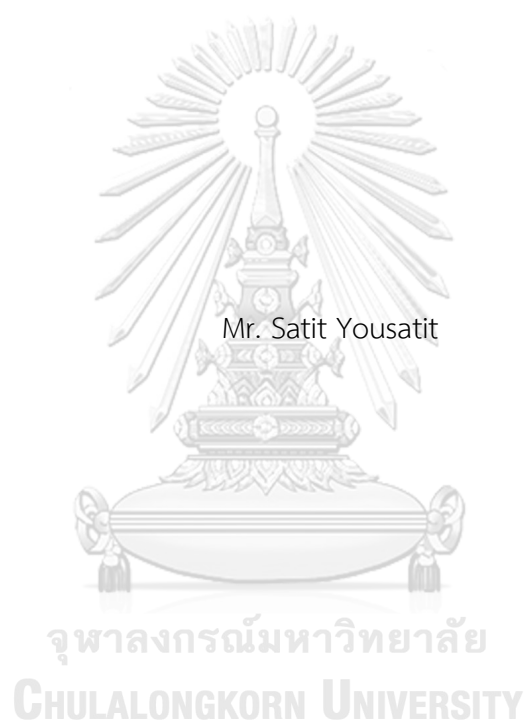


MESOPOROUS CARBON/SILICA NANOCOMPOSITES WITH ACID AND BASE PROPERTIES  
FOR GLUCOSE CONVERSION INTO VALUE ADDED CHEMICALS



A Dissertation Submitted in Partial Fulfillment of the Requirements  
for the Degree of Doctor of Philosophy in Chemical Technology

Department of Chemical Technology

FACULTY OF SCIENCE

Chulalongkorn University

Academic Year 2021

Copyright of Chulalongkorn University

มีโซพอร์สคาร์บอน/ซิลิกานาโนคอมพอสิตที่มีสมบัติกรดและเบสสำหรับการเปลี่ยนกลุ่มโคสเป็นสารเคมี  
มูลค่าเพิ่ม



วิทยานิพนธ์นี้เป็นส่วนหนึ่งของการศึกษาตามหลักสูตรปริญญาวิทยาศาสตรดุษฎีบัณฑิต  
สาขาวิชาเคมีเทคนิค ภาควิชาเคมีเทคนิค  
คณะวิทยาศาสตร์ จุฬาลงกรณ์มหาวิทยาลัย  
ปีการศึกษา 2564  
ลิขสิทธิ์ของจุฬาลงกรณ์มหาวิทยาลัย

Thesis Title	MESOPOROUS CARBON/SILICA NANOCOMPOSITES WITH ACID AND BASE PROPERTIES FOR GLUCOSE CONVERSION INTO VALUE ADDED CHEMICALS
By	Mr. Satit Yousatit
Field of Study	Chemical Technology
Thesis Advisor	Professor Chawalit Ngamcharussrivichai, Ph.D.
Thesis Co Advisor	Associate Professor Toshiyuki Yokoi, Ph.D.

---

Accepted by the FACULTY OF SCIENCE, Chulalongkorn University in Partial Fulfillment of the Requirement for the Doctor of Philosophy

----- Dean of the FACULTY OF SCIENCE  
(Professor POLKIT SANGVANICH, Ph.D.)

DISSERTATION COMMITTEE

----- Chairman  
(Associate Professor PRASERT REUBROYCHAROEN, Ph.D.)

----- Thesis Advisor  
(Professor Chawalit Ngamcharussrivichai, Ph.D.)

----- Thesis Co-Advisor  
(Associate Professor Toshiyuki Yokoi, Ph.D.)

----- Examiner  
(Professor PATTARAPAN PRASASSARAKICH, Ph.D.)

----- Examiner  
(Professor APANEE LUENGNARUEMITCHAI, Ph.D.)

----- External Examiner  
(Professor Attasak Jaree, Ph.D.)

สาริต อยู่สถิตย์ : มีโซพอร์สคาร์บอน/ซิลิกานาโนคอมพอสิตที่มีสมบัติกรดและเบส  
 สำหรับการเปลี่ยนกลูโคสเป็นสารเคมีมูลค่าเพิ่ม. ( MESOPOROUS CARBON/SILICA  
 NANOCOMPOSITES WITH ACID AND BASE PROPERTIES FOR GLUCOSE  
 CONVERSION INTO VALUE ADDED CHEMICALS) อ.ที่ปรึกษาหลัก : ศ. ดร.ชวลิต  
 งามจรัสศรีวิชัย, อ.ที่ปรึกษาร่วม : รศ. ดร.โทชิยุกิ โยโคอิ

งานวิจัยนี้มีจุดประสงค์เพื่อศึกษาการเตรียมมีโซพอร์สคาร์บอน/ซิลิกานาโนคอมพอสิต (MCS) โดยใช้อย่างธรรมชาติเป็นแหล่งคาร์บอนหมุนเวียน คอมพอสิตของยางธรรมชาติและซิลิกา (NR/HMS) ถูกเตรียมด้วยวิธีอินซิทู โซล-เจล เพื่อใช้เป็นสารตั้งต้นแล้วเปลี่ยนเป็น MCS ด้วยวิธีคาร์บอนไนเซชัน มีโซพอร์สคาร์บอน/ซิลิกานาโนคอมพอสิตที่หมู่กรดซัลโฟนิก (MCS-SO<sub>3</sub>H) ถูกเตรียมผ่านกระบวนการซัลโฟเนชันด้วยสารละลายกรดซัลฟิวริก จากนั้นพื้นผิวซิลิกาของ MCS-SO<sub>3</sub>H ถูกต่อติดเชิงเคมีด้วย 3-อะมิโนโพรพิลไตรเมทอกซีไซเลนเพื่อสังเคราะห์ตัวเร่งปฏิกิริยาที่มีหมู่กรดและเบส (MCS-SO<sub>3</sub>H-NH<sub>2</sub>) และใช้เป็นตัวเร่งปฏิกิริยาในการเปลี่ยนกลูโคส จากการวิเคราะห์พบว่ามีโซพอร์สคาร์บอน/ซิลิกานาโนคอมพอสิตแสดงการจัดเรียงตัวของโครงสร้าง สมบัติความพรุน รวมถึงแสดงสมบัติความไม่ชอบน้ำเพิ่มขึ้นเมื่อเพิ่มอุณหภูมิการเผาไปถึง 700 องศาเซลเซียส ส่วนการใช้กรดซัลฟิวริกความเข้มข้นกรดสูงจะส่งเสริมให้ยางธรรมชาติเปลี่ยนไปเป็นคาร์บอนได้มากขึ้น ส่งผลให้มีปริมาณคาร์บอนเพิ่มขึ้น สำหรับการเปลี่ยนฟรุคโตสไปเป็น 5-ไฮดรอกซีเมทิลเฟอรัล (HMF) จะเพิ่มขึ้น เมื่อเพิ่มปริมาณกรดของ MCS-SO<sub>3</sub>H เพิ่มขึ้น ตัวเร่งปฏิกิริยา MCS-SO<sub>3</sub>H-NH<sub>2</sub> มีประสิทธิภาพสำหรับใช้ในการสังเคราะห์ HMF จากกลูโคส อีกทั้งยังสามารถยับยั้งการเกิดกรดแลคติกที่เป็นผลิตภัณฑ์ได้จากไฮโดรไลซิสของ HMF นอกจากนี้ตัวเร่งปฏิกิริยา MCS-SO<sub>3</sub>H-NH<sub>2</sub> ยังมีความสามารถในการกลับมาใช้ซ้ำสำหรับการเร่งปฏิกิริยาดีไฮเดรชันของกลูโคสอย่างน้อย 3 รอบ

สาขาวิชา เคมีเทคนิค  
 ปีการศึกษา 2564

ลายมือชื่อนิสิต .....  
 ลายมือชื่อ อ.ที่ปรึกษาหลัก .....  
 ลายมือชื่อ อ.ที่ปรึกษาร่วม .....

# # 6072859323 : MAJOR CHEMICAL TECHNOLOGY

KEYWORD: Mesoporous silica, Carbon/silica, Nanocomposite, Hydrophobicity,  
Glucose conversion

Satit Yousatit : MESOPOROUS CARBON/SILICA NANOCOMPOSITES WITH  
ACID AND BASE PROPERTIES FOR GLUCOSE CONVERSION INTO VALUE  
ADDED CHEMICALS. Advisor: Prof. Chawalit Ngamcharussrivichai, Ph.D. Co-  
advisor: Assoc. Prof. Toshiyuki Yokoi, Ph.D.

The purpose of this study is to prepare mesoporous carbon/silica (MCS) nanocomposites using natural rubber (NR) as a renewable carbon source. A series of mesoporous nanocomposites based on NR and hexagonal mesoporous silica (HMS), prepared via an *in situ* sol-gel process, were used as precursors, which were then converted into the MCS materials by carbonization. The sulfonic acid-functionalized mesoporous carbon/silica (MCS-SO<sub>3</sub>H) was prepared by direct sulfonation with H<sub>2</sub>SO<sub>4</sub> solution. The silica surface of MCS-SO<sub>3</sub>H were then grafted by 3-aminopropyltrimethoxysilane to produce the acid-base catalysts (MCS-SO<sub>3</sub>H-NH<sub>2</sub>) and used as the solid catalysts in glucose conversion. The MCS nanocomposites exhibited enhanced structural, textural, and hydrophobic properties after increasing the carbonization temperature up to 700 °C, while using a high concentration of H<sub>2</sub>SO<sub>4</sub> solution promoted rubber conversion into carbon residues, resulting in an increased carbon content. Conversion of fructose to 5-hydroxymethylfurfural (HMF) increases with an increase in the acidity of the MCS-SO<sub>3</sub>H catalysts. MCS-SO<sub>3</sub>H-NH<sub>2</sub> has prospect for the HMF synthesis from glucose. In addition, the formation of levulinic acid, as a byproduct from HMF hydrolysis, was retarded over the MCS-base nanocomposite catalysts. Moreover, the MCS-SO<sub>3</sub>H-NH<sub>2</sub> catalysts exhibited reusability in the glucose dehydration for at least 3 cycles.

Field of Study: Chemical Technology

Student's Signature .....

Academic Year: 2021

Advisor's Signature .....

Co-advisor's Signature .....

## ACKNOWLEDGEMENTS

I would like to express my profound gratitude to my supervisor, Prof. Chawalit Ngamcharussrivichai for his scientific guidance, insightful comments, and considerable encouragement to complete this thesis. I deeply appreciate his careful revision of all my work. I also would like to thank his friendship.

I express my gratitude to my co-advisor, Assoc. Prof. Toshiyuki Yokoi who offered many helpful suggestions and supported my study for 9 months at the Nanospace Catalysis Unit, Institute of Innovative Research, Tokyo Institute of Technology, Japan. I also thank all Nanospace Catalysis Unit members for their helpful advice, supports, encouragement, and friendship during my period in Japan.

I also would like to thank Asst. Prof. Sakdinun Nuntang and my research group (Fai, Ploy, Ice, etc.) for suggestions and kindly support my thesis.

Sincerest appreciation also extends to The Royal Golden Jubilee Scholarship from the Thailand Science Research and Innovation (TSRI) for the financial support essential to complete this project.

I would like to acknowledge Assoc. Prof. Dr. Prasert Reubroycharoen, Prof. Pattarapan Prasassarakich, Prof. Apanee Luengnaruemitchai, and Prof. Attasak Jaree for their participation as the dissertation chairman and members of the thesis committee, respectively.

Lastly, I wish to express my love and my gratitude to my lover and my family for their constant support, and encouragement during the completion of the thesis.

Satit Yousatit

## TABLE OF CONTENTS

	Page
.....	iii
ABSTRACT (THAI) .....	iii
.....	iv
ABSTRACT (ENGLISH) .....	iv
ACKNOWLEDGEMENTS .....	v
TABLE OF CONTENTS .....	vi
List of tables.....	xii
List of figures.....	xiv
ABBREVIATIONS.....	xx
NOMENCLATURE.....	xxi
Chapter 1 INTRODUCTION .....	1
1.1 Motivation.....	1
1.1 Objectives.....	4
1.3 Scope of this work.....	5
<i>Chapter 2</i> THEORY AND LITERATURE REVIEWS.....	1
2.1 Porous materials .....	1
2.2 Mesoporous silica materials .....	3
2.3 Hexagonal mesoporous silica .....	5
2.3.1 General features .....	5
2.3.2 Synthesis of hexagonal mesoporous silica .....	6
2.3.3 Applications of hexagonal mesoporous silica.....	7

2.4 Mesoporous natural rubber/silica nanocomposites.....	9
2.4.1 General features .....	9
2.4.2 Synthesis of NR/HMS nanocomposites .....	9
2.4.3 Application of NR/HMS nanocomposites .....	10
2.5 Mesoporous carbon/silica nanocomposites.....	11
2.5.1 General features .....	11
2.5.2 Synthesis of mesoporous carbon/silica nanocomposites .....	12
2.5.3 Functionalization of carbon/silica nanocomposites.....	14
2.5.4 Application of mesoporous carbon/silica nanocomposites in catalytic biomass conversion .....	16
2.6 Biomass.....	17
2.6.1 Lignocellulosic biomass.....	18
2.6.2 Conversion of lignocellulosic biomass into platform chemicals.....	21
2.7 Hexose.....	22
2.7.1 Glucose .....	22
2.7.2 Fructose .....	23
2.7.3 Transformation of hexose into value-added chemicals .....	24
2.7.4 5-hydroxymethylfurfural (HMF).....	24
2.8 Synthesis of HMF using Brønsted acid-base catalyst .....	26
2.8.1 Conversion of glucose into HMF .....	26
2.8.2 Homogeneous acid-base catalysts.....	27
2.8.3 Heterogeneous acid-base catalysts .....	27
2.8.4 Solvent systems.....	27
2.8.4.1 Monophasic solvent systems .....	27



2.8.4.2	Biphasic solvent systems.....	28
2.9	Literature reviews .....	29
2.9.1	Synthesis of polymer/silica and carbon/silica nanocomposites.....	29
2.9.2	Functionalized mesoporous carbon/silica with sulfonic group .....	30
2.9.3	Catalysts in glucose conversion into HMF .....	31
Chapter 3	EXPERIMENTAL AND ANALYTICAL METHOD .....	33
3.1	Materials .....	33
3.1.1	Chemical for synthesis mesoporous materials and composites .....	33
3.1.2	Chemical for HMF synthesis.....	33
3.1.3	Chemicals for reaction product analysis .....	34
3.2	Instruments and equipment.....	34
3.3	Preparation of pure silica HMS, NR/HMS and MCS nanocomposites .....	35
3.3.1	Synthesis of hexagonal mesoporous silica (HMS).....	35
3.3.2	Natural rubber and hexagonal mesoporous silica nanocomposites (NR/HMS) synthesis .....	37
3.3.3	Mesoporous carbon/silica nanocomposites (MCS) synthesis .....	39
3.4	Functionalization of pure silica HMS and MCS nanocomposites .....	41
3.4.1	Sulfonation of MCS nanocomposites (MCS-SO <sub>3</sub> H).....	41
3.4.2	Functionalization of MCS and MCS-SO <sub>3</sub> H with aminopropyl groups .....	42
3.4.3	Functionalization of HMS with organo-sulfonic acid and aminopropyl groups.....	43
3.5	Characterization of Materials.....	45
3.5.1	Structural analysis.....	45
	X-ray Powder diffraction (XRD).....	45

Raman spectroscopy .....	46
3.5.2 Compositional and elemental analysis.....	47
Thermogravimetric/differential thermal analysis (TG/DTA).....	47
Carbon, Hydrogen, Nitrogen and Sulfur (CHNS) analysis .....	47
3.5.3 Textural properties and hydrophobicity measurement.....	47
N <sub>2</sub> adsorption-desorption measurement.....	47
H <sub>2</sub> O adsorption-desorption measurement.....	49
3.5.4 Surface functional groups analysis.....	49
Fourier-transform infrared spectroscopy (FTIR).....	49
Solid-state <sup>29</sup> Si magic angle spinning nuclear magnetic resonance ( <sup>29</sup> Si MAS NMR) and <sup>13</sup> C cross-polarization magic angle spinning nuclear magnetic resonance ( <sup>13</sup> C CP/MAS NMR).....	50
3.5.5 Morphology and microstructural analysis .....	51
Field-emission scanning electron microscopy (FE-SEM) .....	51
Transmission electron microscopy (TEM).....	51
3.4.6 Acidity and basicity measurement .....	51
3.6 Catalytic performance of MCS catalysts.....	52
3.6.1 Study on the effect of functionalized HMS and MCS as catalyst.....	52
3.6.2 Study on the effect of reaction temperature and time.....	52
3.6.3 Study on the effect of catalyst amount .....	53
3.6 Catalyst reusability of MCS-SO <sub>3</sub> H-NH <sub>2</sub> composite .....	53
3.7 Reaction product analysis .....	53
Chapter 4 SYNTHESIS AND CHARACTERIZATION OF MCS COMPOSITES.....	55
4.1 Thermogravimetric/differential thermal analysis (TG/DTA).....	55

4.2 XRD analysis.....	60
4.3 N <sub>2</sub> physisorption measurement .....	64
4.4 FTIR spectroscopy .....	67
4.5 Raman spectroscopy .....	68
4.6 XPS analysis .....	71
4.7 Solid state <sup>29</sup> Si MAS NMR and <sup>13</sup> C CP/MAS NMR studies .....	76
4.8 Field-emission scanning electron microscopy (FE-SEM) .....	78
4.9 Transmission electron microscopy (TEM).....	80
4.10 H <sub>2</sub> O adsorption measurement.....	81
4.11 SAXS analysis.....	83
4.12 Formation of mesoporous NR/HMS and MCS nanocomposites.....	84
Chapter 5 Functionalization and Characterization of MCS nanocomposites .....	86
5.1 Compositional and elemental analysis .....	86
5.2 XRD analysis.....	89
5.3 N <sub>2</sub> physisorption measurement .....	90
5.4 FTIR spectroscopy .....	93
5.5 XPS analysis .....	94
5.6 Solid state <sup>29</sup> Si MAS NMR and <sup>13</sup> C CP/MAS NMR studies .....	96
5.7 Raman spectroscopy .....	98
5.8 Acidity and basicity measurement.....	101
5.9 H <sub>2</sub> O adsorption measurement .....	103
Chapter 6 Catalytic activity of synthesized composites in HMF synthesis .....	105
6.1 Dehydration of fructose into HMF.....	105
6.2 Conversion of glucose into HMF .....	107

6.2.1 Effect of Catalyst Functionality on Glucose Conversion into HMF .....	107
6.2.2 Effect of reaction temperature and time .....	110
6.2.3 Effect of catalyst amount .....	111
6.3 Reusability of MCS-SO <sub>3</sub> H-NH <sub>2</sub> composite .....	112
6.4 Comparison of catalyst performance .....	114
Chapter 7 CONCLUSIONS AND RECOMMANDATIONS .....	116
7.1 Conclusions .....	116
7.2 Recommendation and future works .....	117
REFERENCES .....	119
APPENDIX A Quantitative chemical calculation for preparation MCS composites .....	133
APPENDIX B HPLC Chromatogram and Standard Curve of Reactants and Products..	134
APPENDIX C Calculation of conversion .....	139
VITA .....	142

## List of tables

	Page
Table 2.1 Examples of porous materials applied in catalysis and adsorption applications. ....	2
Table 2.2 Structural and textural properties of some mesoporous silicas. ....	3
Table 2.3 Summary of advantage and disadvantage of two organic functionalized modification methods.....	8
Table 2.4 HMF derivatives and its industrial applications.....	25
Table 3.1 Synthesis conditions of MCS material.....	39
Table 3.2 Synthesis conditions of MCS-SO <sub>3</sub> H material.....	41
Table 3.3 Synthesis conditions of MCS-SO <sub>3</sub> H-NH <sub>2</sub> and MCS-NH <sub>2</sub> material.....	42
Table 4.1 Carbon content of the pure silica HMS, NR/HMS precursor and MCS nanocomposites prepared under different conditions. ....	57
Table 4.2 Structural properties of the pure silica HMS, NR/HMS precursor and MCS nanocomposites prepared under different conditions. ....	61
Table 4.3 Textural properties of the pure silica HMS, NR/HMS precursor and MCS nanocomposites prepared under different conditions. ....	66
Table 4.4 Raman spectroscopy results of the pure silica HMS, NR/HMS precursor, and MCS nanocomposites. ....	70
Table 4.5 XPS results of the pure silica HMS, NR/HMS precursor, and MCS nanocomposites.....	75
Table 4.6 Relative intensity of the Q <sup>n</sup> group .....	78
Table 4.7 Water adsorption volume of the pure silica HMS, NR/HMS precursor and MCS nanocomposites prepared under different conditions .....	82
Table 5.1 Chemical composition of HMS and MCS-based catalysts.....	88

Table 5.2 Textural properties of HMS and MCS-based catalysts.....	91
Table 5.3 Relative intensities of the T <sup>m</sup> and Q <sup>n</sup> groups .....	97
Table 5.4 Raman spectroscopy results of the functionalized MCS Nanocomposites. .	99
Table 5.5 Chemical composition, acidity and basicity of HMS and MCS-based catalysts.....	102
Table 5.6 Water adsorption volume of HMS and MCS-based catalysts.....	104
Table 6.1 Transformation of fructose to HMF over HMS and MCS-based catalysts. .	106
Table 6.2 Chemical composition of MCS-based catalysts fresh MCS-18S-0.2N and spent MCS-18S-0.2N after used at 3st cycle in glucose dehydration.....	113
Table 6.3 Overview of HMF yields from the conversion of fructose and glucose in the representative catalytic system.....	115
Table A.1 Molecular weight and density of concentrated sulfuric acid solution.....	133
Table C.1 Peak area of sugar substrates and products in aqueous phase.....	139
Table C.2 Peak area of products in organic phase .....	141

## List of figures

	Page
Figure 1.1 Catalytic transformation of HMF into its derivatives [2].....	1
Figure 1.2 The reaction pathway for the conversion of glucose into HMF [4]. .....	2
Figure 1.3 Experimental framework of this study. ....	7
Figure 2.1 Classification of porous materials based on their framework building blocks [10].....	1
Figure 2.2 Schematic representation of mechanistic pathways for the synthesis of MCM-41 [15]. .....	4
Figure 2.3 TEM image of HMS [25]. .....	5
Figure 2.4 Schematic representation of HMS mesoporous silica synthesis by neutral template ( $S^{0I^0}$ ) mechanism [16]. .....	6
Figure 2.5 Functionalization of surface of mesoporous silica by (a) post-grafting and (b) direct co-condensation methods using trialkoxyorganosilane [27]. .....	8
Figure 2.6 Schematic representation of the formation of the hexagonal array of silicate micellar rods and NR [9]. .....	9
Figure 2.7 The mechanistic model for the formation of NR/HMS nanocomposite prepared with the pre-swelling step [28]. .....	10
Figure 2.8 Schematic representation of the formation of the hexagonal array of silicate micellar rods and NR in the presence of propylsulfonic acid groups [20]. .....	11
Figure 2.9 Structural scheme of mesoporous carbon/silica nanocomposites. Red represents silica framework and black represents carbon phase [31]. .....	12
Figure 2.10 Sequence of events during chemical vapour deposition (CVD). .....	13
Figure 2.11 Triconstituent co-assembly to ordered mesoporous carbon-silica nanocomposites [36]. .....	14

Figure 2.12 Summary of possible ways that permit functionalization of the surface of carbon/silica nanocomposites with $-SO_3H$ groups [32].	15
Figure 2.13 Schematic representation of carbon structure and surface function group on carbon surface of sulfonated carbon/silica composites [42].	17
Figure 2.14 The major biomass sources [44].	18
Figure 2.15 The main components and structure of lignocellulose [46].	19
Figure 2.16 The structural formula of cellulose [48].	19
Figure 2.17 The structural formula of hemicellulose [51].	20
Figure 2.18 The structural formula of lignin and its derivatives [43].	21
Figure 2.19 Conversion routes for the platform chemicals produced from lignocellulosic biomass. [43].	22
Figure 2.20 The structures of (A) D-glucose and (B) D-fructose in a Fischer formular [56].	22
Figure 2.21 Hydrolysis of cellulose in lignocellulose [58].	23
Figure 2.22 Lobry de Bruyn–Alberda van Ekenstein (LdB–AvE) Mechanism for the Base-Catalyzed Isomerization of Glucose to Fructose [60].	23
Figure 2.23 Selective transformation of hexose into various chemicals [61].	24
Figure 2.24 The structural formula of HMF.	25
Figure 2.25 A typical reaction scheme for glucose transformation [6].	26
Figure 2.26 Schematic diagram of a biphasic system for HMF production.	29
Figure 3.1 Schematic diagram of HMS synthesis.	36
Figure 3.2 Temperature program of muffle furnace condition for HMS calcination.	36
Figure 3.3 Schematic diagram of NR/HMS synthesis.	38
Figure 3.4 Schematic diagram of MCS synthesis.	40
Figure 3.5 Temperature program of tubular furnace condition for carbonization.	40



Figure 3.6 Schematic diagram of MCS-SO <sub>3</sub> H synthesis.....	41
Figure 3.7 Schematic diagram of MCS-SO <sub>3</sub> H-NH <sub>2</sub> synthesis. ....	42
Figure 3.8 Chemical structure of MPS and APS. ....	43
Figure 3.9 Schematic diagram of HMS-SO <sub>3</sub> H-NH <sub>2</sub> synthesis. ....	44
Figure 3.10 Diffraction of X-ray by regular planes of atoms.....	45
Figure 3.11 The IUPAC classification of adsorption isotherm.....	48
Figure 4.1 Weight loss and DTA curves of HMS, NR/HMS, and MCS-0.5G-0.05M- <i>t</i> series prepared at different carbonization temperatures.....	56
Figure 4.2 Weight loss and DTA curves of MCS-0.5G- <i>y</i> M-700 series prepared at H <sub>2</sub> SO <sub>4</sub> concentration.....	58
Figure 4.3 Weight loss and DTA curves of MCS-xG-1.00M-700 series prepared at different natural rubber content in the preparation of the NR/HMS precursor.....	59
Figure 4.4 XRD patterns of HMS, NR/HMS, and MCS-0.5G-0.05M- <i>t</i> series prepared at different carbonization temperatures.....	60
Figure 4.5 XRD patterns of MCS-0.5G- <i>y</i> M-700 series prepared at H <sub>2</sub> SO <sub>4</sub> concentration. ....	62
Figure 4.6 XRD patterns of MCS-xG-1.00M-700 series prepared at different natural rubber content in the preparation of the NR/HMS precursor. ....	63
Figure 4.7 N <sub>2</sub> adsorption-desorption isotherms of pure silica HMS, NR/HMS precursor, and MCS nanocomposites prepared under different conditions.....	65
Figure 4.8 FTIR spectra of pure silica HMS, NR/HMS precursor, and MCS nanocomposites prepared under different conditions. ....	67
Figure 4.9 Raman spectra of pure silica HMS, NR/HMS precursor, and MCS nanocomposites prepared under different conditions at low Raman shift region. ....	69
Figure 4.10 Raman spectra of NR/HMS precursor, and MCS nanocomposites prepared under different conditions at high Raman shift region.....	69

Figure 4.11 C1s XPS spectra of (A) NR/HMS, (B) MCS-0.5G-1.00M-700, (C) MCS-0.5G-2.00M-700, and (D) MCS-1.5G-1.00M-700. ....	72
Figure 4.12 O1s XPS spectra of (A) NR/HMS, (B) MCS-0.5G-1.00M-700, (C) MCS-0.5G-2.00M-700, and (D) MCS-1.5G-1.00M-700. ....	73
Figure 4.13 Solid-state $^{13}\text{C}$ CP/MAS NMR spectra of HMS, NR/HMS, and MCS-0.5G-1.00M-700. ....	76
Figure 4.14 Solid-state $^{29}\text{Si}$ -MAS NMR spectra of HMS, NR/HMS, and MCS-0.5G-1.00M-700. ....	77
Figure 4.15 FE-SEM images of (A) HMS, (B) NR/HMS, (C) MCS-0.5G-1.00M-700, and (D) MCS-0.5G-2.00M-700, all at a magnification of 150000 $\times$ .....	79
Figure 4.16 TEM images of the (A) HMS, (B) NR/HMS, (C) MCS-0.5G-1.00M-700, and (D) MCS-0.5G-2.00M-700, all at a magnification of 100000 $\times$ .....	80
Figure 4.17 Representative water adsorption isotherms of the (a) HMS, (b) NR/HMS, (c) MCS-0.5G-1.00M-700, (d) MCS-0.5G-2.00M-700, and (e) MCS-1.5G-1.00M-700 at the low relative pressures $P/P_0$ in the range of 0–0.6.....	81
Figure 4.18 SAXS patterns of the preparation of the as-synthesized (A) HMS and (B) NR/HMS with different compositions.....	83
Figure 4.19 Mechanistic model for the formation of NR/HMS nanocomposites and their transformation to MCS materials. ....	85
Figure 5.1 Weight loss and DTA curves of (a) MCS, (b) MCS-18S, (c) MCS-0.2N and (d) MCS-18S-0.2N.....	87
Figure 5.2 XRD patterns of HMS and MCS with and without functionalization.....	89
Figure 5.3 $\text{N}_2$ adsorption–desorption isotherms of HMS and MCS with and without functionalization.....	92
Figure 5.4 FTIR spectra of the pure silica HMS, Parent MCS, MCS-18S, MCS-18S-0.2N and MCS-0.2N.....	93

Figure 5.5 (A) C1s, (B) N1s and (C) S2p XPS spectra of parent MCS, MCS-18S, MCS-18S-0.2N and MCS-0.2N.....	95
Figure 5.6 Solid-state $^{13}\text{C}$ CP/MAS NMR spectra of parent MCS, MCS-18S, MCS-18S-0.2N and MCS-0.2N.....	96
Figure 5.7 Solid-state $^{29}\text{Si}$ MAS NMR spectra of parent MCS, MCS-18S, MCS-18S-0.2N and MCS-0.2N.....	97
Figure 5.8 Raman spectra of parent MCS, MCS-18S, MCS-18S-0.2N and MCS-0.2N.....	98
Figure 5.9 Schematic diagram showing the preparation process of acid and base functionalized MCS composites.....	100
Figure 6.1 Glucose conversion over functionalized HMS and MCS composites. Reaction conditions: 100 mg catalyst, 5 ml of 200 mM glucose in NaCl solution, 10 ml THF, 150 °C, 2 h.....	107
Figure 6.2 Relationship of (A) number of basic sites and (B) number of acid sites over functionalized HMS and MCS composites.....	108
Figure 6.3 Relationship of the fructose, HMF, and humins yield and number of basic sites and acid sites from glucose conversion over functionalized HMS and MCS composites.....	109
Figure 6.4 Effect of temperature and reaction time on glucose conversion to HMF catalyzed by MCS-18S-0.2N. Reaction conditions: 5 mL 0.2-M glucose in NaCl solution, 10 mL THF, 100 mg MCS-18S-0.2N.....	110
Figure 6.5 Effect of catalyst amount on glucose conversion to HMF catalyzed by MCS-18S-0.2N. Reaction conditions: 5 mL 0.2-M glucose in NaCl solution, 10 mL THF, 190 °C, 1 h.....	112
Figure 6.6 Reusability of MCS-18S-0.2N in catalytic glucose conversion to HMF. Reaction conditions: 5 mL 0.2-M glucose in NaCl solution, 10 mL THF, 50 mg catalyst, 190 °C, 1 h.....	113

Figure B.1 Chromatogram of Glucose, Fructose, Luvulinic acid, HMF, and furfural in aqueous phase by using 2-butanone as internal standard.....	134
Figure B.2 Chromatogram of HMF and furfural in organic phase by using 5-methyl-2-furaldehyde as internal standard.....	134
Figure B.3 The standard curves of glucose by using 2-butanone as internal standard. .....	135
Figure B.4 The standard curves of fructose by using 2-butanone as internal standard. .....	135
Figure B.5 The standard curves of HMF by using 2-butanone as internal standard. .	136
Figure B.6 The standard curves of luvulinic acid by using 2-butanone as internal standard. ....	136
Figure B.7 The standard curves of furfural by using 2-butanone as internal standard. .....	137
Figure B.8 The standard curves of HMF by using 5-methyl-2-furaldehyde as internal standard. ....	137
Figure B.9 The standard curves of furfural by using 5-methyl-2-furaldehyde as internal standard. ....	138

## ABBREVIATIONS

BET	=	Brunner-Eller-Teller
BJH	=	Barret-Joyner-Halenda
DDA	=	Dodecylamine
DTA	=	Differential Thermal Analysis
FTIR	=	Fourier Transform Infrared Spectroscopy
HMS	=	Hexagonal Mesoporous Silica
MPTMS	=	3-mercaptopropyltrimethoxysilane
MAS	=	Magic Angle Spinning
NMR	=	Nuclear Magnetic Resonance
NR	=	Natural Rubber
SEM	=	Scanning Electron Microscope
TEM	=	Transmission Electron Microscopy
TEOS	=	Tetraethylorthosilicate or tetraethoxysilane
TGA	=	Thermo Gravimetric Analysis
THF	=	Tetrahydrofuran
XRD	=	X-Ray Diffraction
HPLC	=	High-performance liquid chromatography

## NOMENCLATURE

$^{\circ}\text{C}$	=	Degree Celsius
g	=	Gram
mL	=	Milliliter
min	=	Minute
h	=	Hour
$\text{cm}^{-1}$	=	Unit of wavenumber
$a_0$	=	The repeat distance between pore centers of the hexagonal structure
$d_{100}$	=	d-spacing of plane (100)
$S_{\text{BET}}$	=	BET specific surface area ( $\text{m}^2 \text{g}^{-1}$ )
$S_{\text{ext}}$	=	External surface area ( $\text{m}^2 \text{g}^{-1}$ )
$D_p$	=	Pore diameter (nm)
$V_t$	=	Total pore volume ( $\text{cm}^3 \text{g}^{-1}$ )
$V_p$	=	Mesopore volume ( $\text{cm}^3 \text{g}^{-1}$ )
$V_m$	=	Monolayer adsorbed volume ( $\text{cm}^3 \text{g}^{-1}$ )

# Chapter 1

## INTRODUCTION

### 1.1 Motivation

Plant-based biomass is a renewable feedstock abundantly available in Thailand, which is present as energy crops, agricultural wastes, and forestry-derived materials and products. These sources mainly consist of cellulose, hemicellulose, and lignin. The cellulose and hemicellulose consist primarily of C5 and C6 sugars. Under controlled conditions, cellulose can be hydrolyzed into glucose, which then can be dehydrated to produce 5-hydroxymethylfurfural (HMF). The US Department of Energy listed HMF as one of the top ten value-added bio-based chemicals [1]. It can serve as a versatile precursor for the synthesis of a variety of value-added chemicals and high-quality liquid fuels as show in Figure 1.1. For example, 2,5-furandicarboxylic acid (FDCA) is synthesized via selective oxidation of HMF, which is main building block as a sustainable alternative to petrochemical derived terephthalic acid for production of green polymer such as polyethylene 2,5-furandicarboxylate (PEF). Moreover, the hydrogenation product (2,5-dimethylfuran, DMF) and etherification product (5-ethoxymethylfurfural, EMF) of HMF are excellent miscible diesel biofuels, with high energy densities [2].

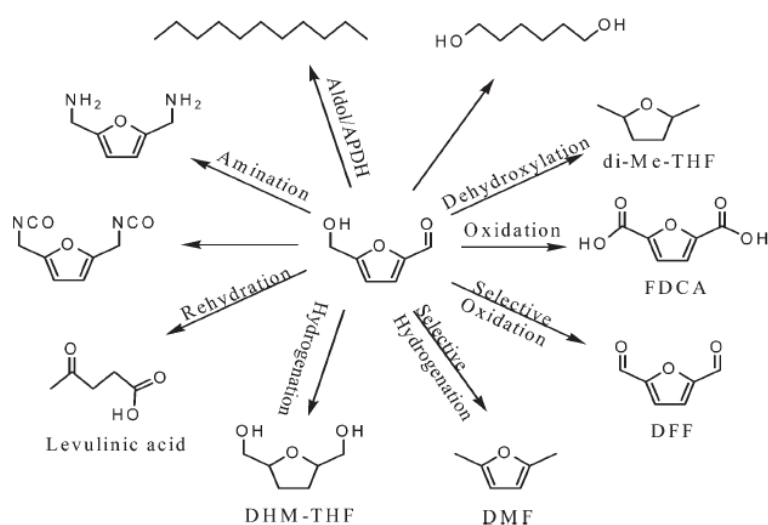


**Figure 1.1** Catalytic transformation of HMF into its derivatives [2].

The acid-catalyzed dehydration of fructose produces HMF at a high yield [3]. However, the use of fructose as substrates in the synthesis of HMF is not an economical option due to its relatively high cost when compared to glucose, as the most abundant monosaccharide consisting of cellulose. Therefore, the synthesis of HMF from glucose is much more economical as compared with that from fructose-based carbohydrates. However, the direct dehydration of glucose into HMF catalyzed by conventional Brønsted acids generally results in lower HMF yields. The successful dehydration of glucose into HMF requires two consecutive steps, including the isomerization of glucose into fructose and the subsequent dehydration of fructose into HMF. The glucose isomerization can be catalyzed by Brønsted bases, Lewis acids and enzymes, while the fructose dehydration into HMF, a very facile reaction, can be catalyzed by both Brønsted and Lewis acids [3]. Moreover, side reactions are always occurred, such as the further hydrolysis of HMF into levulinic acid and the polymerization of HMF itself or with fructose to humins or oligomers as show in Figure 1.2.

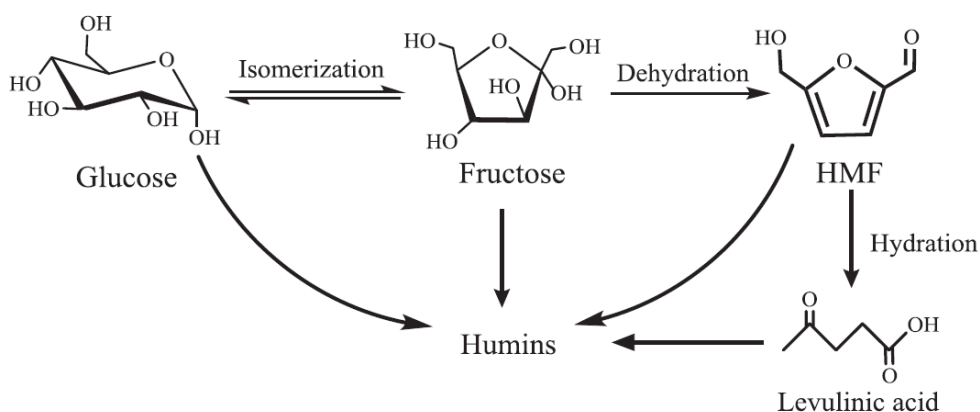


**Figure 1.2** The reaction pathway for the conversion of glucose into HMF [4].

Currently, the synthesis of HMF via the isomerization and dehydration of glucose is achieved in the presence of mineral acids or combined homogeneous base and acid Brønsted systems, such as  $\text{H}_2\text{SO}_4$ ,  $\text{H}_3\text{PO}_4$ ,  $\text{HCl}$ ,  $\text{H}_3\text{PO}_4/(\text{NH}_4)_2\text{HPO}_4$ , and  $\text{H}_3\text{PO}_4/\text{pyridine}$  [5]. These catalysts actively promote a high conversion of glucose, giving a high yield of HMF since they possess high acidity and present in the same



phase as the reaction mixture. However, at the end of production process, a neutralization step is necessary to stop the catalytic reaction, and then a purification of the products can be attempted. Typically, using these homogeneous acid catalysts is associated with high toxicity, material corrosion, a large amount of liquid waste and product contamination. In addition, it is difficult to recycle the homogeneous acids.

Recently, the application of heterogeneous catalysts has attracted considerable attention in the synthesis of HMF since they exhibit not only high activities under moderate conditions but also offer several advantages, such as reusability and waste minimization. A huge number of researches have been attempted to develop new solid acid and base catalysts to enhance the yield of desired chemical products. For solid base catalysts catalyzed isomerization of glucose into fructose, Mg–Al hydrotalcite (HT) is a layered double hydroxide with the general formula of  $Mg_6Al_2CO_3(OH)_{16}\cdot 4(H_2O)$ . The  $HCO_3^-$  groups on the surface were found to display the highest activity for isomerization. However, these catalysts still poor HMF selectivity due to the presence of high strength of basic sites leading to humins formation. Amberlyst 15, an acidic ion-exchange resin, is an active catalyst in the dehydration due to its high density of sulfonic acid group and high hydrophobicity. Nevertheless, its applicability to the practical process is limited by low thermal stability (less than  $<140\text{ }^\circ\text{C}$ ) and high cost [6].

The mesoporous carbon/silica (MCS) nanocomposites would combine the advantages properties of silica (i.e. uniform mesopores and a well-defined pore arrangement) and organic carbon, such as a facility to incorporate oxygen containing functional groups (i.e. sulfonic, carbonyl, hydroxyl, carboxylic, etc.) [7]. These materials are usually prepared by filling the active carbon-containing precursors, such as furfural [8], inside the mesoporous channels of silica-based materials, followed by carbonization under controlled conditions. The obtained nanocomposites are characterized by carbonaceous layer coating on the internal surface of mesoporous silica framework. The sulfonic acid functionalized MCS nanocomposites, post-

modified by sulfonation, are candidates in acid catalytic dehydration. As report in the previous studies, silica itself can be modified with organosilanes via the reaction of surface silanol group, which were then grafted by 3-aminopropyltri-methoxysilane to produce the acid–base catalyst. Recently, novel mesoporous nanocomposites consisting of natural rubber (NR) as a hydrophobicity improver dispersed in the wormhole-like framework of hexagonal mesoporous silica (HMS), namely NR/HMS, have been developed. These nanocomposites have high surface area and porosity. The remaining surface silanol groups allow the composites to be modified with different active functional groups to prepare hydrophobic mesoporous materials serving adsorption and catalysis applications [9]. The purpose of this work is to prepare MCS nanocomposites by using NR/HMS composites as precursors via pyrolysis method and functionalized with sulfonic acid and amino group into carbon phase and surface of silica, respectively. Then these materials have appropriate properties for the conversion of glucose to HMF. It is expected that the carbon and silica matrix functionalized with sulfonic acid and amino group would provide high acidity and basicity and high surface area while the hydrophobic nature of carbon could reduce water adsorption and inhibit the dehydration of HMF into byproduct such as levulinic acid.

## 1.1 Objectives

1.2.1 To find the suitable conditions for preparation of carbon/silica nanocomposites with tunable carbon content, high mesoporosity and well-ordered mesostructure by using natural rubber/hexagonal mesoporous silica materials as precursors

1.2.2 To study the effects of surface functionalization methods and conditions on the preparation of bifunctional acid–base mesoporous carbon/silica nanocomposites

1.2.3 To study the catalytic performance of bifunctional acid–base mesoporous carbon/silica nanocomposites in the glucose conversion into value-added chemicals

### 1.3 Scope of this work

This work was divided into 3 parts. The scope of this study is as follow and the experimental framework is shown in Figure 1.3.

- 1.3.1 Firstly (Part A), Synthesis and characterization of MCS nanocomposites: MCS nanocomposites were prepared via carbonization under an Argon flow by using the NR/HMS composite as the precursors. The effects of carbonization temperature, sulfuric acid concentration for acid pretreatment and initial NR content of the NR/HMS precursor on the physicochemical properties of the MCS nanocomposites obtained were investigated. In addition, the characterization of synthesis composites was analyzed by thermogravimetric/differential thermal analysis (TG/DTA), Nitrogen ( $N_2$ ) adsorption-desorption measurement, powder X-ray diffraction (XRD), Fourier-transform infrared spectroscopy (FTIR), Raman spectroscopy, X-ray photoelectron spectroscopy (XPS), solid-state  $^{29}Si$  magic angle spinning (MAS) nuclear magnetic resonance (NMR) spectroscopy and  $^{13}C$ -cross-polarization (CP) MAS NMR spectroscopy, field-emission scanning electron microscopy (FE-SEM), transmission electron microscopy (TEM) and  $H_2O$  adsorption-desorption measurement.
- 1.3.2 Part B, bifunctional acid-base MCS nanocomposites (MCS- $SO_3H-NH_2$ ): sulfonated MCS nanocomposites (MCS- $SO_3H$ ) were prepared via sulfonation of MCS material using sulfuric acid as sulfonating agent. The surface of MCS- $NH_2$  and MCS- $SO_3H-NH_2$  were modified by post-grafting method using APS as aminosilane coupling agent. The effects sulfuric acid concentration in the sulfonation and APS concentration in post-grafting process on the physicochemical properties of the MCS- $SO_3H$  and MCS- $SO_3H-NH_2$  composites obtained were investigated. The characterization of synthesis composites were analyzed as in section 1.3.1.

1.3.3 Finally (Part C), the catalytic activities of synthesis composites were studied in synthesis of HMF. The MCS-SO<sub>3</sub>H composites were compared their activities with the propylsulfonic acid-functionalized HMS (HMS-SO<sub>3</sub>H) in fructose dehydration into HMF. Moreover, the MCS-SO<sub>3</sub>H-NH<sub>2</sub> were used as bifunctional acid-base catalyst in glucose conversion into HMF. In addition, effects of type of reaction conditions, catalyst loading and initial concentration of substrate on conversion and yield were investigated.



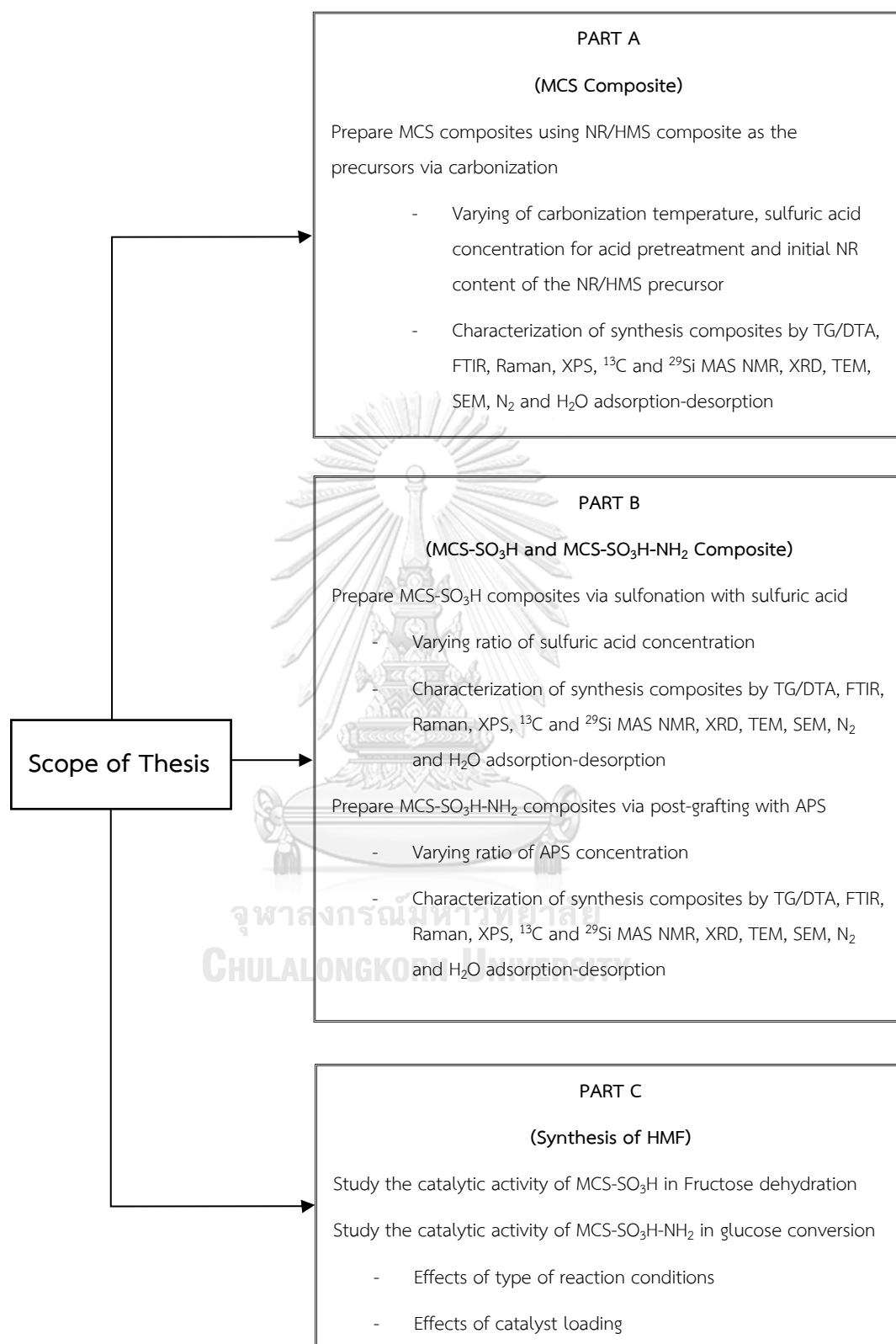


**Figure 1.3** Experimental framework of this study.

## Chapter 2

### THEORY AND LITERATURE REVIEWS

#### 2.1 Porous materials

Porous materials are a class of solids with channels, cavities, or interstices. According to the International Union of Pure and Applied Chemistry (IUPAC) classification, the porous materials can be divided into 3 categories based on their pore size, which are microporous (<2 nm), mesoporous (2–50 nm) and macroporous (>50 nm) materials. The materials with micro-scale pores have received a great deal of interest in the fields of catalysis, adsorption, gas separation and ion exchange, whereas the mesoporous materials have potential applications as catalyst support, enzyme support, protein sorbent and drug carrier. Nevertheless, the characteristics of porous materials depend not only on the size, arrangement, and shape of the pores but also elemental composition and surface functional groups of the materials themselves. Based on the framework composition, the porous materials can be classified to inorganic materials, organic materials, and organic-inorganic hybrids (Figure 1) [10]. Table 1 lists some examples of porous materials in the catalysis and adsorption applications.

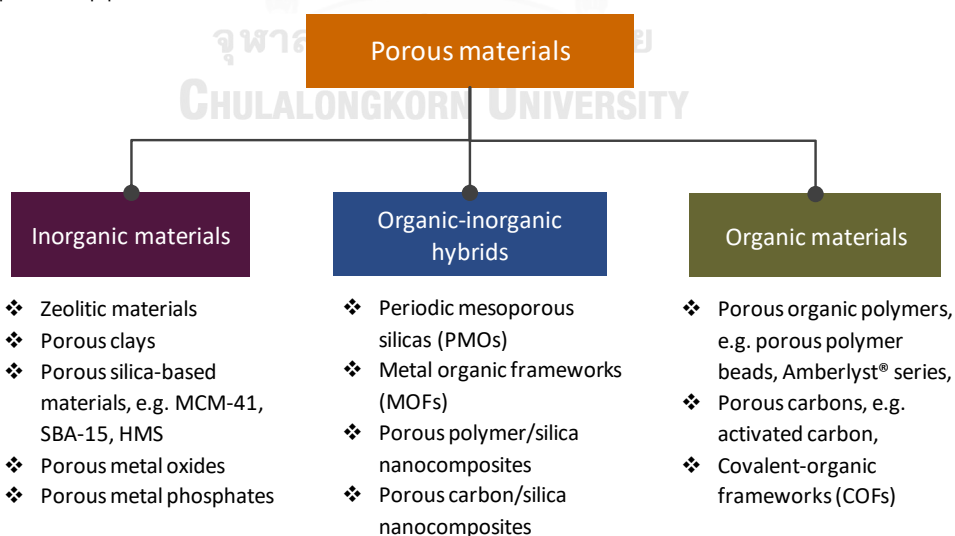


**Figure 2.1** Classification of porous materials based on their framework building blocks [10].

**Table 2.1** Examples of porous materials applied in catalysis and adsorption applications.

Porous material	Synthesis	Modification	Application
Zeolites	Hydrothermal	<ul style="list-style-type: none"> <li>- Dealumination</li> <li>- Impregnation</li> <li>- Ion exchange</li> <li>- Isomorphic substitution</li> </ul>	<ul style="list-style-type: none"> <li>- Acid catalysts</li> <li>- Basic catalysts</li> <li>- Adsorptive removal of water and small organic molecules</li> </ul>
Mesoporous silica	Sol-gel	<ul style="list-style-type: none"> <li>Impregnation</li> <li>Surface grafting</li> <li>Incorporation of metal atoms</li> </ul>	<ul style="list-style-type: none"> <li>Catalyst supports</li> <li>Functionalized catalysts for acid/base reactions</li> <li>Recovery of micronutrients</li> <li>Drug carriers</li> </ul>
Carbon-based materials	Carbonization	<ul style="list-style-type: none"> <li>Acid oxidation</li> <li>Impregnation</li> <li>Surface grafting</li> <li>Sulfonation</li> <li>Amination</li> </ul>	<ul style="list-style-type: none"> <li>Catalyst supports</li> <li>Acid catalysts</li> <li>Base catalysts</li> <li>Recovery of micronutrients</li> <li>VOC adsorption</li> <li>CO<sub>2</sub> adsorption</li> </ul>
Mesoporous polymer/silica nanocomposites (MPSs)	Templating sol-gel	<ul style="list-style-type: none"> <li>Impregnation</li> <li>Surface grafting</li> <li>Cross-linking</li> <li>Incorporation of metal atoms</li> </ul>	<ul style="list-style-type: none"> <li>Catalyst supports</li> <li>Acid catalysts</li> <li>Removal of micropollutants</li> <li>CO<sub>2</sub> adsorption</li> <li>Drug carriers</li> </ul>
Metal organic frameworks (MOFs)	Reticular synthesis	<ul style="list-style-type: none"> <li>Direct synthesis using different organic linkers and metal ions</li> <li>Ligand exchange</li> <li>Metal exchange</li> <li>Metal doping</li> </ul>	<ul style="list-style-type: none"> <li>Catalyst supports</li> <li>Acid catalysts</li> <li>Redox catalysts</li> <li>Enantioselective catalysts</li> <li>Selective adsorption</li> <li>Hydrogen storage</li> </ul>

## 2.2 Mesoporous silica materials

Mesoporous silica materials have received a lot of attention due to their excellent properties, including high specific surface area (600–1300 m<sup>2</sup>/g), large pore size (2–17 nm) and large pore volume (0.8–1.2 cm<sup>3</sup>/g), and so a high adsorption capacity. They also exhibit good thermal stability and are now available at lower cost. The synthesis of silica-based porous materials is carried out via surfactant-assisted templating sol–gel approach, so-called soft-templating chemistry, under varying range of pH, temperatures, and time. The surfactant templates act as structure-directing agents to determine the size and shape of pores. The structural and textural properties as summarized in Table 2.2, together with the synthesis condition.

**Table 2.2** Structural and textural properties of some mesoporous silicas.

Materials	Structure	Surface area (m <sup>2</sup> /g)	Pore size (nm)	Surfactant	Condition	Ref
MCM-41	2d-hexagonal	1207	3.4	CTAB	Base	[11]
MCM-48	Cubic	953	3.6	CTAB	Base	[11]
MCM-50	Stabilized Lamellar	340	3.5	CTAB	Base	[12]
SBA-15	2d-hexagonal	609	16.7	Pluronic P123	Acid	[13]
SBA-16	Cubic	755	11.7	Pluronic F127	Acid	[14]
HMS	Wormhole-like	917	2.1	DDA	Neutral	[9]

MCM-41, MCM-48, and MCM-48 can be prepared using cetyl trimethylammonium bromide (CTAB) as a template under basic conditions. Both SBA-15 as SBA-16 were synthesized in acidic condition of HCl in the presence of amphiphilic triblock copolymer surfactants Pluronic P123 and Pluronic F127, respectively. In case of HMS, primary amine was used as a template and can be prepared in neutral and environmental-friendly condition.



The mesoporous silica materials were prepared via sol-gel method. For example, the schematic representation of mechanistic pathways for the synthesis of mesoporous silica MCM-41 is shown in Figure 2.2 [15]. The original synthesis of the MCM-41 involves interaction between cationic surfactant ( $S^+$ ) and anionic species ( $I^-$ ) to generate assembled ion pairs ( $S^+I^-$ ). Generally, the surfactant template was dissolved in an aqueous basic solution. the cationic surfactant molecules organize to form spherical micelle and then transform into cylindrical shape under optimum conditions. After adding silica precursor, monomeric precursor is hydrolyzed into an anionic silicate, which then undergoes condensation into anionic silicate oligomer. The anionic silicate oligomers adsorb onto the external surfaces of micellar rod through electrostatic interactions ( $S^+I^-$ ). The cooperative self-assembly of anionic silicate species and cationic surfactant micelles into hexagonal structures was occurred together with the silica walls is generated by condensation of silicate species. The void of mesopores was generated after the After removal of surfactant template by calcination or solvent extraction.

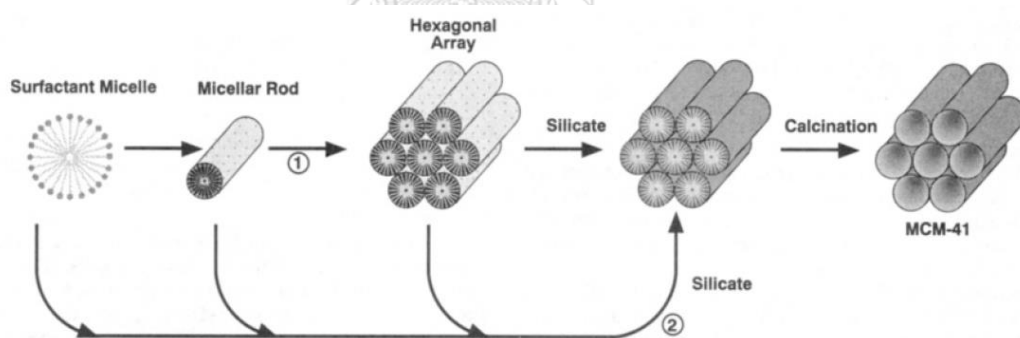


**Figure 2.2** Schematic representation of mechanistic pathways for the synthesis of MCM-41 [15].

## 2.3 Hexagonal mesoporous silica

### 2.3.1 General features

Hexagonal mesoporous silica (HMS) is a type of mesoporous silica that are prepared by neutral assembly pathway between a neutral primary amine surfactant and silica precursor under mild conditions, which was firstly found by Tanev and Pinnavaia (1996) [16]. They possessed wormhole-like or sponge-like framework structures as shown in Figure 2.3, a large surface area, and a narrow pore size distribution. Comparing HMS with other siliceous mesoporous materials with hexagonal framework structures, HMS exhibits the smaller particle sizes together with the randomly packed cylindrical pores that results in a high textural mesoporosity and enhanced intraparticle diffusion and adsorption [17]. Moreover, HMS revealed a thicker silica framework that results in a high thermal stability. Furthermore, the interactions between the primary amine molecules and the silicate occurred through hydrogen bonds. Therefore, the amine template can be easily removed by extraction using a solvent, such as acidic aqueous solution [18] and ethanol [16]. In addition, the silanol groups on HMS surface can be modified with organic functional groups for application in catalysis [19-21] and adsorption [22-24].

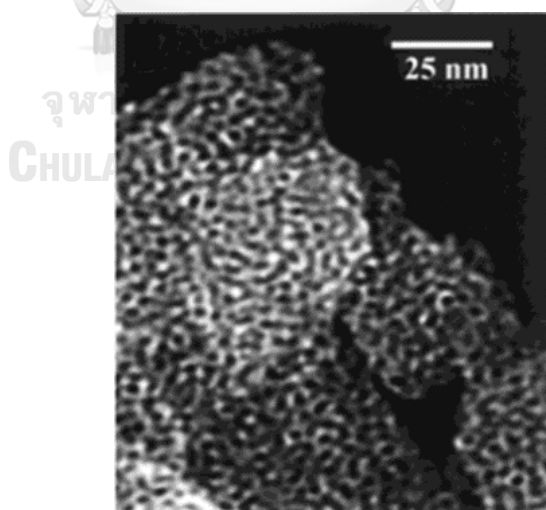
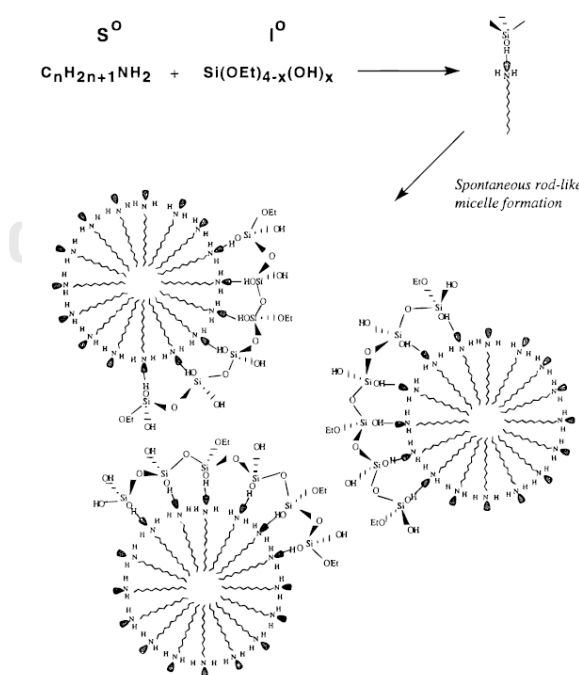


Figure 2.3 TEM image of HMS [25].

### 2.3.2 Synthesis of hexagonal mesoporous silica

The HMS was prepared using dodecylamine (DDA) as the organic template and tetraethyl orthosilicate (TEOS) as the silica via sol-gel process through neutral assembly route. The neutral assembly route ( $S^0I^0$ ) is the mesophases formation mechanism by interaction of neutral primary amine micelles ( $S^0$ ) and neutral or inorganic precursors ( $I^0$ ) through hydrogen bond. The schematic of synthesis pathway is illustrated in Figure 2.4 [16]. The DDA was dissolved in a polar solvent (e.g. ethanol or water). Micelles are formed in a polar solvent whereby the hydrophilic region (head group) of DDA molecules faces the outside surface of the micelle due to interaction between the hydrophilic region and the polar solvent through hydrogen bond, whereas the hydrophobic region (tail group) forms the core. After adding TEOS, the TEOS is hydrolyzed into a silicate and then condensation into silicate oligomers. The neutral silicate oligomers and neutral surfactant molecules (DDA) cooperatively self-assembled to form hexagonal structures, accompanied by silicate condensation, while the silica walls are built. The surfactants are removed by calcination or solvent extraction.



**Figure 2.4** Schematic representation of HMS mesoporous silica synthesis by neutral template ( $S^0I^0$ ) mechanism [16].

### 2.3.3 Applications of hexagonal mesoporous silica

The HMS is attractive support due to their high surface area, large pore volume and narrow pore size distribution. However, the application of HMS itself is limited due to the restriction in the active sites. Therefore, the incorporation of organo-functional group or metal substitution on the surface of HMS can provide the unique properties of HMS for various specific applications such as catalysis and adsorption. The advantages of the functionalization of these materials can provide the modified surface properties (such as hydrophilicity/hydrophobicity), thermal and structural stability [26].

Their chemical functionality is created by incorporating metal atoms into the siliceous framework or anchoring active functional groups onto the surface of silica, both of which can be done by either direct co-condensation or post-grafting method [27]. The functionalized materials attained by post-grafting method was performed by modification of the silica surface with organic functional groups through silylation reaction occurring on surface silanol groups (Si-OH) using trichloro- or trialkoxyorganosilane and silylamines as organic precursors as shown in Figure 2.5a. The direct co-condensation method is a one-step procedure in which the hydrolysis and the condensation of tetraalkoxysilane and trialkoxyorganosilane precursors through a sol-gel process in presence of an organic template (Figure 2.5b). Tetraalkoxysilane precursors act as the main silica framework, whereas the trialkoxyorganosilane precursors contribute to the adjusting of the silica framework and act as functional groups on the surface.

The co-condensation provides a better control of the loading and distribution of organo-functional groups, but it often produces materials with less ordered mesoporous structures. The post-grafting method exhibited a relative well-ordered functionalized mesoporous material, but it is limited by non-uniformly distributed organic moieties due to congregation of the organosilane on the channel pore mouth and on the exterior surface of the mesoporous materials that result in loss of surface area, pore size and pore volume [ref]. The advantages and disadvantages of post-grafting and co-condensation methods is summarized in Table 2.5.

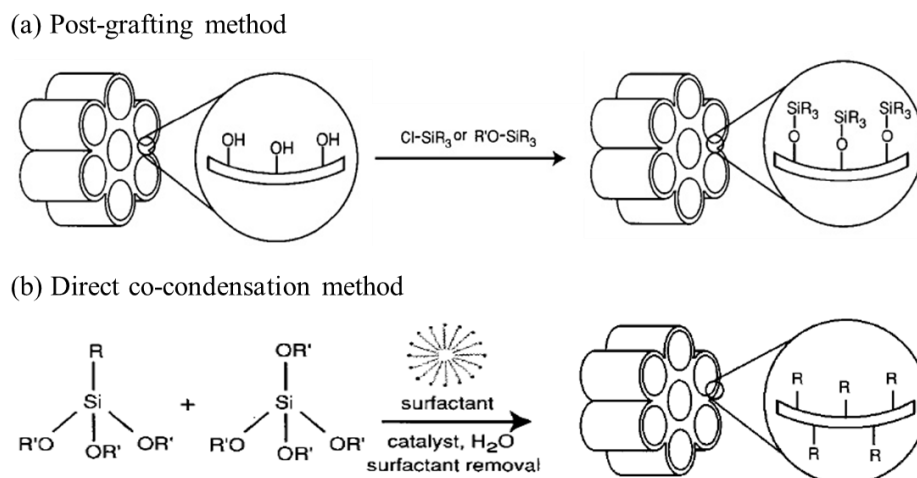


**Figure 2.5** Functionalization of surface of mesoporous silica by (a) post-grafting and (b) direct co-condensation methods using trialkoxyorganosilane [27].

**Table 2.3** Summary of advantage and disadvantage of two organic functionalized modification methods.

Post-grafting method	Co-condensation method
<p><b>Advantage:</b></p> <ul style="list-style-type: none"> <li>• Good preservation of the mesostructure after post-functionalization</li> </ul>	<p><b>Advantage:</b></p> <ul style="list-style-type: none"> <li>• Higher and more uniform surface coverage of functionality</li> <li>• Capable control in surface properties.</li> </ul>
<p><b>Disadvantage:</b></p> <ul style="list-style-type: none"> <li>• limited loading level of the functional groups can be grafted because of the limited density of the reactive surface silanols</li> <li>• Obtain low density and non-uniformity of functionality</li> <li>• Reduce pore size and pore volume</li> <li>• Time consuming</li> </ul>	<p><b>Disadvantage:</b></p> <ul style="list-style-type: none"> <li>• Loss in original structure ordering</li> </ul>

## 2.4 Mesoporous natural rubber/silica nanocomposites

### 2.4.1 General features

Recently, the successful synthesis of mesostructured nanocomposite constituted of natural rubber (NR) dispersed in the wormhole-like framework of hexagonal mesoporous silica (HMS), which is called NR/HMS [ref]. The NR/HMS composite is a new class of mesoporous polymer/silica hybrid materials that are synthesized via *in situ* sol-gel technique as showed in Figure 2.6. The NR/HMS have received considerable attention due to their high surface area, large pore volume and narrow pore size distribution, while the presence of natural rubber in mesostructured also enhanced hydrophobicity [9]. Moreover, the mesoporosity and hydrophobicity of NR/HMS can adjust by materials by varying type of primary amines (C8–C16) as templates [17]. These advantages make NR/HMS attractive for applications in catalysis and adsorption.

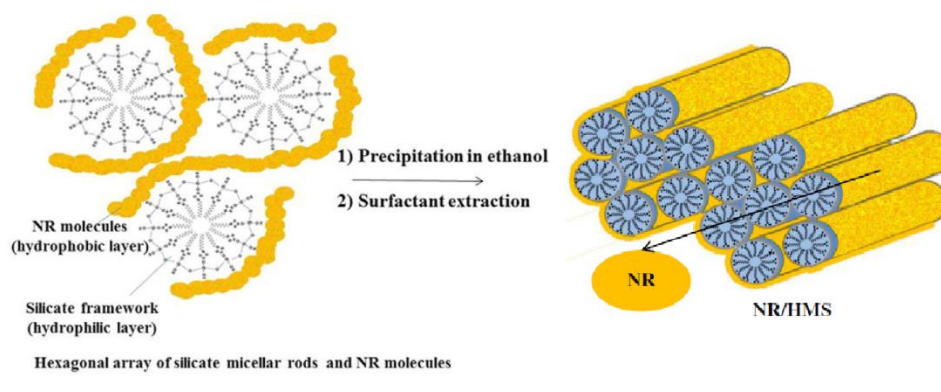


**Figure 2.6** Schematic representation of the formation of the hexagonal array of silicate micellar rods and NR [9].

### 2.4.2 Synthesis of NR/HMS nanocomposites

The of NR/HMS nanocomposites were prepared via the *in situ* sol-gel technique DDA (a neutral primary amine) as the organic template, TEOS as the silica source and tetrahydrofuran (THF) as the synthesis media. The dodecylamine added is not only a structure-directing agent for self-assembled silicate species, but the basicity of amine group also catalyzes the sol-gel reaction. The schematic of the formation of NR/HMS nanocomposite prepared with the pre-swelling step is illustrated in Figure 2.7 [28]. Firstly, the silica source was incorporated within NR sheet

through hydrophobic interaction between the ethoxy groups and the NR chains. The rubber chains were expanded by adding of THF and DDA and then NR solution was obtained. The addition of water hydrolyzed silica precursor to generate the silicate species simultaneously with a hybrid organic-inorganic mesophase formation by a cooperative self-assembly mechanism. Further condensation of the silicate species then allowed an aggregate of silica framework. The ethoxy groups of non-hydrolyzed silica precursor served as linkers between the rubber molecules and the silicate oligomers, which resulting in the dispersion of NR in mesostructured silica framework.

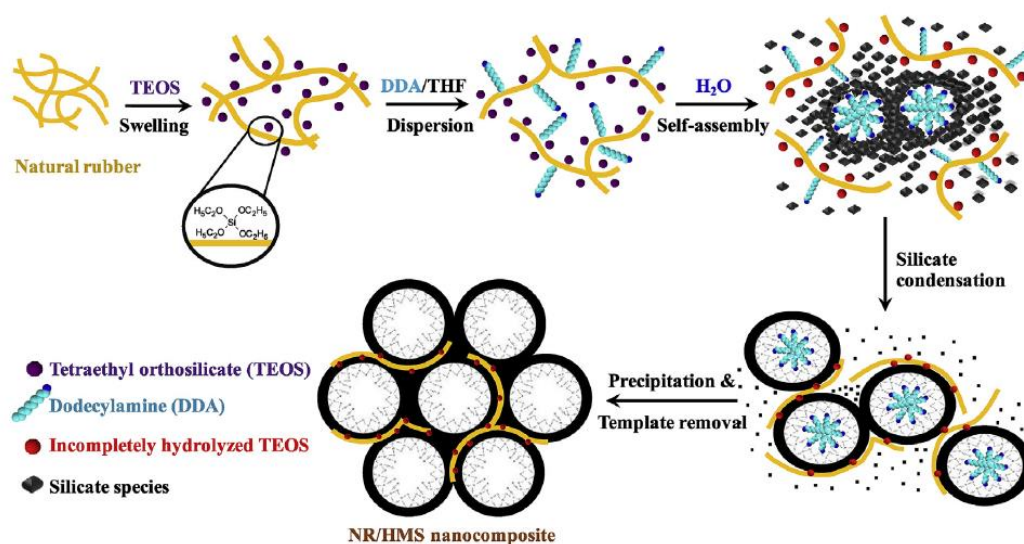


**Figure 2.7** The mechanistic model for the formation of NR/HMS nanocomposite prepared with the pre-swelling step [28].

### 2.4.3 Application of NR/HMS nanocomposites

The NR/HMS nanocomposites possesses genuinely mesostructured entrapped rubber/silica nanocomposite framework. The presence of rubber molecules in the resulting NR/HMS nanocomposite enhances framework hydrophobicity, while a high amount of surface silanol groups remains inside the mesopore channel [9]. The remaining surface silanol groups allow the composites to be modified with different active functional groups to prepare hydrophobic mesoporous materials serving catalysis and adsorption applications [20, 21, 29]. Consequently, the NR/HMS nanocomposite can be directly functionalized with propylsulfonic acid groups to obtain the mesostructured acid catalyst with hydrophobic properties as show in

Figure 2.8, which showed a high activity in the esterification of medium-to-long-chain fatty acids and palm fatty acid distillate with ethanol [20, 21].

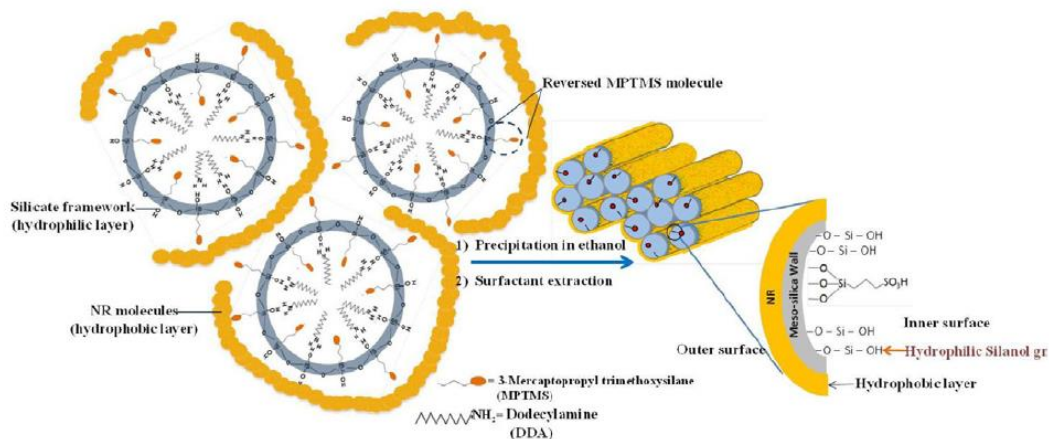


**Figure 2.8** Schematic representation of the formation of the hexagonal array of silicate micellar rods and NR in the presence of propylsulfonic acid groups [20].

## 2.5 Mesoporous carbon/silica nanocomposites

### 2.5.1 General features

The mesoporous carbon/silica nanocomposites (MCSs) are comprising of inorganic silica and organic carbon in its mesostructure. These nanocomposites have high surface area and porosity. The silica and carbon moieties in the structure provide advantages of both the inorganic silica, viz. the hydrophilicity and thermal/mechanical stability, and the organic component, viz. the hydrophobicity, capability of functionalization and facility to incorporate oxygen-containing functional groups such as carboxyl, lactone, and phenol as show in Figure 2.9 [7]. In other words, these types of nanocomposites combine the textural characteristics of mesostructured silica and the surface and hydrophobic properties characteristic of carbon materials. The mesoporous carbon-silica nanocomposites also have improved thermal, chemical, conductive, and mechanical properties. Confined-space effects inside the nanospace of mesostructures would certainly modify the unique chemical behaviors of polymer-silica and carbon/silica nanocomposites, which have inspired chemists and material scientists to create mesoporous nanocomposites. It would provide an opportunity to develop porous materials for specific applications, such as in catalysis,



adsorption, optics devices, energy storage, drug delivery, and sensors and electrodes [30].

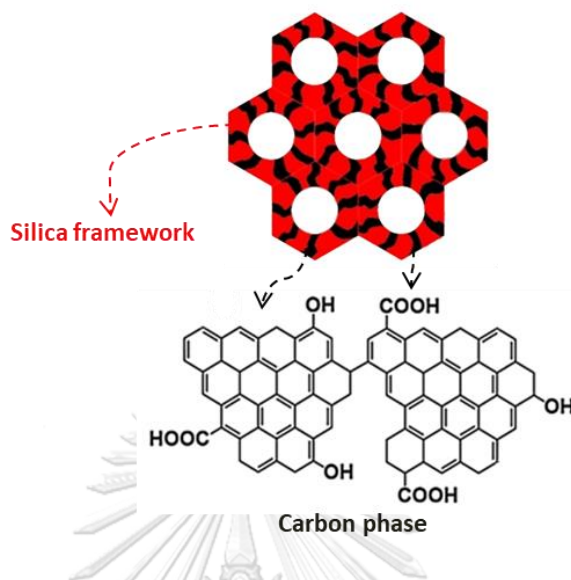


**Figure 2.9** Structural scheme of mesoporous carbon/silica nanocomposites. Red represents silica framework and black represents carbon phase [31].

### 2.5.2 Synthesis of mesoporous carbon/silica nanocomposites

The mesoporous carbon/silica nanocomposites have two reported synthetic strategies for deposition of carbon inside silica pores: (i) by means of a chemical vapor deposition (CVD) process, and (ii) by attaching organic moieties to the silica surface [7]. As a suitable carbon precursor, it should have the propensity to polymerize and show the resistance to decomposition during the carbonization process. Aromatic compounds, such as phenol-formaldehyde, and heteroaromatic compounds, such as furan derivatives from carbohydrates, are all suitable building blocks for carbonization. In addition, with the catalysis of acid, such as the non-volatile  $H_2SO_4$ , the P123 copolymer and even butanol can act as the carbon source [32].

The CVD process is one of the most common processes used to coat carbon onto silica surface as illustrated in Fig. 2.10. The CVD process involves depositing a solid material from a gaseous phase; this is achieved by means of a chemical reaction between volatile precursors and the surface of the materials to be coated. As the precursor gases pass over the surface of the heated substrate, the resulting

chemical reaction forms a solid phase, which deposited onto the substrate. The substrate temperature is critical and can influence the occurrence of different reactions [33]. Although the CVD method has been successfully applied to the synthesis of well-ordered mesoporous carbon/silica materials, this method is difficult to ensure a uniform carbon deposition.

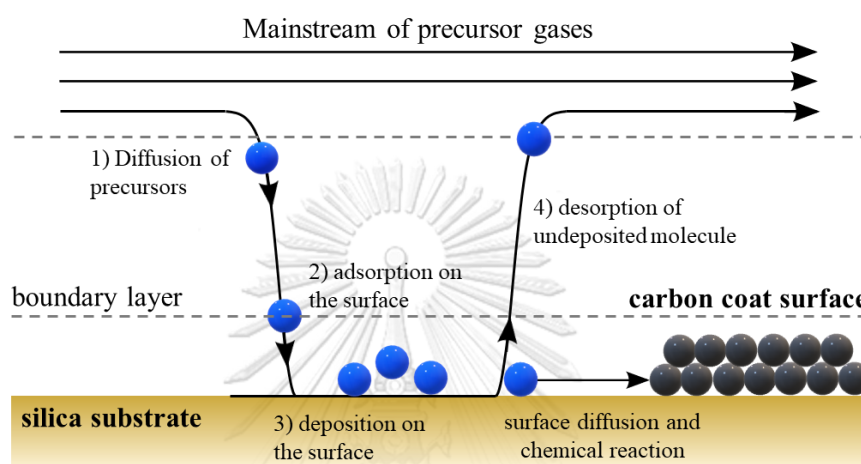


**Figure 2.10** Sequence of events during chemical vapour deposition (CVD).

The mesoporous carbon/silica nanocomposites were synthesized by attaching organic moieties to the silica mesostructure method, which have utilized a variety of carbon precursors such as furfuryl alcohol [8], glucose [34], and sucrose [35]. The amount of carbon precursor partial filling or coating the porous structure of silica and the porosity of the resultant carbon obtained determine the structural stability of mesostructured carbon after carbonization and upon the surface functionalization. Moreover, the nanocomposites obtained exhibit improved thermal and mechanical stability. However, this synthetic route is complex and involves numerous steps [7]. It is well-known that a surfactant-assisted templating sol-gel process is a useful technique to prepare a nanocomposite of organic and inorganic materials, so-called soft-templating chemistry, and the shape and size of a silica obtained can be controlled by the sol-gel reaction conditions such as range of pH, temperatures, and time. The self-assembled structure composed of template surfactant and carbon-silica precursor is directly used (Figure 2.11), which makes the synthesis simpler than the attaching organic moieties to the silica surface approach. Typically, the soft-

template molecules are block copolymers [36], which can be employed as a carbon source at the same time. The carbon precursors used in the soft-templating approach are those having a strong interaction, hydrogen bonding or electrostatic interaction, with one of the blocks of block copolymers and being polymerized around the template micelle. To obtain a mesoporous carbon/silica nanocomposite, the inorganic silica precursor is directly introduced into the self-assembled organic polymeric network. The abundant silanol groups ( $\equiv\text{Si}-\text{OH}$ ) of hydrolyzed silica precursor enhance interaction with the surfactant template, which assist in the organization into ordered mesostructures [37].

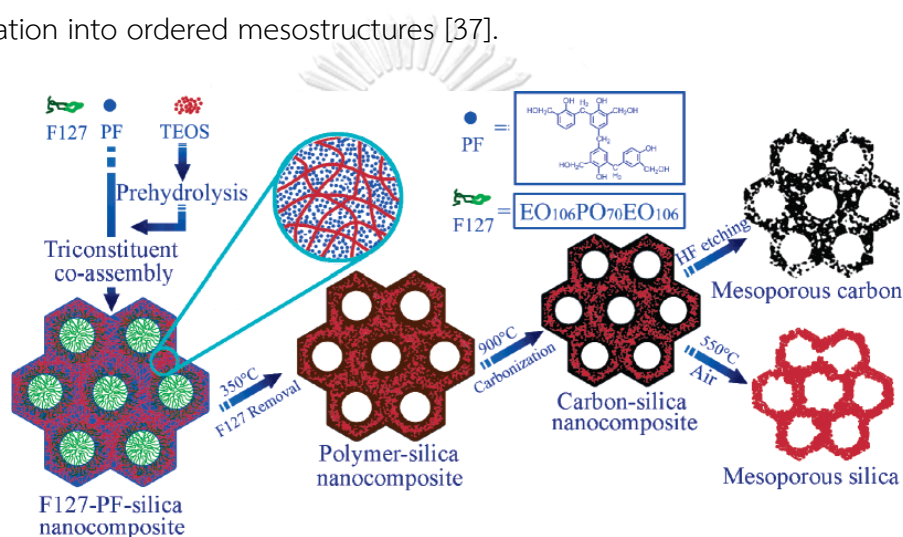


**Figure 2.11** Triconstituent co-assembly to ordered mesoporous carbon-silica nanocomposites [36].

### 2.5.3 Functionalization of carbon/silica nanocomposites

The mesoporous carbons and carbon/silica nanocomposites functionalized with sulfonic acid groups ( $-\text{SO}_3\text{H}$ ) are a class of heterogeneous acid catalysts, which exhibited good performance in several acid-catalyzed reactions, such as esterification, dehydration, and hydrolysis. The incorporation of chemically bound  $-\text{SO}_3\text{H}$  groups can be broadly divided into direct co-condensation and post-grafting approaches. There have been various sulfonating reagents, such as concentrated  $\text{H}_2\text{SO}_4$ ,  $\text{ClSO}_3\text{H}$ , 4-benzene-diazoniumsulfonate and MPTMS, used in the functionalization of mesoporous carbons and carbon/silica nanocomposites via post-grafting process, as

summarized in Figure 2.12. In the direct process, the carbon precursor is treated with concentrated  $\text{H}_2\text{SO}_4$  to produce the carbonaceous material bearing  $-\text{SO}_3\text{H}$  groups. For example, the aromatic compounds were heated in concentrated  $\text{H}_2\text{SO}_4$  as a one-step formation and incomplete carbonization of sulfoaromatic hydrocarbons. However, this method is highly dangerous and the resulting sulfonated carbons are not stable. The co-condensation of TEOS with organosilanes carrying S-containing terminal groups, such as 3-mercaptopropyltrimethoxysilane (MPTMS), is other direct approach to obtain the sulfonated silica material by one-step synthesis.  $\text{H}_2\text{O}_2$  is used as an oxidizing agent, which is directly added in the synthesis mixture, to convert the thiol groups into the  $-\text{SO}_3\text{H}$  moieties. This functionalization method is performed under mild conditions, but there is a limitation to achieve the acid catalysts with a high density of  $-\text{SO}_3\text{H}$  groups and well-ordered mesostructure, due to a hydrophobic nature of MPTMS itself. The post-grafting of mesoporous carbons and carbon/silica nanocomposites with MPTMS using cross-linking reactions with surface silanol groups or acidic oxygen functional groups is not as preferred as the direct co-condensation approach. It is due to a less stable anchoring, uneven distribution and decreased mesoporosity [32].

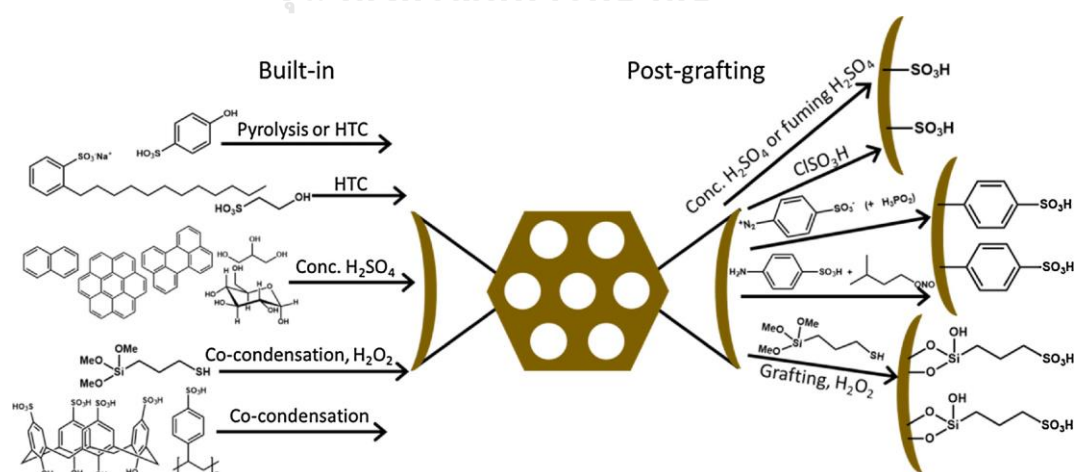


**Figure 2.12** Summary of possible ways that permit functionalization of the surface of carbon/silica nanocomposites with  $-\text{SO}_3\text{H}$  groups [32].

#### 2.5.4 Application of mesoporous carbon/silica nanocomposites in catalytic biomass conversion

The catalytic conversion of lignocellulosic biomass into fuels and platform chemicals involves multiple reactions, most of which are catalyzed by strong Brønsted acids [34, 38-41]. Many attempts have been made to develop heterogeneous catalytic processes for the biomass conversion with the aim of finding potential industrial applications. The sulfonated carbon/silica composites as an important class of H<sub>2</sub>O-tolerant strong Brønsted acid solid catalysts because of their high density of strong Brønsted –SO<sub>3</sub>H moieties. Moreover, the presence of oxygen containing functional groups, such as phenolic –OH and –COOH groups (Figure 2.13), on the carbon surface promotes the catalytic reactions by enhanced adsorption of reactants or synergistic catalytic function [42]. Their well-ordered mesostructure facilitates the molecular transport of large substrates and targeted products and controls the reaction selectivity. The hydrophobicity of carbon is beneficial to improve the stability of catalysts under hydrothermal conditions since the biomass conversion usually takes place in aqueous media. The surface hydrophobicity also facilitates the adsorption of reactant molecules and desorption of H<sub>2</sub>O formed as a dehydration by-product. The sulfonated carbon/silica composites have been widely applied for catalytic conversion of various biomass components to fuels and value-added chemicals via different reactions, including the liquid-phase up-grading of lignocellulose to biofuels and bio-based chemicals, including the hydrolysis of cellulose and hemicellulose to monomers and their conversion mainly via a furan platform.

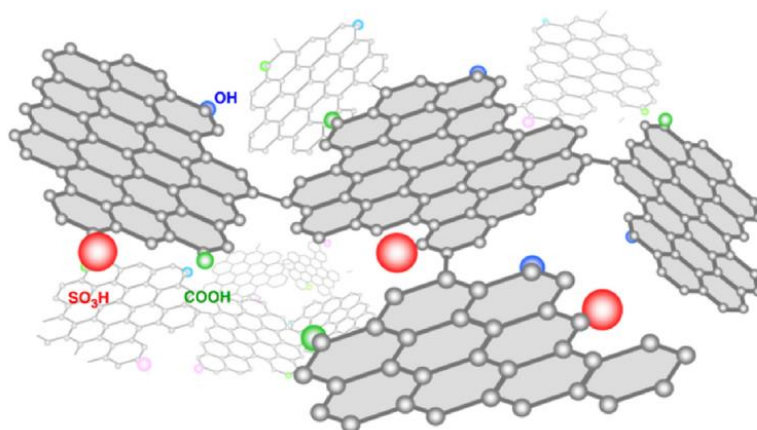


**Figure 2.13** Schematic representation of carbon structure and surface function group on carbon surface of sulfonated carbon/silica composites [42].

## 2.6 Biomass

Biomass is organic substance derived from plant or animal material. Plants produce carbohydrate molecules (starch and sugar) from carbon dioxide and water through photosynthesis for their growth and for their metabolic processes. The major biomass sources are agricultural and forestry residues, animal residues, sewage, algae, and aquatic crops (Fig. 2.14). Besides, Municipal solid waste and waste streams originating from human activities are also classified as a type of biomass. Therefore, the biomass is a promising alternative to petroleum resources in the carbon-based chemicals and fuel productions for transportation, electricity, and heat [43].



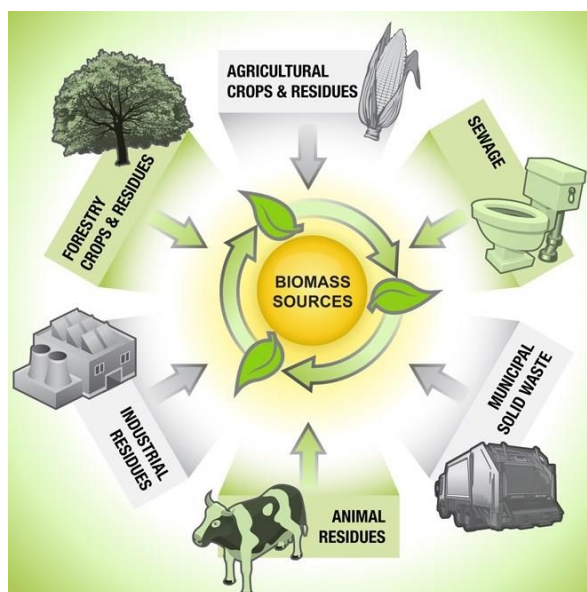


Figure 2.14 The major biomass sources [44].

### 2.6.1 Lignocellulosic biomass

Lignocellulosic biomass has attracted considerable attention as a sustainable alternative for fossil fuel to produce biofuels and other biobased chemicals due to the most abundant renewable biomass feedstock in the earth [45]. It can be found in agricultural wastes such as cereal straw and bagasse, forest residues such as pine and dedicated crops and short rotation coppices such as miscanthus, switchgrass and poplar [43]. Lignocellulose consists mainly of lignin, which is a three-dimensional polymer of phenylpropanoid units responsible for the structural rigidity of plants and that surrounds hemicellulose and cellulose (Figure. 2.15) [45, 46].

Cellulose ( $[C_6H_{10}O_5]_n$ ), the most abundant lignocellulose representing 40–60% in weight, is a polysaccharide consisting of a linear chain with a high molecular weight and a maximum of 10,000 monomeric units of D-glucose linked via  $\beta$ -(1,4) glycosidic bonds (Figure. 2.16) [43]. The cellulose chains are arranged together to form microfibrils, which are packed together to form cellulose fibrils. Cellulose fibrils are embedded in a lignocellulosic matrix that makes it very resistant to enzymatic hydrolysis [47].

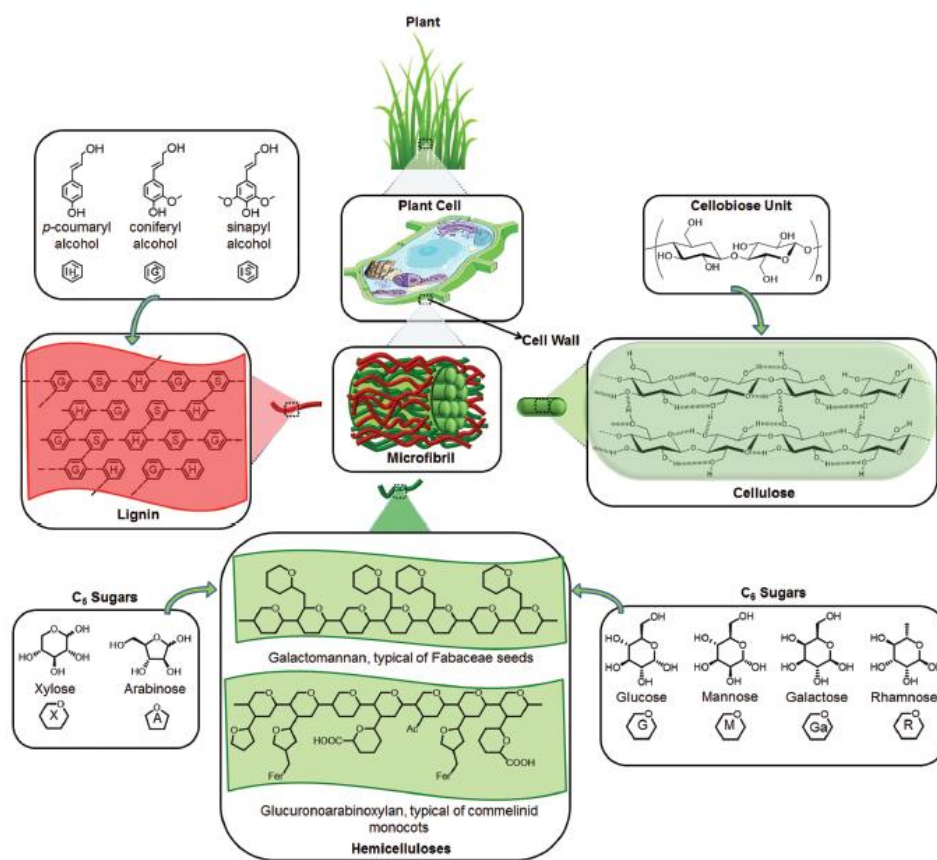


Figure 2.15 The main components and structure of lignocellulose [46].

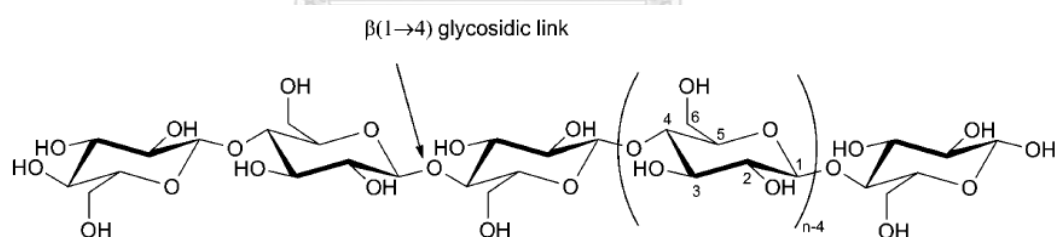
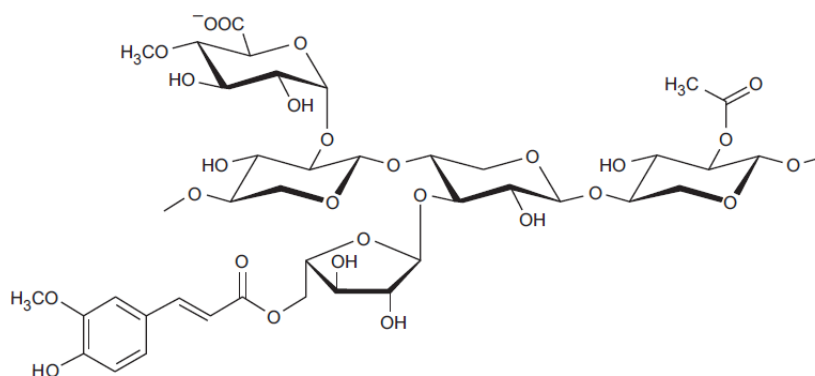


Figure 2.16 The structural formula of cellulose [48].

Hemicelluloses is comprising heterogeneous branching polysaccharides including pentoses (e.g. xylose and arabinose) and hexoses (e.g. mannose galactose and glucose) with an average molecular weight of  $<30,000$  as shown in Figure. 2.17, which may represent as much as 25-35% of lignocellulosic biomass [47, 49]. It is strongly bound with the surface of cellulose microfibril through hydrogen bonding. The content and structure of hemicellulose are different depending on the kind of



plant due to a different arrangement and proportions of sugar units. The thermal decomposition of hemicellulose mainly occurred between 180 °C and 350 °C, which produce the non-condensable gas, coal, and a variety of ketones, aldehydes, acids, and furans [43, 50].



**Figure 2.17** The structural formula of hemicellulose [51].

Lignin is a complex highly branched polymer of phenylpropanoid building units (*p*-coumaryl, coniferyl, and sinapyl alcohol) as shown in Fig. 2.18 [47]. The molecular weight of lignin was ranging from tens of thousands of Daltons to infinite, corresponding to 15–40% of lignocellulosic biomass [52]. The function of lignin as the cellular glue which provides compressive strength to the plant tissue and the individual fibers, stiffness to the cell wall and resistance against insects and pathogens [46].

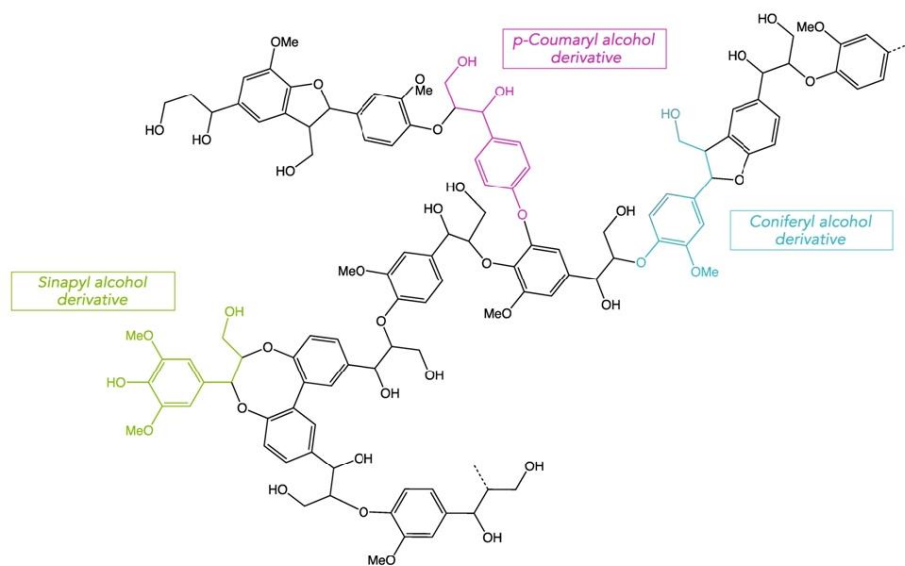


**Figure 2.18** The structural formula of lignin and its derivatives [43].

### 2.6.2 Conversion of lignocellulosic biomass into platform chemicals

Lignocellulosic biomass is promising renewable feedstock to produce value-added chemicals and biopolymers due to the chemistry of its major biocomponents such as cellulose, hemicellulose and lignin. Lignocellulosic biomass can be converted to valuable platform chemicals through chemical or biological routes (Fig. 2.19) [53]. The chemical route involves an initial depolymerization of the polysaccharides (cellulose and hemicellulose) to produce soluble hexose or/and pentose sugar, which is further converted to platform chemicals such as furfural, 5-hydroxymethylfurfural (HMF) and levulinic acid (LVA). These chemicals are used for the synthesis of fuel additives, liquid hydrocarbon fuels, biopolymers [45, 54]. The bioethanol is obtained from fermentation of sugar through biological routes. It is almost used as a fuel additive, whereas a small percentage is also used as a platform chemical for production of higher value-added products. Bioethanol can serve as a renewable source for production of ethylene, propylene, and butadiene, which are critical building blocks for polymer synthesis [55].

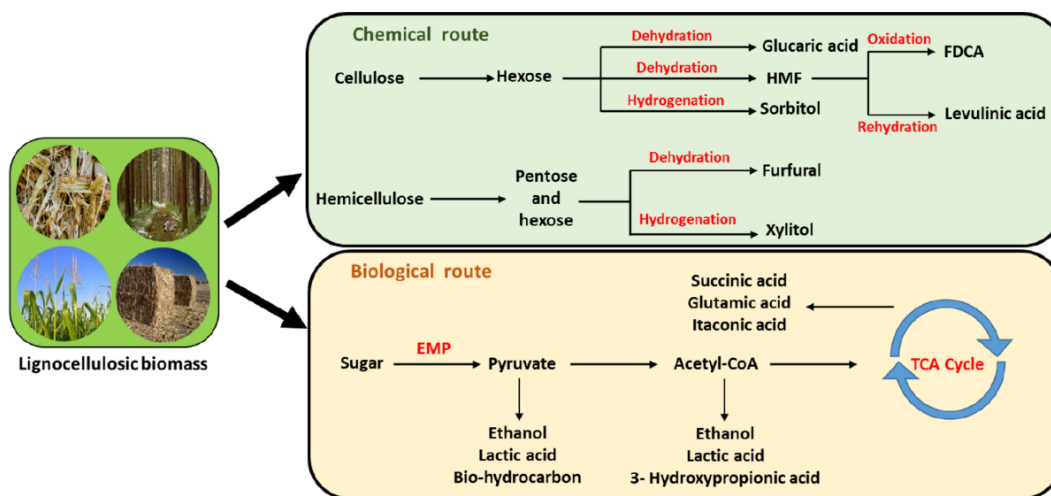


**Figure 2.19** Conversion routes for the platform chemicals produced from lignocellulosic biomass. [43].

## 2.7 Hexose

Hexose is a monosaccharide (simple sugar) with six carbon atoms. The chemical formula for all hexoses is  $C_6H_{12}O_6$ , and their molecular weight is 180.156 g/mol. Glucose and fructose are important hexoses for production of value-added chemicals. The glucose is aldohexoses, while fructose is a ketohexose [56]. The structures of glucose and fructose are shown in Fig.2.20.

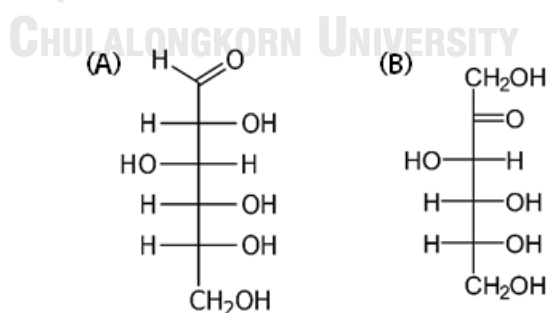


**Figure 2.20** The structures of (A) D-glucose and (B) D-fructose in a Fischer formular [56].

### 2.7.1 Glucose

Glucose or dextrose is the most common carbohydrate and classified as a monosaccharide with the molecular formula  $C_6H_{12}O_6$ , which is the most abundant

sugar found in nature. Glucose forms white or colorless solids that are highly soluble in water. It naturally occurs in fruits and honey [57]. The glucose is also produced via acid hydrolysis of cellulose through breakage of the  $\beta$ -1,4-glycosidic bonds as shown in Fig. 2.21 [58].

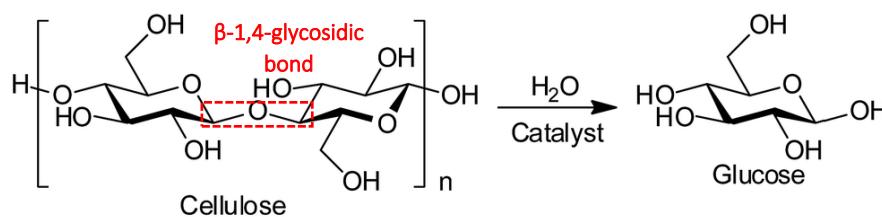


**Figure 2.21** Hydrolysis of cellulose in lignocellulose [58].

### 2.7.2 Fructose

Fructose, also known as fruit sugar, is a monosaccharide and an isomer of glucose. It naturally found in many fruits and other plant foods such as honey, sugar beets, sugar cane and vegetables [59]. The fructose is synthesized via isomerization of glucose using Brønsted bases, Lewis acids or enzymes as catalysts. The glucose isomerization to fructose in the presence of organic basic occurs through the Lobry de Bruyn–Alberda van Ekenstein (LdB–AvE) mechanism. In this mechanism, the C-2 proton on the acyclic form of glucose is abstracted by a Brønsted base, resulting in the formation of an enediol intermediate, and followed by hydrogen transfer from O-2 to O-1 and protonation of C-1 (Fig. 2.21) [60].

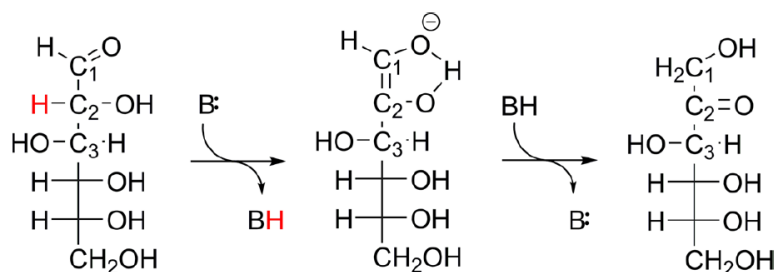


**Figure 2.22** Lobry de Bruyn–Alberda van Ekenstein (LdB–AvE) Mechanism for the Base-Catalyzed Isomerization of Glucose to Fructose [60].

### 2.7.3 Transformation of hexose into value-added chemicals

Hexose is one of the most important precursors for production of value-added chemicals through various catalytic processes. A notable commercialized reaction is the dehydration of glucose via fructose to HMF. HMF can be further convert into 2,5-furandicarboxylic acid (FDCA), which can substitute conventional petroleum-derived terephthalic acid. Moreover, fructose is also an intermediate to make other important value-added chemicals, such as levulinic acid and its esters, alkyl fructosides, and 5-ethoxymethylfurfural (Fig. 2.22) [61].

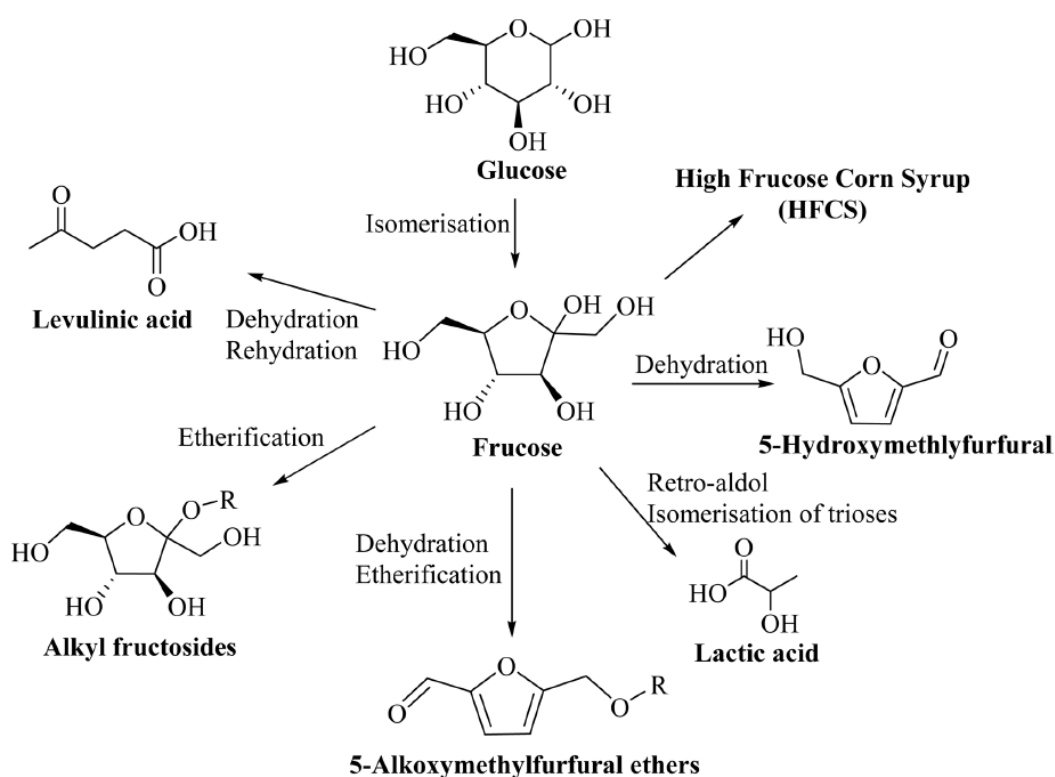


**Figure 2.23** Selective transformation of hexose into various chemicals [61].

### 2.7.4 5-hydroxymethylfurfural (HMF)

5-hydroxymethylfurfural (HMF) is a six-carbon heterocyclic organic compound consisting of a furan ring with both aldehyde and alcohol functional groups (Fig 2.23), which formed by the dehydration of hexose sugar [62]. The HMF is a white low-melting solid, but it is highly soluble in both water and organic solvents. The HMF is one of the top ten valuable bio-based chemicals listed by US Department of Energy,

as an important platform compound to produce fuel additives, liquid hydrocarbon fuels, biopolymers, and specialty chemicals (Table 2.3) [45, 54, 63].

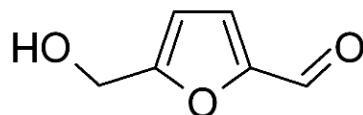


**Figure 2.24** The structural formula of HMF.

**Table 2.4** HMF derivatives and its industrial applications

Derivative	Molecular structure	Application
2,5-Diformylfuran (DFF)		Monomer, Fungicides, Pharmaceuticals
2,5-Dimethylfuran (DMF)		Biofuels
Levulinic acid (LVA)		Biofuels, Additives Pharmaceuticals, Solvent, Plasticizers, Herbicides
2,5-dihydroxymethylfuran (DHMF)		Polymers, Ethers
2,5-Dimethyltetrahydrofuran		Surfactants, Resins
2-Hydroxymethylfuran		Resins
2,5-Furandicarboxylic acid (FDCA)		Plasticizers, Polyesters, Polyurethanes

## 2.8 Synthesis of HMF using Brønsted acid-base catalyst

### 2.8.1 Conversion of glucose into HMF

Glucose, an abundant monosaccharide obtained from the depolymerization of cellulose, is further converted to HMF by two consecutive reactions (Fig.2.24). The first step is isomerization of glucose into fructose catalyzed by Brønsted base catalyst. The follow step is dehydration of fructose into HMF by Brønsted acid catalyst; Dehydration of fructose is facile and removes three water molecules. Selective formation of HMF is therefore highly desirable to establish successful bio-refinery. However, direct production of HMF from glucose via acid catalysts is unsuccessful because isomerization of glucose into fructose seems to be more difficult by acid catalysis. Moreover, many other reactions, such as rehydration of HMF into LVA, and formic acid (FA), esterification and condensation may occur under the action of acid catalysis as well, resulting in poor selectivity and considerable amounts [64]. The concept of site isolation can be realized by the coexistence of acid and base without neutralization, which has been demonstrated using acid–base pairs of polymers, sol–gel matrices, porous silicas, and layered clays.

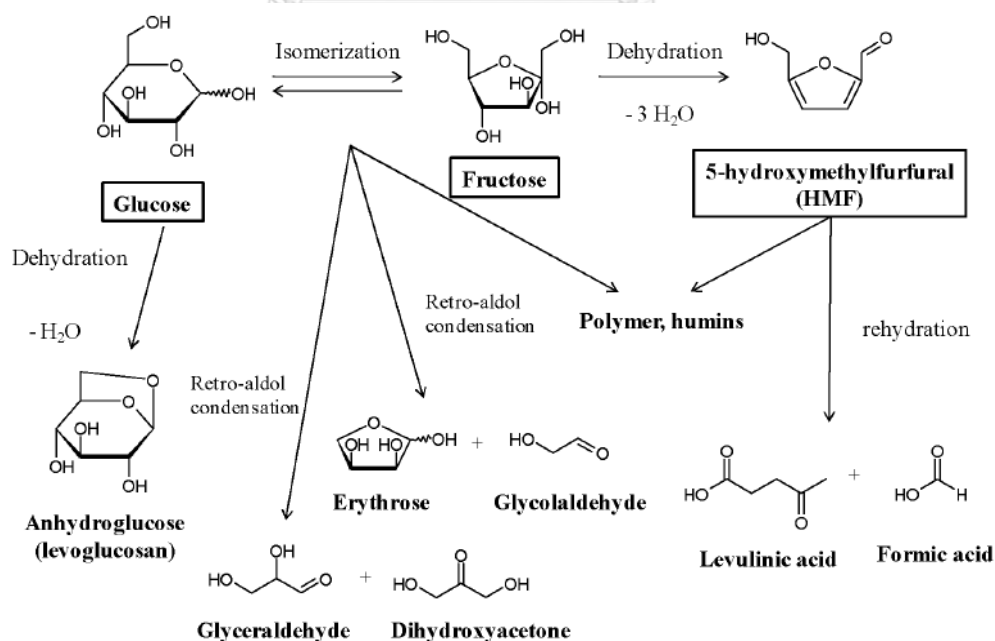


Figure 2.25 A typical reaction scheme for glucose transformation [6].

## 2.8.2 Homogeneous acid-base catalysts

The HMF synthesis from glucose have been investigated by using homogenous catalyst ( $\text{H}_2\text{SO}_4$  [65],  $\text{HCl}$  [65, 66],  $\text{CrCl}_3$  [3, 67], or  $\text{AlCl}_3$  [68]) in presence of different solvents. Generally, the homogeneous catalysts are present in the same phase as the reaction mixture, which enhanced reaction rate due to reduction of reactance diffusion limitations. Combination of homogeneous Brønsted base and acid catalysts ( $\text{H}_3\text{PO}_4/(\text{NH}_4)_2\text{HPO}_4$ , and  $\text{H}_3\text{PO}_4/\text{pyridine}$ ) actively promote high glucose conversion and HMF yield due to their high basicity and acidity for the glucose isomerization to fructose and fructose dehydration to HMF [5]. Nevertheless, the homogeneous acid catalytic system possessed several serious drawbacks, including high toxicity, corrosion, and difficulty of separation from the reaction mixture.

## 2.8.3 Heterogeneous acid-base catalysts

Heterogeneous catalysts have been used in the synthesis of HMF since they exhibit high selectivity to desired product under moderate conditions and provide several advantages, such as reusability and waste minimization [4]. However, in some cases, the reaction over the solid catalysts is subjected to mass transfer limitation. Several studies have been conducted to develop new solid catalysts and efficient catalytic systems that will increase the yields of desired chemical products.  $\text{Mg-Al}$  hydrotalcite, a layered double hydroxide [ $\text{Mg}_6\text{Al}_2\text{CO}_3(\text{OH})_{16}\cdot 4(\text{H}_2\text{O})$ ] displayed high activity for glucose to fructose isomerization. However, these catalysts still have poor HMF selectivity due to the presence of high strength of basic sites, leading to humin formation. Amberlyst 15, an acidic ion-exchange resin with high density of sulfonic acid group and high hydrophobicity, is an active catalyst in dehydration, however, its use is limited by low thermal stability (less than  $<140^\circ\text{C}$ ) and high cost [6].

## 2.8.4 Solvent systems

### 2.8.4.1 Monophasic solvent systems

Several reaction media have been used in the conversion of glucose into HMF. Water is usually the most preferred medium for these reactions due to less toxic and Environment friendly. However, the HMF synthesis from glucose under aqueous acidic conditions could rehydrate to undesired products such as levulinic



and formic acids as well as self-condensate to form both soluble polymers and insoluble humins. Therefore, the use of high-boiling organic solvents was employed to minimize the formation of undesired products and increase the HMF yield. For example, pure dimethyl sulfoxide (DMSO) exhibited high HMF yield of 90% in the presence of acid resins in fructose dehydration, whereas water media has been shown to give lower HMF yields of 60% [69]. However, the removal of these organic solvents and the purification of HMF may give rise to additional technical difficulties and to environmental problems. Moreover, glucose and fructose required a large amount of organic solvents to be dissolved due to their poor organic solubility, thus leading to low substrate concentration and consequently reduced productivity.

#### 2.8.4.2 Biphasic solvent systems

The biphasic systems (water/organic solvent) have been used in the synthesis of HMF with the purpose of solving the low solubility of sugars in organic solvents while the continuous extraction of formed HMF from the aqueous phase prevents its degradation as shown in Fig 2.25. Several experiments have been investigated for the catalytic dehydration of glucose to HMF in tetrahydrofuran/water (THF/H<sub>2</sub>O) biphasic reaction systems [4, 68, 70, 71]. The presence of NaCl can increase the partition coefficient of HMF in THF/H<sub>2</sub>O biphasic systems, which increases the HMF selectivity by removing it more efficiently from the reactive aqueous solution. NaCl is also useful in creating biphasic systems with solvents that are otherwise completely miscible with water, as well as increasing the upper critical solubility temperature of certain partially soluble solvents [70]. Moreover, the combination of NaCl and heterogeneous organic bases can promote glucose aqueous isomerization to fructose because the neutral salt-induced promotion could make the heterogeneous organic bases as efficient as the homogeneous organic bases [72].

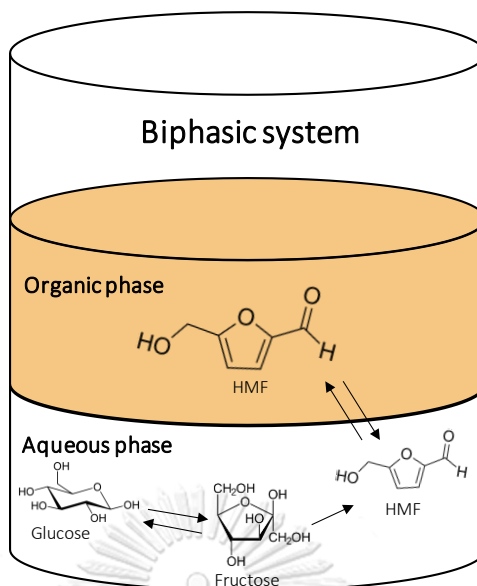


**Figure 2.26** Schematic diagram of a biphasic system for HMF production.

## 2.9 Literature reviews

### 2.9.1 Synthesis of polymer/silica and carbon/silica nanocomposites.

Nuntung *et al.* [9] prepared NR/HMS composites with a high structural order and mesoporosity via *in situ* sol-gel process. The incorporation of NR molecules into the mesoporous structure expanded the hexagonal unit cell and channel wall thickness. The surface of HMS was reduced amount of silanol groups by coverage of NR molecules. The NR/HMS composites exhibited high BET surface area, large pore volume and narrow poresize distribution. Moreover, the formation of the NR/HMS composites induced the agglomeration of HMS nanoparticles, resulting in an enhanced textural porosity and hydrophobicity.

Zhao *et al.* [36] prepared highly ordered mesoporous polymer-silica and carbon-silica nanocomposites with interpenetrating networks through the evaporation-induced triconstituent co-assembly method, wherein soluble resol polymer is used as an organic precursor, prehydrolyzed TEOS is used as an inorganic precursor, and triblock copolymer F127 is used as a template. The presence of silicates in nanocomposites dramatically inhibits framework shrinkage during the

calcination, resulting in highly ordered large-pore mesoporous carbon-silica nanocomposites.

### 2.9.2 Functionalized mesoporous carbon/silica with sulfonic group

Zhong *et al.* [32] synthesized mesostructured carbon/silica composites by using the classic evaporation-induced triconstituent coassembly method, wherein sucrose is used as carbon precursor, prehydrolyzed tetraethylorthosilicate as silica precursor, and Pluronic F127 as template. The resultant mesostructured silica-carbon nanocomposite was sulfonated to provide a strong acid catalyst with high sulfonic acid density, or the carbon phases of the nanocomposite can be removed by calcination to produce a silica material with ultrahigh porosity ( $V_{\text{pore}} = 1.25$  to  $1.34 \text{ cm}^3 \text{ g}^{-1}$ ). There have attributed to the higher  $\text{SO}_3\text{H}$  acid density ( $0.64$  to  $1.08 \text{ mmol g}^{-1}$ ), the larger and better communicating mesopores ( $V_{\text{meso}} = 0.38$  to  $0.82 \text{ cm}^3 \text{ g}^{-1}$ ) and the abundant presence of surface oxygen-containing functional groups on the vapor-phase assisted hydrothermally treated samples.

Nakajima *et al.* [73] prepared sulfonated amorphous carbon/silica composites for the selective dimerization of  $\alpha$ -methylstyrene. Partial carbonization and sulfonation of D-glucose impregnated SBA-15 resulted in the formation of a carbon/SBA-15 composite where  $\text{SO}_3\text{H}$ -bearing carbon with large surface area was incorporated into the mesopores of SBA-15. Bulky  $\text{SO}_3\text{H}$ -bearing carbon material prepared simply by the partial carbonization and sulfonation of D-glucose does not catalyze the dimerization of  $\alpha$ -methylstyrene at all because of the small surface area.

Zhang *et al.* [74] prepared sulfonated carbon/silica composites with surface areas of over  $600 \text{ m}^2 \text{ g}^{-1}$  and pore sizes of  $1.5$ – $2.2 \text{ nm}$  via incompletely carbonizing sucrose dispersed on MCM-48 and sulfonating the obtained carbon/MCM-48 composites. The pore sizes and catalytic activities of the sulfonated carbon-silica composites were adjustable by changing the amount of sucrose loadings and the

composites exhibited enhanced hydrothermal stability and amphiphilic property. When the sucrose loading was close to the monolayer dispersion capacity of sucrose on MCM-48, the resulting sulfonated carbon-silica composites exhibited surface areas of 700–724 m<sup>2</sup> g<sup>-1</sup>.

### 2.9.3 Catalysts in glucose conversion into HMF

Takagaki *et al.* [6] reported glucose dehydration to HMF catalyzed by a solid acid/base catalyst via one-pot reaction under mild conditions and using *N,N*-dimethylformamide (DMF) as solvent. Firstly, two individual reactions were screened to identify the best solid catalyst for both reactions. The base catalyst for the glucose isomerisation was Mg–Al hydrotalcite (HT), consisting of layered clays with HCO<sub>3</sub> groups on the surface. For the fructose dehydration Amberlyst 15 was chosen as the acid catalyst. The combination of these two solid catalysts improved the glucose transformation from zero selectivity to 76%, improving the conversion as well. Other substrates were tested also with high HMF yields.

Wu *et al.* [75] reported one-pot conversion of cellulose into HMF by solid acid/base catalyst. mesoporous silica nanoparticles functionalized with an sulfonic group (–SO<sub>3</sub>H) and amine group (–NH<sub>2</sub>) simultaneously. The immobilization of 3-mercaptopropyltrimethoxysilane on silica, followed by the oxidation of thiol groups (–SH) generated the –SO<sub>3</sub>H group, which were then grafted by 3-aminopropyltrimethoxysilane to produce the acid–base catalyst (LPMSN). The LPMSN catalyst was used for the one-pot conversion of cellulose into HMF in an ionic liquid ([EMIM]Cl), which includes the hydrolysis of cellulose into glucose, the isomerization of glucose into fructose and the dehydration of fructose into HMF. HMF was produced with a yield of around 15% after 360 min at 120 °C

Zhou *et al.* [76] reported synthesis of HMF from glucose was done in H<sub>2</sub>O, dimethylsulfoxide (DMSO) and 1-butyl-3-methylimidazolium chloride ([Bmim]Cl) catalyzed by metal (III) chloride. HMF yield in the different solvents follows a

decreasing order as  $\text{DMSO} > [\text{Bmim}]\text{Cl} > \text{H}_2\text{O}$ . The highest HMF yield is achieved by  $\text{FeCl}_3 \cdot 6\text{H}_2\text{O}$ , followed by  $\text{AlCl}_3$  and then  $\text{CrCl}_3 \cdot 6\text{H}_2\text{O}$ . An optimal condition is found at 393 K or 403 K and a time between 30 min and 480 min.



## Chapter 3

### EXPERIMENTAL AND ANALYTICAL METHOD

#### 3.1. Materials

##### 3.1.1 Chemical for synthesis mesoporous materials and composites

- Tetraethoxysilane (TEOS) ( $\text{SiC}_8\text{H}_{20}\text{O}_4$ ) (AR grade, 98%, Sigma Aldrich)
- Dodecylamine (DDA) ( $\text{CH}_3(\text{CH}_2)_{11}\text{NH}_2$ ) (AR grade, 98%, Sigma Aldrich)
- Tetrahydrofuran (THF) (AR grade, 99.5%, QREC)
- Natural rubber (NR) (commercial grade, STR-5L, Thai Hua Chumporn Natural Rubber Co., Ltd. (Thailand))
- Absolute ethyl alcohol ( $\text{C}_2\text{H}_5\text{OH}$ ) (AR grade, 99.5%, Merck)
- Sulfuric acid ( $\text{H}_2\text{SO}_4$ ) (AR grade, 95-98%, Sigma Aldrich)
- Argon gas (Ar) (IND Grade, 99.9%, Thai - Japan Gas)
- Toluene (AR grade, 99.5%, Wako Pure Chemical Industries, Ltd.)
- 3-aminopropyltrimethoxysilane (APS) ( $\text{H}_3\text{N}(\text{CH}_2)_3\text{Si}(\text{OCH}_3)_3$ ) (AR grade, 97%, Sigma Aldrich)
- 3-mercaptopropyltrimethoxysilane (MPS) ( $\text{HS}(\text{CH}_2)_3\text{Si}(\text{OCH}_3)_3$ ) (AR grade, 95%, Sigma Aldrich)
- $\text{H}_2\text{O}_2$  (AR grade, 30%, TCI)
- Deionized water (DI water)

##### 3.1.2 Chemical for HMF synthesis

- D-(+)-glucose ( $\text{C}_6\text{H}_{12}\text{O}_6$ ) (AR grade, TCI)
- D-(−)-fructose ( $\text{C}_6\text{H}_{12}\text{O}_6$ ) (AR grade, Kanto Chemical Co., Inc.)
- Tetrahydrofuran (THF) (AR, grade, 99.5%, Wako Pure Chemical Industries, Ltd.)
- Sodium chloride (NaCl) (1st grade, 99.9%, Wako Pure Chemical Industries, Ltd.)

### 3.1.3 Chemicals for reaction product analysis

- Methyl alcohol ( $C_2H_5OH$ ) (AR grade, Wako Pure Chemical Industries, Ltd.)
- Sulfuric acid ( $H_2SO_4$ ) (AR grade, >95%, Fluka)
- D-(+)-glucose ( $C_6H_{12}O_6$ ) (AR grade, TCI)
- D(-)-fructose ( $C_6H_{12}O_6$ ) (AR grade, Kanto Chemical Co., Inc.)
- Hydroxymethylfufural ( $C_6H_6O_3$ ) (AR grade, >97%, TCI)
- Luvulinic acid ( $C_5H_8O_3$ ) (AR grade, >97%, TCI)
- Furfural ( $C_5H_4O_2$ ) (AR grade, >98%, TCI)

### 3.2 Instruments and equipment

- Beaker (50, 100, 500 and 1000 mL)
- Laboratory glass bottle (250 mL)
- Glass dropper and rubber bulb
- Magnetic bar
- Glass burette (50 mL)
- Graduated cylinder (10 and 25 mL)
- Round-bottom flask (250 mL)
- Weighting paper
- Filter paper No.1
- Litmus paper
- Ailhn condenser
- Suction flask and Buchner funnel
- Stainless spatula
- Syringe and nylon syringe filter
- Autopipette and pipette tip
- Vial
- Volumetric flask (100 mL and 250 mL)

- Crucible
- Quartz block
- Quartz boat
- Watch glass
- Forceps
- Silicone oil bath
- Desiccator
- Aspirator pump
- Analytical balance
- hot-plate stirrer and thermocouple
- Centrifuge and centrifuge tube
- Electric oven
- Muffle furnace
- Horizontal tube furnace
- Teflon-lined stainless-steel autoclave (50 mL)
- Temperature-controller and heating tape

### 3.3 Preparation of pure silica HMS, NR/HMS and MCS nanocomposites

#### 3.3.1 Synthesis of hexagonal mesoporous silica (HMS)

The pure silica HMS was synthesized using DDA as structure directing agent and TEOS as silica source in the presence of THF as shown in Fig. 3.1. Firstly, 3.75 g of DDA was dissolved in 45 mL of THF. Subsequently, 53.05 mL of deionized water was slowly added into the DDA solution, followed by the dropwise addition of TEOS (10.5 g) with stirring. After 30 min, the mixture was aged in an oven at 40 °C for 24 h. The white solid product was recovered by filtration, thoroughly washed with ethanol, and dried at 60 °C for 12 h. Finally, the organic template was removed from the as-synthesized material by calcination at 350 °C, 450 °C or 700 °C each step was held for 1 h with a heating rate of 2 °C min<sup>-1</sup>. The Temperature program for calcination was shown in Figure 3.2.



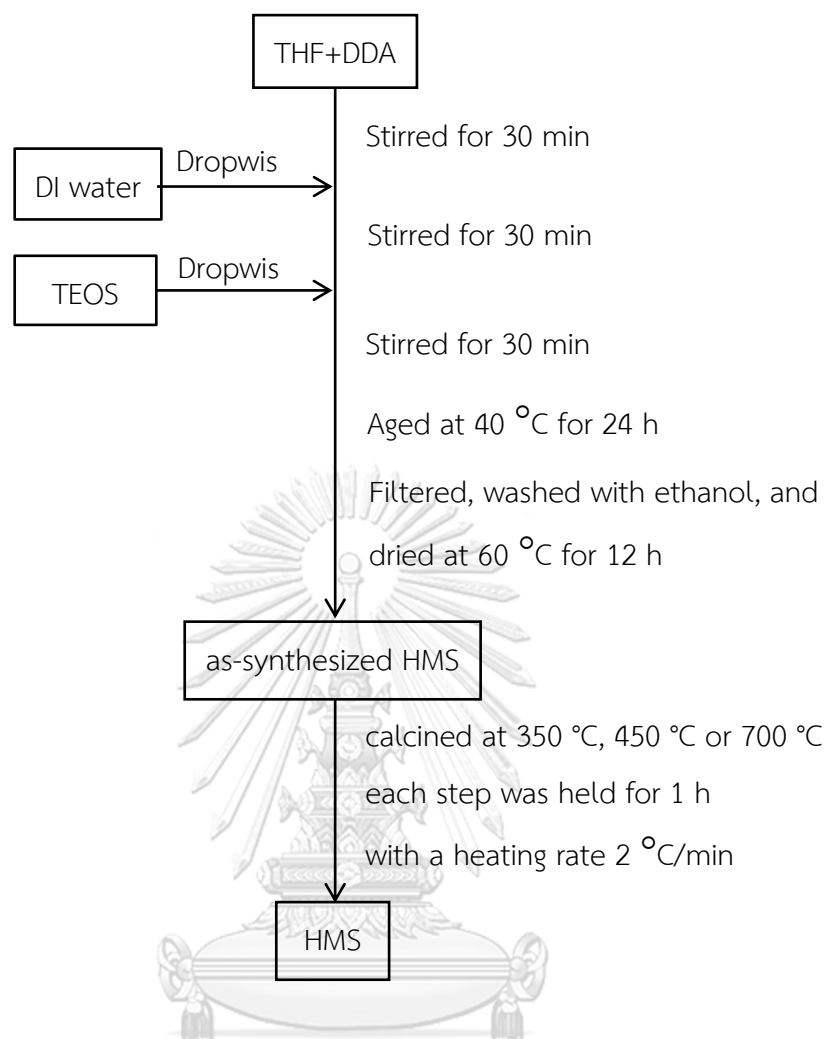


**Figure 3.1** Schematic diagram of HMS synthesis.

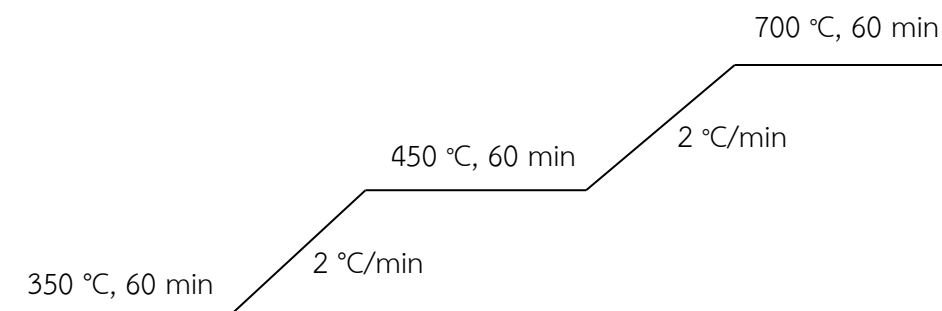


**Figure 3.2** Temperature program of muffle furnace condition for HMS calcination.

### 3.3.2 Natural rubber and hexagonal mesoporous silica nanocomposites (NR/HMS) synthesis

NR/HMS nanocomposites were prepared via an *in situ* sol–gel technique using DDA as organic template and TEOS as silica source, as previously reported [28]. First, 0.5 g of NR sheet was immersed in 8.5 g of TEOS at room temperature for 16 h. The resulting swollen NR was measured for the content of TEOS uptake ( $\approx 1.80$  g) and then stirred overnight in THF (45 mL) to obtain colloidal solutions. Afterwards, 3.75 g of DDA and 8.70 g of TEOS were sequentially added dropwise to the NR solution with stirring. After 30 min, deionized water was added slowly into the mixture and stirred for 1 h at 40 °C. The resulting gel was aged at 40 °C for 3 days and then precipitated in 50 mL of ethanol. The white powder (as-synthesized NR/HMS) was recovered by filtration, followed by drying at 60 °C for 24 h. The acid treatment was performed in a 0.05 M H<sub>2</sub>SO<sub>4</sub>/ethanol solution at 80 °C for 4 h. The resulting solid was filtrated and then further dried at 60 °C for 12 h. The yellow powder obtained was designated as “NR/HMS”.

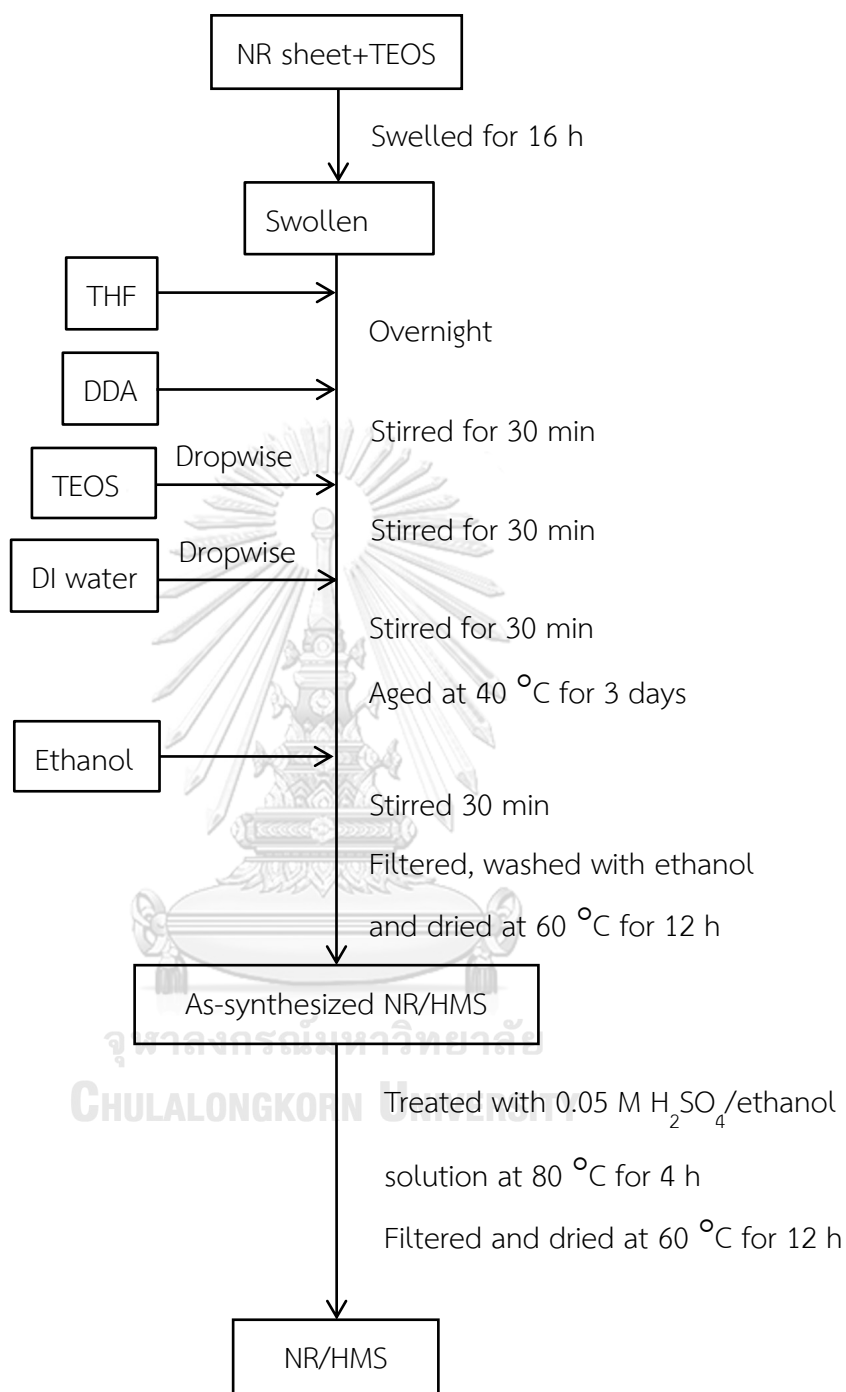


**Figure 3.3** Schematic diagram of NR/HMS synthesis.

### 3.3.3 Mesoporous carbon/silica nanocomposites (MCS) synthesis

MCS nanocomposites were prepared by the carbonization of acid-treated NR/HMS materials as shown in Fig 3.4.  $\text{H}_2\text{SO}_4$  adsorbed on the NR/HMS precursor was supposed to work as a catalyst for the conversion of rubber phase into carbonaceous moieties during the subsequent carbonization process. Carbonization was carried out in a tubular furnace under an argon flow. The temperature was increased at  $2\text{ }^\circ\text{C min}^{-1}$  to 350, 450, or  $700^\circ\text{C}$ , each of which was maintained for 1 h (Fig. 3.5). The obtained carbon/silica nanocomposites were designated as MCS-xG-yM-t, where  $x$  represents the initial NR content of the NR/HMS precursor (g),  $y$  represents the concentration of the  $\text{H}_2\text{SO}_4$ /ethanol solution (M), and  $t$  represents the final temperature of carbonization ( $^\circ\text{C}$ ). The synthesis conditions of MCS are summarized in Table 3.1.

**Table 3.1** Synthesis conditions of MCS material

Material	NR Content (g)	$\text{H}_2\text{SO}_4$ concentration (M)	Final temperature ( $^\circ\text{C}$ )
MCS-0.5G-0.05M-350	0.5	0.05	350
MCS -0.5G-0.05M-450	0.5	0.05	450
MCS-0.5G-0.05M-550	0.5	0.05	550
MCS-0.5G-0.05M-700	0.5	0.05	700
MCS-0.5G-0.05M-800	0.5	0.05	800
MCS-0.5G-0.50M-700	0.5	0.50	700
MCS-0.5G-1.00M-700	0.5	1.00	700
MCS-0.5G-1.50M-700	0.5	1.50	700
MCS-0.5G-2.00M-700	0.5	2.00	700
MCS-1.0G-1.00M-700	1.0	1.00	700
MCS-1.5G-1.00M-700	1.5	1.00	700

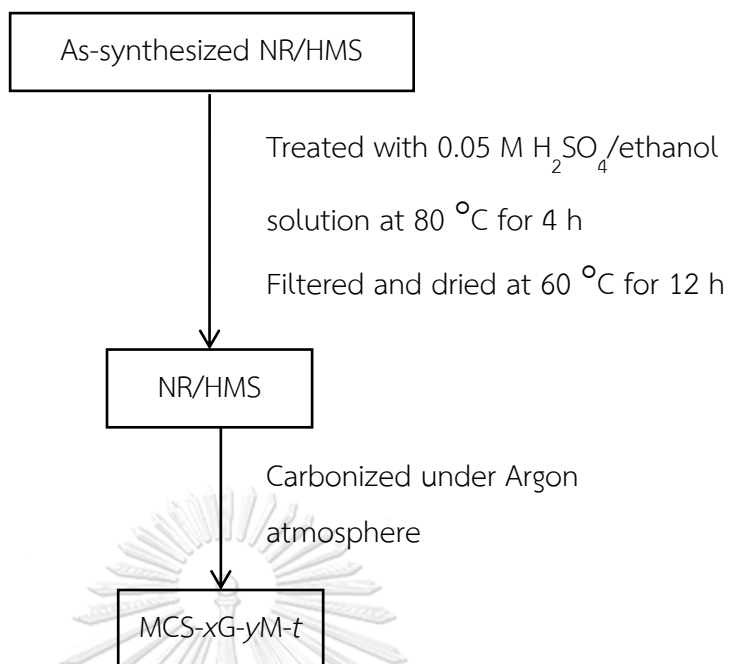


**Figure 3.4** Schematic diagram of MCS synthesis.



**Figure 3.5** Temperature program of tubular furnace condition for carbonization.

### 3.4 Functionalization of pure silica HMS and MCS nanocomposites

#### 3.4.1 Sulfonation of MCS nanocomposites (MCS-SO<sub>3</sub>H)

The sulfonated MCS nanocomposites (MCS-SO<sub>3</sub>H) were carried out performed via sulfonation by using a Teflon-lined stainless-steel autoclave (Fig. 3.6). 2.0 g of MCS-0.5G-1.00M-700 was mixed with aqueous H<sub>2</sub>SO<sub>4</sub> solution. Then, the mixture was heated to 150 °C and held for 12 h. Subsequently, the autoclave was cooled to room temperature. The solid was separated from the mixture by filtration, followed by washing with hot distilled water until the filtrate reached neutral pH, and then, it was dried at 100 °C overnight. The resultant MCS-SO<sub>3</sub>H samples are MCS-xS, where x represents the concentration of H<sub>2</sub>SO<sub>4</sub> solution. The synthesis conditions of MCS-SO<sub>3</sub>H materials were shown as Table 3.2.

**Table 3.2** Synthesis conditions of MCS-SO<sub>3</sub>H material

Material	H <sub>2</sub> SO <sub>4</sub> concentration (M)
MCS-10S	10
MCS-15S	15
MCS-18S	18

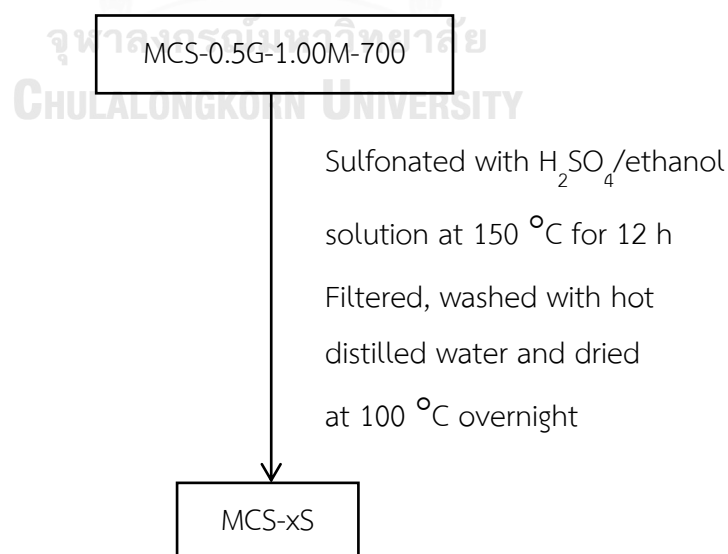


**Figure 3.6** Schematic diagram of MCS-SO<sub>3</sub>H synthesis.

### 3.4.2 Functionalization of MCS and MCS-SO<sub>3</sub>H with aminopropyl groups

The surface of bifunctional acid-base MCS nanocomposites (MCS-SO<sub>3</sub>H-NH<sub>2</sub>) was modified by post-grafting method using APS as aminosilane coupling agent. In a typical procedure, 1 g of MCS-18S was well dispersed in 40 mL of dried toluene. APS was then added into the mixture, followed by heating and refluxing at 110 °C for 24 h. The APS concentrations were used in a varied concentration of 0.1, 0.2, and 0.3 M. The resulting solid product was recovered by filtration, thoroughly washed with toluene, and dried at 100 °C overnight. The MCS-SO<sub>3</sub>H-NH<sub>2</sub> resulting sample was designated as MCS-18S-yN, where y representing the concentration of APS in solution. For preparation of amino-functional MCS nanocomposites (MCS-NH<sub>2</sub>), the MCS were refluxed in a 0.2 M APS solution using the same grafting process described above. The resulting samples was designated as MCS-0.2N.

**Table 3.3** Synthesis conditions of MCS-SO<sub>3</sub>H-NH<sub>2</sub> and MCS-NH<sub>2</sub> material

Material	APS concentration (M)
MCS-18S-0.1N	0.1
MCS-18S-0.2N	0.2
MCS-18S-0.3N	0.3
MCS-0.2N	0.2

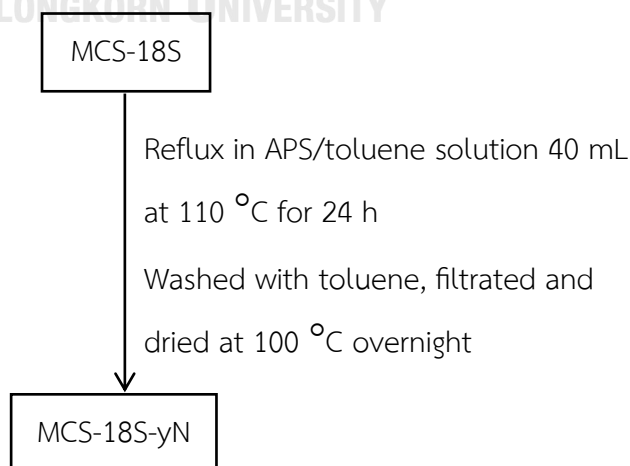


**Figure 3.7** Schematic diagram of MCS-SO<sub>3</sub>H-NH<sub>2</sub> synthesis.

### 3.4.3 Functionalization of HMS with organo-sulfonic acid and aminopropyl groups

First, the calcined HMS was functionalized using an organo-sulfonic acid group by the post-grafting method, using MPS as a functional group precursor. Before the grafting, HMS was dried at 100 °C for 24 h to remove adsorbed moisture. 1 g of the HMS was mixed with 40 and 1.4 mL of dried toluene and MPS, respectively. The mixture was heated and refluxed at 110 °C for 24 h. The resulting solid (HMS-SH) was recovered by filtration, followed by washing with toluene and drying at 100 °C overnight. The HMS-SH (0.5 g) was added to the mixture of hydrogen peroxide (10 mL), deionized water (10 mL), and methanol (10 mL). The solid product was filtered, washed with deionized water several times, and dried under a vacuum, after stirring the mixture at room temperature for 12 h. The resulting sample was denoted as HMS-SO<sub>3</sub>H. For the preparation of bifunctional acid-base HMS (HMS-SO<sub>3</sub>H-NH<sub>2</sub>), APS was grafted onto HMS-SO<sub>3</sub>H, following the procedure described in Section 3.4.2.

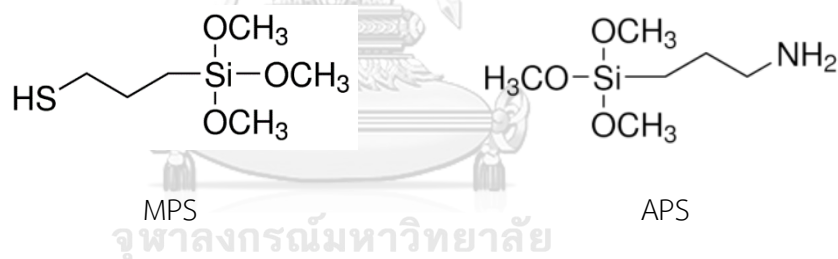
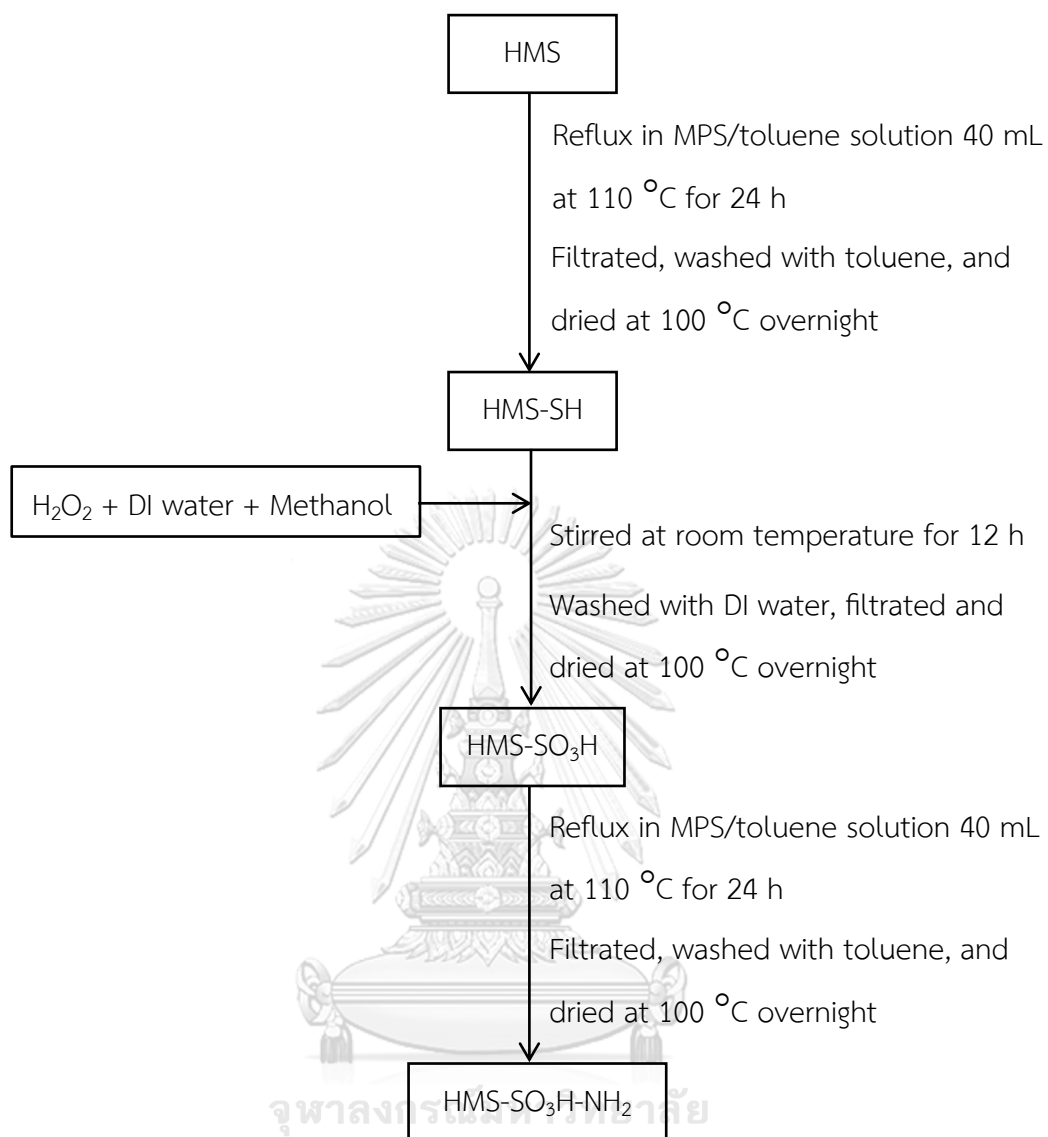


Figure 3.8 Chemical structure of MPS and APS.





**Figure 3.9** Schematic diagram of HMS-SO<sub>3</sub>H-NH<sub>2</sub> synthesis.

### 3.5 Characterization of Materials

#### 3.5.1 Structural analysis

##### *X-ray Powder diffraction (XRD)*

X-ray powder diffraction (XRD) is a powerful nondestructive technique for phase identification and structural parameter determination of crystalline solids. The monochromatic beam of X-rays diffracted on lattice planes of sample at specific angles to obtain X-ray diffraction peaks. The peak intensities are determined by the atom positions within a lattice structure. XRD can reliably investigate the mesostructure of the mesoporous materials. Generally, the XRD pattern of the (100) plane of a hexagonal mesostructure appears at a 2-Theta angle in the range of 0.5–3 degree.

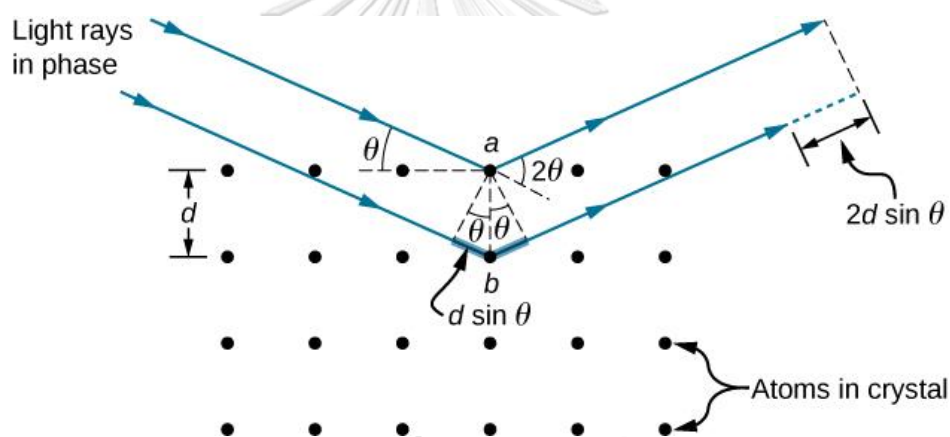


Figure 3.10 Diffraction of X-ray by regular planes of atoms.

Figure 3.9 shows a monochromatic beam of X-ray incident onto the crystal surface at an angle  $\theta$ . The scattered intensity is measured as a function of scattering angle  $2\theta$ . The scattering of X-rays provides a diffraction pattern, which contains structural information of materials. The interplanar spacing of the samples was determined using Bragg's law using the equation 3.1.

$$n\lambda = 2d \sin \theta \quad (3.1)$$

Where the integer  $n$  is a positive integer,  $\lambda$  is the wavelength,  $d$  is the spacing between the planes (the  $d$ -spacings) and  $\theta$  is the reflected angle.

Powder X-ray diffraction (XRD) was used to investigate the mesostructure ordering of synthesis nanocomposites. The XRD patterns were recorded on a Bruker D8 ADVANCE diffractometer equipped with Cu  $K\alpha$  radiation generated at 40 kV and 40 mA. The measurement was performed over a  $2\theta$  range of  $0.5\text{--}10^\circ$  with a scanning step of  $0.02^\circ$  and a count time of 1 s. The interplanar spacing of (100) plane ( $d_{100}$ ) was calculated according to Bragg's equation. The repeating distance ( $a_0$ ) between pore centers of the hexagonal structure was calculated using the formula:  $a_0 = 2d_{100}/\sqrt{3}$ .

### ***Raman spectroscopy***

Raman spectroscopy is a molecular spectroscopic technique, which utilizes the interaction of light with matter to gain insight into a material characteristic. The photons are dispersed or scattered at the same energy as the incident photons when light interacts with molecules in a gas, liquid, or solid. The Raman spectroscopy provide information by light scattering process. Raman spectroscopy is a commonly technique used to acquire information about the structural aspect of carbonaceous materials.

Raman spectroscopy was used to reveal the carbon structure of the MCS nanocomposites. Prior to the analysis, the sample powder was dried at  $100^\circ\text{C}$  overnight to reduce the adsorbed moisture. Raman spectra were collected on a JASCO NRS-5100 laser Raman spectrometer with a laser wavelength of 532 nm. Each sample was placed across a glass slide, and each spectrum was recorded for 5 scans.

### ***Small-angle X-ray scattering (SAXS)***

Small-angle X-ray scattering (SAXS) is a powerful technique that uses to study structural characterization of both ordered and disordered materials in solution. SAXS provides information about the size and shape of nanostructures with characteristic lengths up to several hundred nanometers. The SAXS experiments are typically performed on synchrotron sources to produce high-brightness X-rays. The monochromatic X-ray beam hits the sample and the radiation scattered at low

angles is recorded by a detector. The scattered intensity of X-rays is measured as a function of scattering angle.

Small-angle X-ray scattering (SAXS) experiment was applied to investigate the formation of the mesophase with synthesis gels during the synthesis of NR/HMS. The SAXS measurement was performed on a Beamline 1.3W using 1.2 GeV synchrotron light source at Siam Photon Laboratory, Synchrotron Light Research Institute, Thailand. The synchrotron light originated from a bending magnet was monochromatized using a Double Multilayer Monochromator to provide an X-ray energy of 9 keV. A toroidal mirror was used to focus the X-ray to the sample position. The experimental station was equipped with a charge-coupled device.

### **3.5.2 Compositional and elemental analysis**

#### ***Thermogravimetric/differential thermal analysis (TG/DTA)***

The thermal decomposition pattern and carbon content of nanocomposites was measured by thermogravimetric/differential thermal analysis (TG/DTA) using a Rigaku Thermo Plus thermogravimetric analyzer. The sample (~10 mg) was heated from room temperature to 1000 °C at a heating rate of 10 °C min<sup>-1</sup> under a dry air flow of 50 mL min<sup>-1</sup>.

#### ***Carbon, Hydrogen, Nitrogen and Sulfur (CHNS) analysis***

The amount of nitrogen and sulfur in the synthesis materials was determined using an Elementar Vario Micro Cube CHNS elemental analyser. The sulfanilic acid was used as standard calibration reagent with average value of 6 data to obtain corrective factor. Each sample (about 2 mg) was used analysing and corrected data with the corrective factor.

### **3.5.3 Textural properties and hydrophobicity measurement**

#### ***N<sub>2</sub> adsorption-desorption measurement***

The N<sub>2</sub> adsorption-desorption technique is applied to classify the porous materials and determine surface area, pore volume, pore diameter and pore-size distribution of materials. Gas adsorption by a porous material is described by an adsorption isotherm, the amount of surface adsorbate by the material at a fixed temperature as a function of pressure. Porous materials are typically characterized in

terms of pore sizes derived from gas sorption data. The IUPAC classification of adsorption isotherms is showed in Figure 3.10.

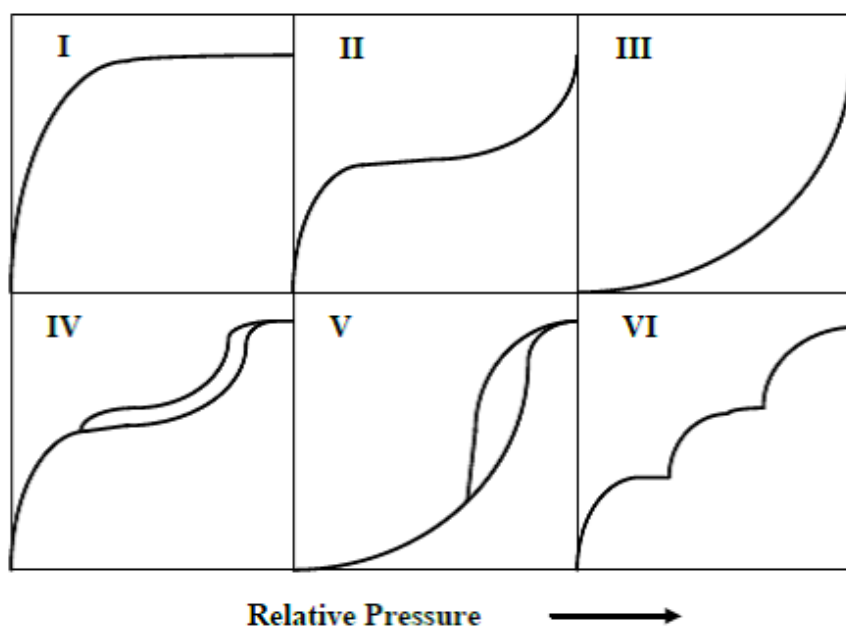


**Figure 3.11** The IUPAC classification of adsorption isotherm.

Brunauer–Emmett–Teller (BET) theory is most frequently used to determine the total surface area of solid or porous materials using the equation in 3.2

$$\frac{1}{W[(P_o/P)-1]} = \frac{1}{W_m C} + \frac{C-1}{W_m C} (P/P_o) \quad (3.2)$$

Where  $W$  is the weight of nitrogen adsorbed at a given relative pressure ( $P/P_o$ ),  $W_m$  is the weight of gas as monolayer, and  $C$  is a constant that is related to the heat of adsorption. The BET equation strictly describes a linear plot of  $1/((P_o/P)-1)$  vs.  $P/P_o$ , usually in the  $P/P_o$  range of 0.05 to 0.35. A slope and intercept are used to determine the quantity of nitrogen adsorbed in the monolayer and calculate the surface area.

Nitrogen ( $N_2$ ) adsorption–desorption measurement was carried out at  $-196$  °C a were determined at  $-196$  °C using a BEL Japan BELSORP mini II instrument to determine the textural properties of the synthesized materials. The sample was pretreatment at  $150$  °C for 2 h prior to the measurement. The specific surface area ( $S_{BET}$ ) was calculated from the adsorption branch data in the  $P/P_o$  range from 0.05 to

0.3 using the BET method. The total pore volume ( $V_t$ ) was obtained from a single point on the adsorption branch at a  $P/P_0$  of about 0.99. The external surface area ( $S_{\text{ext}}$ ) and primary mesopore volume ( $V_p$ ) were estimated using the  $t$ -plot method. The pore size ( $D_p$ ) was calculated from the adsorption branch data according to the Barrett-Joyner-Halenda (BJH) equation.

#### ***H<sub>2</sub>O adsorption-desorption measurement***

H<sub>2</sub>O adsorption measurement was applied to determine the hydrophobicity of HMS and representative nanocomposites was determined using H<sub>2</sub>O adsorption measurement. The weight of the sample used (initially around 60 mg) was measured exactly after degassed at 150 °C for 2 h. The measurement was performed using a BEL Japan BELSORP-max instrument at 25 °C. The monolayer adsorbed volume ( $V_m$ ) of H<sub>2</sub>O was determined from analysis of adsorption data at a relative pressure below 0.2.

#### **3.5.4 Surface functional groups analysis**

##### ***Fourier-transform infrared spectroscopy (FTIR)***

Fourier transform infrared spectroscopy (FTIR) was used to study the chemical functional groups of the materials. A self-supporting disk of each sample (20 mm diameter, 40 mg) was placed at the center of a quartz cell connected to a conventional closed gas-circulation system. The sample was pretreated by evacuation at 150 °C for 1 h to remove the adsorbed moisture. The FTIR spectra were collected under evacuation at room temperature in transmission mode on a JASCO FT/IR-4100 spectrometer with a Mercury Cadmium Telluride (MCT) detector with total of 64 scans over 400–4000  $\text{cm}^{-1}$  at a resolution of 4  $\text{cm}^{-1}$ .

##### ***X-ray photoelectron spectroscopy (XPS)***

X-ray photoelectron spectroscopy (XPS) is a surface quantitative technique based on the photoelectric effect to determine the surface elemental composition and the chemical or electronic state of these elements in the material. XPS normally probes to a depth of 10 nm. XPS spectra provide the relative frequencies of binding energies of electrons detected, measured in electron-volts (eV). XPS data is given in a plot of intensity versus binding energy. The binding energies are used to identify the

elements to which the peaks correspond, which can provide information about the surface functional groups of the material.

X-ray photoelectron spectroscopy (XPS) was used to investigate the surface functional groups of the materials using ESCA 1700R system equipped with Al K $\alpha$ 1 radiation (1486.8eV). The sample was dried by oven at 100 °C for 24 h to remove the adsorbed moisture. The high-resolution XPS spectra of C1s, O1s, N1s, S2p, and Si2p spectra were collected and calibrated to standard binding energy (BE) at C1s of 284.6 eV. Curve-fitting of XPS spectra was performed with the OriginPro 8.5 software.

*Solid-state <sup>29</sup>Si magic angle spinning nuclear magnetic resonance (<sup>29</sup>Si MAS NMR) and <sup>13</sup>C cross-polarization magic angle spinning nuclear magnetic resonance (<sup>13</sup>C CP/MAS NMR)*

Nuclear Magnetic Resonance (NMR) has established itself as a major and unique analytical tool in the characterization on the structural features of solid materials. In case of organo-functionalized mesoporous materials, the presence of organo-sulfonic acid groups or/and aminopropyl groups on the material surface and silica structure are confirmed using Solid-state <sup>29</sup>Si nuclear magnetic resonance. Solid-state <sup>13</sup>C cross-polarization Magic Angle Spinning Nuclear Magnetic Resonance (<sup>13</sup>C CP/MAS NMR) has been applied to characterize the structure and dynamics of solid materials such as polymers, biopolymers, and catalysts.

In solid-state NMR, the NMR spectrum of a powder sample contains very broad peak due to effects of anisotropic or orientation-dependent interactions. The presence of broad NMR line shapes results in lack of resolution of the NMR spectrum, which obscures any information. Therefore, magic angle spinning (MAS) is a technique often used to applied in solid-state NMR spectroscopy to remove the effects of chemical shift anisotropy and to assist in the removal of heteronuclear dipolar coupling effects, resulting in high-resolution NMR spectrum. Cross polarization (CP) also used to reduce or eliminate the broadening line in a solid-state NMR spectrum, which allows for the high-resolution acquisition of NMR spectra from solid samples.

Solid-state  $^{29}\text{Si}$  magic-angle spinning (MAS) nuclear magnetic resonance (NMR) and  $^{13}\text{C}$  cross-polarization (CP) MAS NMR spectroscopy were used to study the relative concentration of the silica and carbon species present in the representative catalysts, respectively. The  $^{29}\text{Si}$  NMR MAS and  $^{13}\text{C}$  CP/MAS NMR spectra were acquired using a JEOL-ECA600 NMR spectrometer at frequency of 79.4 MHz with 4 mm zirconium oxide rotor and a sample spinning frequency of 15 kHz. A single-pulse method was used to analyze the  $^{29}\text{Si}$  MAS NMR with a recycle delay time of 60 s. For  $^{13}\text{C}$  CP/MAS NMR, the experiments were conducted using the recycle delay of 5 s, and the CP contact time of 2 ms. The chemical shift of polydimethylsiloxane (PDMS) was referenced to both  $^{29}\text{Si}$  NMR MAS and  $^{13}\text{C}$  CP/MAS NMR spectra. Curve-fitting analysis, using OriginPro 8.5 software, was used to determine the relative peak area of each silica species.

### **3.5.5 Morphology and microstructural analysis**

#### ***Field-emission scanning electron microscopy (FE-SEM)***

Field-emission scanning electron microscopy (FE-SEM) was used to observed sample morphology. The FE-SEM images were obtained on a Hitachi SU5000 instrument at an accelerating voltage of 40 kV. The sample powder was dispersed on carbon tape, followed by platinum coating.

#### ***Transmission electron microscopy (TEM)***

Transmission electron microscopy (TEM) was used to directly observe the mesoporous structure of materials. The TEM images were recorded at a magnification of 100,000 $\times$  using a JEOL JEM-2010F transmission electron microscope at operated at 200 kV.

### **3.4.6 Acidity and basicity measurement**

The acid and base amounts of the representative catalysts were measured using back acid-base titration. 40 mg of the sample was dispersed in 20 mL NaOH aqueous solution (0.01 M) while stirring at room temperature for 6 h. The solid phase was subsequently filtered off, and the filtrate was titrated with 0.01 M HCl aqueous solution. For basicity measurement, the sample was stirred in an HCl aqueous



solution before titrating with NaOH aqueous solution. The acidity and basicity were calculated using equation (3.3) and (3.4), respectively.

$$N_{\text{acid}} = \frac{0.01 \times (20 - V_{\text{HCl}})}{1000 \times W} \quad (3.3)$$

$$N_{\text{base}} = \frac{0.01 \times (20 - V_{\text{NaOH}})}{1000 \times W} \quad (3.4)$$

where  $N_{\text{acid}}$  and  $N_{\text{base}}$  are the acidity and basicity ( $\text{mmol g}^{-1}$ ),  $V_{\text{HCl}}$  and  $V_{\text{NaOH}}$  are the volume consumptions of HCl and NaOH solution, respectively, during the titration (mL), and  $W$  is the weight of catalyst (mg).

### 3.6 Catalytic performance of MCS catalysts

#### 3.6.1 Study on the effect of functionalized HMS and MCS as catalyst

Dehydration of fructose or glucose was performed in a biphasic solvent (aqueous NaCl solution/THF) using a 50-mL Teflon-lined stainless-steel autoclave equipped with a temperature-controlled heating tapes and magnetic stirrer. The composite catalyst was dried at 150 °C for 2 h prior to use. Typically, 0.18 g of sugar substrates and 1.8 g of NaCl was dissolved in deionized water, corresponding to the sugar substrate concentration of 0.2 M. Subsequently, THF was added to the substrate solution, follow by an addition of catalyst with stirring. Other typical operating parameters were volume ratio of organic phase and aqueous phase of 2 and catalyst loading of 100 mg. Zero time was recorded when the mixture temperature reached the target value. The mixture was then held at this temperature for a set period. After reaction, the autoclave was rapidly cooled down in an ice bath to stop the reaction. The reaction mixture was filtered to remove the solid catalyst before the quantitative analysis by high performance liquid chromatography (HPLC).

#### 3.6.2 Study on the effect of reaction temperature and time

The effect of reaction temperature and time was studied as procedure in Section 3.6.1 in glucose conversion using MCS-SO<sub>3</sub>H-NH<sub>2</sub> as catalyst. The effects of reaction conditions were carried out at three different temperatures (150, 170 and 190 °C) for 5-360 min. The reaction conditions were glucose concentration of 200

mM, volume ratio of organic phase and aqueous phase of 2 and catalyst loading of 100 mg.

### 3.6.3 Study on the effect of catalyst amount

The effect of catalyst amount was studied as procedure in Section 3.6.1 in glucose conversion using MCS-SO<sub>3</sub>H-NH<sub>2</sub> as catalyst. The amount of catalyst was varied from 10 to 200 mg. The reaction was carried out at 190 °C for 60 min. In addition, the glucose concentration was used at 200 mM with a volume ratio of organic phase and aqueous phase of 2.

### 3.6 Catalyst reusability of MCS-SO<sub>3</sub>H-NH<sub>2</sub> composite

After the glucose dehydration in Section 3.6.1, the MCS-SO<sub>3</sub>H-NH<sub>2</sub> was recovered by a filtration and washed with water and acetone to remove the organic phase covering on their surface from each reaction cycle, and then dried at 100 °C overnight before a new cycle was started with fresh reactants.

### 3.7 Reaction product analysis

The sugar substrates and water-soluble products in the aqueous phase were analyzed using a high-performance liquid chromatography (HPLC) apparatus (Shimadzu, LC-20A series), equipped with ROA-Organic Acid H<sup>+</sup> (8%) column (Phenomenex) at 50 °C and refractive index detectors. The eluent with a flow rate of 0.5 mL min<sup>-1</sup> was 5 mM H<sub>2</sub>SO<sub>4</sub> solution. Furfural, HMF, and other products in the organic phase were quantified with an ultraviolet detector (260 nm) using another HPLC apparatus (Shimadzu LC-10A) equipped with a Gemini C18 column (Phenomenex) at 75 °C in the presence of 80:20 H<sub>2</sub>O: methanol solution, as the eluent with a flowing rate of 0.5 mL min<sup>-1</sup>. The chromatograms of standard solution are shown in APPENDIX B.

The quantification of sugar substrates and products was performed using internal standardization calibration. 2-Butanone and 5-methyl-2-furaldehyde were used as internal standard for aqueous phase and organic phase, respectively. First, Aqueous phase was diluted to 10 times with deionized water. Afterward, 0.15 mL of 0.2 M 2-butanone solution was added to 2.85 mL of diluted aqueous solution prior to the HPLC analysis. For organic phase, 0.3 mL of 1 M 5-methyl-2-furaldehyde/THF

was added into the liquid sample and then analyzed product. The calculation of conversion, product yield, product selectivity and turnover number (TON) can be seen in APPENDIX C.



## Chapter 4

### SYNTHESIS AND CHARACTERIZATION OF MCS COMPOSITES

In this Chapter, mesoporous carbon/silica (MCS) nanocomposites using natural rubber (NR) as source were studied. A series of mesoporous nanocomposites based on NR and hexagonal mesoporous silica (HMS), prepared via an *in-situ* sol gel process, were used as precursors, which were then converted into the MCS materials by controlled carbonization. Effects of the carbonization temperature, concentration of sulfuric acid ( $H_2SO_4$ ) solution used in the pretreatment step, and the initial NR content of the NR/HMS precursors on the physicochemical properties and hydrophobicity of MCS materials were investigated as described in Chapter III. The MCS materials were characterized by a well-ordered mesostructure, high mesoporosity, and enhanced hydrophobicity.

#### 4.1 Thermogravimetric/differential thermal analysis (TG/DTA)

The weight loss and differential thermal analysis (DTA) curves of HMS, NR/HMS, and MCS-0.5G-0.05M-x series prepared at different carbonization temperatures are shown in Figure 4.1. In all cases, the first-step weight loss between 30 and 120 °C was due to the loss of the physisorbed water. The pure silica HMS revealed very little weight loss in the region of 200–600 °C. For NR/HMS, the second step, as the major weight loss at ~17 wt.%, occurred at 150–420 °C and was attributed to the decomposition of NR incorporated into the mesostructured silicate framework. More precisely, the change in DTA curve in this region was classified into two sub-steps: the first one (150–265 °C) corresponded to the melting temperature of NR [77], while the latter step (270–420 °C) was ascribed to the decomposition of the HC chain of NR in the silicate structure [78]. The small weight loss (~7 wt.%) in the range of 420–650 °C was related to the rubber-derived carbon residue [9] and the dehydroxylation of the silicate network [22]. The content of carbon present in the MCS nanocomposites was calculated from the weight loss of the carbon residue in

the 450–650 °C region, and the results are summarized in Table 4.1. Some rubber fractions remained in the resulting nanocomposite, as deduced from the weight loss between 270–420 °C, when the carbonization was performed at 350 °C (MCS-0.5G-0.05M-350). The decomposition step disappeared at a carbonization temperature of 450 °C. A small weight loss of 1–3 wt.% was observed in the range 250–450 °C for MCS-0.5G-0.05M-450 and corresponded to the decomposition of oxygen-containing functional groups, such as carboxyl, carbonyl, and hydroxyl groups [79, 80]. As shown in Table 1, the carbon content of the MCS composites prepared at 550–800 °C was insignificantly different (3.3–3.5 wt.%) and not affected by the increased carbonization temperature.

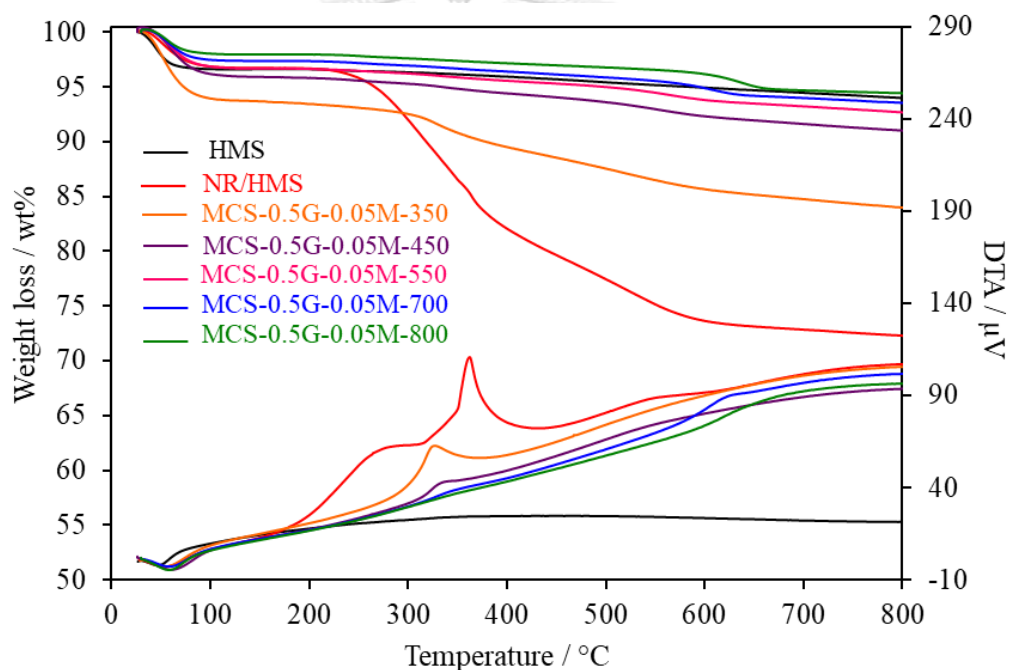


**Figure 4.1** Weight loss and DTA curves of HMS, NR/HMS, and MCS-0.5G-0.05M-*t* series prepared at different carbonization temperatures.

**Table 4.1** Carbon content of the pure silica HMS, NR/HMS precursor and MCS nanocomposites prepared under different conditions.

Material	NR Content (g)	H <sub>2</sub> SO <sub>4</sub> concentration (M)	Final temperature (°C)	Carbon content <sup>b</sup> (wt.%)
HMS	0	-	550	n.d.
NR/HMS <sup>a</sup>	0.5	0.05	-	23.9
MCS-0.5G-0.05M-350	0.5	0.05	350	9.1
MCS-0.5G-0.05M-450	0.5	0.05	450	4.2
MCS-0.5G-0.05M-550	0.5	0.05	550	3.5
MCS-0.5G-0.05M-700	0.5	0.05	700	3.4
MCS-0.5G-0.05M-800	0.5	0.05	800	3.3
MCS-0.5G-0.50M-700	0.5	0.50	700	4.3
MCS-0.5G-1.00M-700	0.5	1.00	700	10.4
MCS-0.5G-1.50M-700	0.5	1.50	700	13.1
MCS-0.5G-2.00M-700	0.5	2.00	700	16.1
MCS-1.0G-1.00M-700	1.0	1.00	700	10.2
MCS-1.5G-1.00M-700	1.5	1.00	700	10.8

n.d. = not determined.

<sup>a</sup> Extracted samples.

<sup>b</sup> Determined by thermogravimetric analysis.

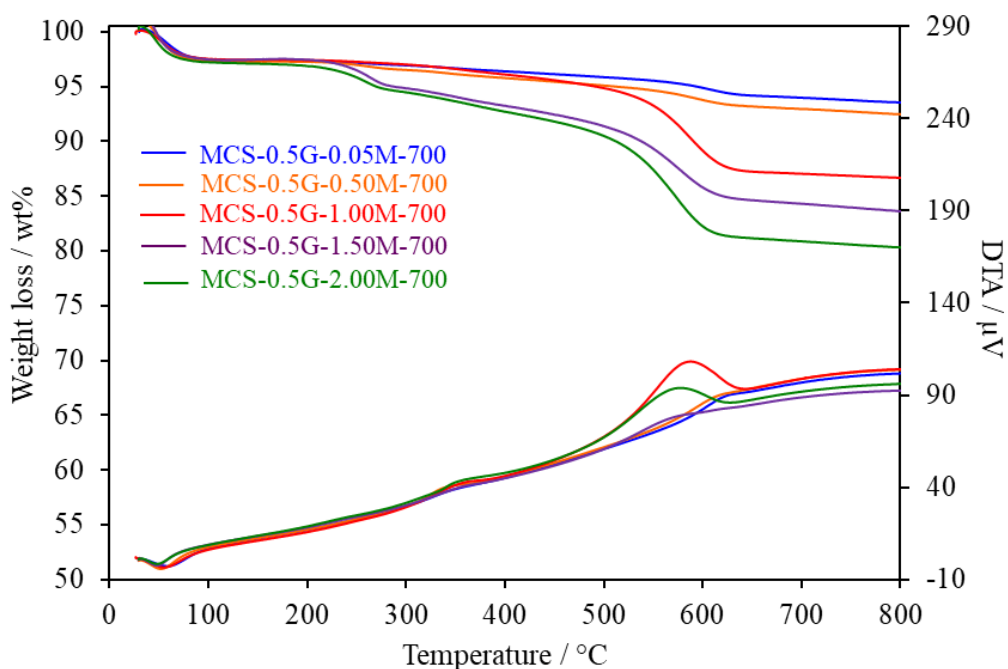


**Figure 4.2** Weight loss and DTA curves of MCS-0.5G-yM-700 series prepared at  $\text{H}_2\text{SO}_4$  concentration.

The effect of the  $\text{H}_2\text{SO}_4$  concentration on the thermal decomposition of MCS nanocomposites is revealed in Figure 4.2. The weight loss in the range of 200–450 °C and 450–650 °C was due to the decomposition of the oxygen-containing groups functionalized on the carbon surface (2–4 wt.%) and the carbon residue in the composite structure (2–12 wt.%), respectively, which systematically increased with increasing  $\text{H}_2\text{SO}_4$  concentrations (Table 4.1). The  $\text{H}_2\text{SO}_4$  enhanced the dehydration reactions and the substitution of sulfonic acid groups onto the resulting amorphous carbon at low temperatures [7]. When increasing the carbonization temperature, the oxygen-containing functional groups were decomposed to  $\text{H}_2\text{O}$ , carbon monoxide, carbon dioxide, and sulfur dioxide [7, 79]. Moreover, the  $\text{H}_2\text{SO}_4$  played an important role in generating carbonaceous residues from NR molecules due to promoting the formation of aromatic structures and cross-linking processes [7].

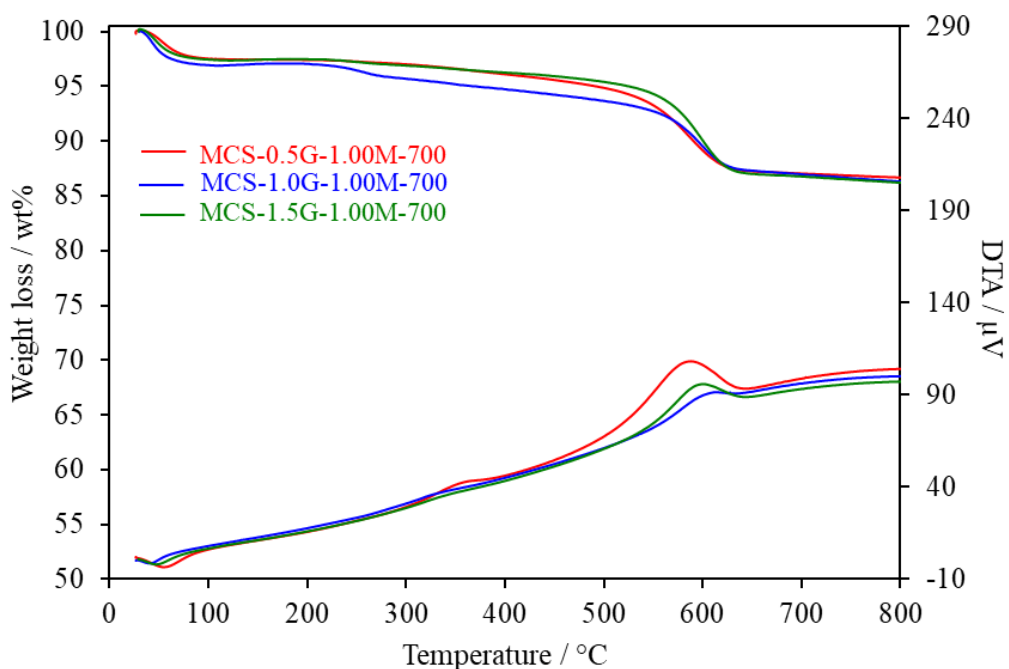


**Figure 4.3** Weight loss and DTA curves of MCS-xG-1.00M-700 series prepared at different natural rubber content in the preparation of the NR/HMS precursor.

The weight loss and differential thermal analysis (DTA) curves of HMS, NR/HMS, and MCS-xG-1.00M-700 series prepared at different natural rubber content in the preparation of the NR/HMS precursor are compared in Figure 4.3. Increasing the amount of NR used in the preparation of the NR/HMS precursor from 0.5 to 1.5 g did not influence the carbon content of the resulting MCS nanocomposites. This result was ascribed to the limited incorporation of NR molecules into the mesostructure of HMS.



## 4.2 XRD analysis

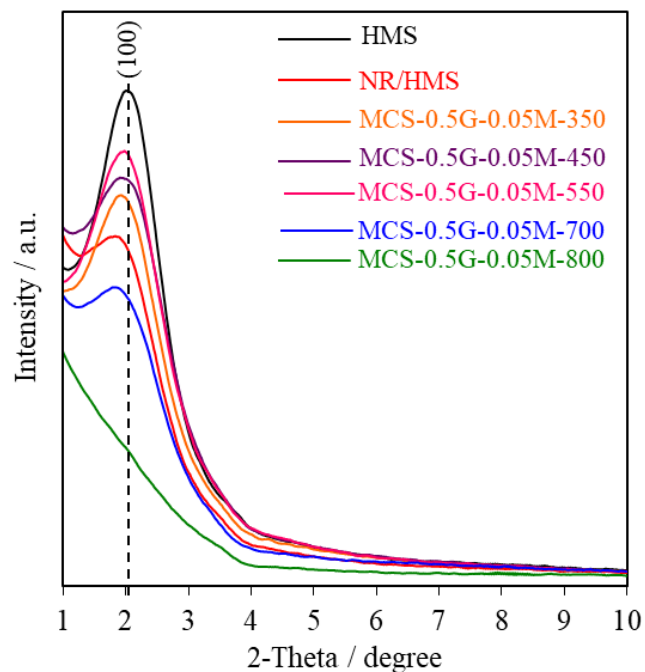


**Figure 4.4** XRD patterns of HMS, NR/HMS, and MCS-0.5G-0.05M-*t* series prepared at different carbonization temperatures.

The small-angle XRD patterns of the pure silica HMS, NR/HMS, and MCS-0.5G-0.05M-*t* series prepared at different carbonization temperatures are shown in Figure 4.4. The presence of an intense reflection at a 2-Theta in the range of 1.5–3.0°, corresponding to the (100) plane of a hexagonal mesostructure with a wormhole-like silicate framework [9], confirmed the successful preparation of HMS-based materials. The NR/HMS nanocomposite exhibited a shift of this reflection to a lower 2-Theta position, with respect to the diffraction of HMS, due to the incorporation of rubber molecules into the mesostructured silica [9, 17, 28]. As a result, the wall thickness ( $W_t$ ) of NR/HMS was larger than that of pure HMS (Table 4.2). The presence of NR in the HMS structure also hampered the hexagonal ordering of the mesoporous structure and the condensation of silicate species during the formation of the mesostructured silica framework [9, 17, 28].

**Table 4.2** Structural properties of the pure silica HMS, NR/HMS precursor and MCS nanocomposites prepared under different conditions.

Material	NR Content (g)	H <sub>2</sub> SO <sub>4</sub> concentration (M)	Final temperature (°C)	$d_{100}^a$ (nm)	$a_0^b$ (nm)	$W_t^c$ (nm)
HMS	0	-	550	4.80	5.55	2.61
NR/HMS <sup>a</sup>	0.5	0.05	-	5.08	5.87	3.52
MCS-0.5G-0.05M-350	0.5	0.05	350	4.80	5.55	3.13
MCS-0.5G-0.05M-450	0.5	0.05	450	4.75	5.49	3.05
MCS-0.5G-0.05M-550	0.5	0.05	550	4.70	5.43	2.96
MCS-0.5G-0.05M-700	0.5	0.05	700	4.91	5.67	3.27
MCS-0.5G-0.05M-800	0.5	0.05	800	n.d.	n.d.	n.d.
MCS-0.5G-0.50M-700	0.5	0.50	700	4.91	5.67	3.30
MCS-0.5G-1.00M-700	0.5	1.00	700	4.97	5.73	3.36
MCS-0.5G-1.50M-700	0.5	1.50	700	5.02	5.80	3.56
MCS-0.5G-2.00M-700	0.5	2.00	700	5.08	5.87	3.75
MCS-1.0G-1.00M-700	1.0	1.00	700	4.97	5.73	3.49
MCS-1.5G-1.00M-700	1.5	1.00	700	4.97	5.73	3.41

n.d. = not determined.

<sup>a</sup> Extracted samples.

<sup>b</sup> Interplanar spacing of (100) plane ( $d_{100}$ ) obtained from XRD analysis.

<sup>c</sup> The repeat distance ( $a_0$ ) between the pore centers of the hexagonal structure was calculated from  $a_0 = 2d_{100}/3^{1/2}$ .

<sup>d</sup> The framework wall thickness was determined by subtracting the BJH mesopore size from the repeat distance between pore centers.

The carbonization temperature strongly influenced the hexagonal mesostructure of the resulting MCS nanocomposites. Increasing the carbonization temperature up to 550 °C increased the intensity of the (001) reflection. As evidenced from the TGA, this was due to the decomposition of long-chain rubber at temperatures above 270 °C (see also Figure 4.1). Moreover, an increased temperature promoted the condensation of incompletely hydrolyzed silicate species to form siloxane bonds [81]. These effects led to a contraction of the hexagonal unit cell ( $a_0$ ) due to the reduced wall thickness of the MCS nanocomposites (Table 4.2). However, a loss of mesostructure ordering was observed when the carbonization step was performed above 600 °C. This was due to dehydroxylation of the silicate

networks, which was enhanced at  $> 500$  °C [82, 83]. Interestingly, the  $a_0$  and  $W_t$  of MCS composites obtained at 600 and 700 °C were larger than that of HMS calcined at 700 °C (Table 4.2). This suggests that the formed carbon layer acted as a rigid support in the wall and probably limited the structural shrinkage. This result was similar to that reported by Liu et al. [36], who observed an interpenetrating network of carbon-silica nanocomposites prepared from a soluble resol polymer as the carbon source, TEOS as the silica source, and triblock copolymer F127 as the template via evaporation-induced triconstituent co-assembly. The carbon layer acted as a rigid support and so decreased the framework shrinkage. Unfortunately, the mesostructured framework of MCS-0.5G-0.05M-800 collapsed, which could be explained by the small carbon content containing in the silica wall that was insufficient to retain the mesostructured framework during the severe dehydroxylation that occurred at this high temperature (700 °C).

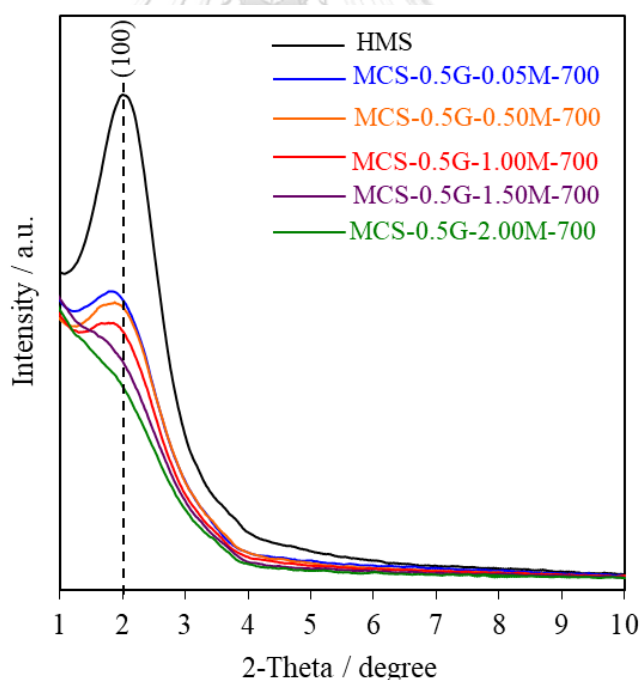


**Figure 4.5** XRD patterns of MCS-0.5G-yM-700 series prepared at  $H_2SO_4$  concentration.

The MCS series pretreated with different  $H_2SO_4$  concentrations exhibited the characteristic peaks at lower 2-Theta positions than the pure silica HMS (Figure 4.5). As shown in Table 4.2, the  $a_0$  and  $W_t$  values of the MCS nanocomposites expanded

with increasing  $\text{H}_2\text{SO}_4$  concentrations, which was in accord with an increased amount of carbon residue incorporated into the mesostructured silica framework. In addition, the concentration of  $\text{H}_2\text{SO}_4$  used in the pretreatment step detrimentally affected the structural order of the resulting nanocomposites. This was due to either a lower diffraction contrast or a loss of mesostructured order at a high content of incorporated carbon residue.

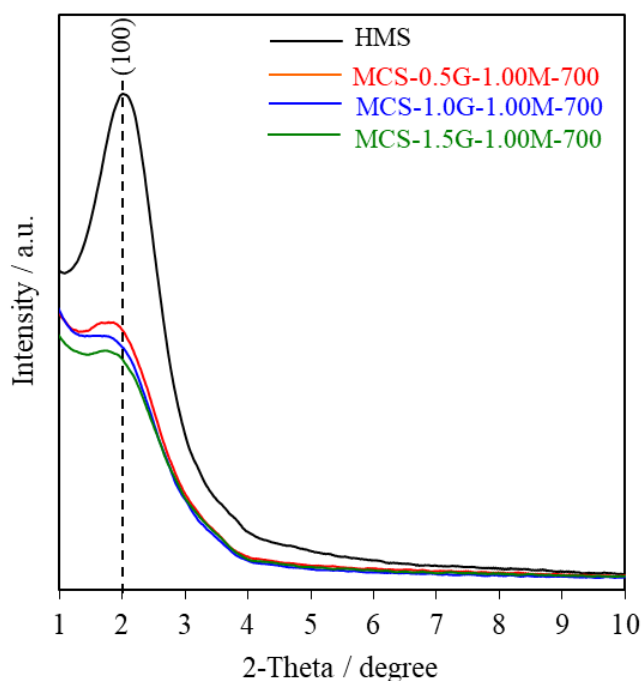


**Figure 4.6** XRD patterns of MCS-xG-1.00M-700 series prepared at different natural rubber content in the preparation of the NR/HMS precursor.

As shown in Figure 4.6, an increased amount of NR (from 0.5 to 1.5 g) used in the preparation of the NR/HMS precursors hampered the structural order of the resulting MCS nanocomposites. Indeed, their structural properties were essentially determined by the mesostructure of NR/HMS precursors themselves. Nevertheless, their  $a_0$  value was not significantly altered since the carbon content of these materials was nearly the same (Table 4.2). Thus, using NR/HMS with a higher NR content as a precursor gave a higher fraction of carbon phase that was not incorporated into the mesostructured silica.

### 4.3 N<sub>2</sub> physisorption measurement

The N<sub>2</sub> adsorption-desorption isotherms revealed that both the pure silica HMS and the NR/HMS precursor exhibited type IV sorption isotherms (Figure 4.7A), according to the IUPAC classification, with the hysteresis loops at  $P/P_0$  ranging from 0.2–0.4, characteristic of framework confined mesoporous materials. However, the NR/HMS exhibited a lower N<sub>2</sub> adsorbed volume,  $S_{\text{BET}}$ ,  $D_p$ , and  $V_t$  than HMS (Table 4.3). This suggests that a part of the NR molecules might cover the pore mouths or occupy the porous channels of the mesostructured silica. Except for MCS-0.5G-0.05M-800, all MCS samples showed a type IV isotherm (Figure 4.7A-C). When compared to the NR/HMS precursors, the MCS nanocomposites obtained at 350–600 °C showed enhanced textural properties (Table 4.3). The carbonization not only decomposed the NR covering the precursor surface but also enhanced the condensation of the silicate framework. The mesostructure collapse was the main reason for the severe loss of mesoporosity at the carbonization temperature of 800 °C. These results are in accord with the structural properties as analyzed by XRD (see also Figure 4.4).

With respect to the effect of the H<sub>2</sub>SO<sub>4</sub> concentration used in the pretreatment step, the MCS nanocomposites prepared with a higher acid concentration exhibited a lower  $S_{\text{BET}}$ ,  $D_p$ , and  $V_t$  than those obtained with a lower concentration of H<sub>2</sub>SO<sub>4</sub> (Table 4.3). This correlated well with the trend in the carbon content of this MCS series. The increased H<sub>2</sub>SO<sub>4</sub> concentration promoted the formation of a carbon residue, some of which might occupy the mesopores of the resulting nanocomposites. Increasing the amount of NR used in the preparation of the NR/HMS precursors reduced the textural properties of the MCS materials (Table 4.3). Combining this result with the XRD analysis confirmed that the MCS prepared with a high NR content had a higher carbon phase fraction occluding into the mesopores than the MCS prepared from the NR/HMS precursor with a high NR dispersion.

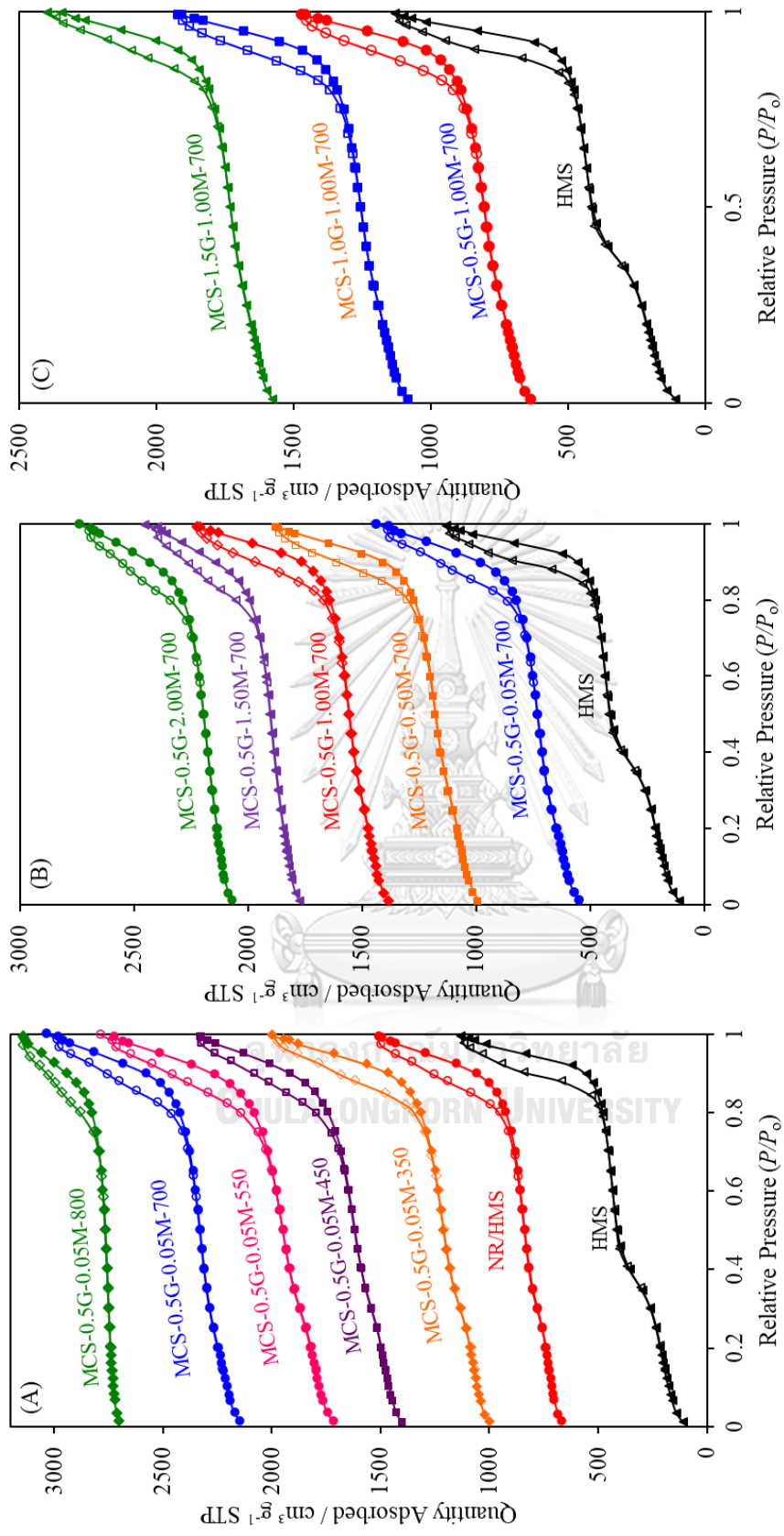


**Figure 4.7**  $N_2$  adsorption-desorption isotherms of pure silica HMS, NR/HMS precursor, and MCS nanocomposites prepared under different conditions.

**Table 4.3** Textural properties of the pure silica HMS, NR/HMS precursor and MCS nanocomposites prepared under different conditions.

Material	NR Content (g)	H <sub>2</sub> SO <sub>4</sub> concentration (M)	Final temperature (°C)	S <sub>BET</sub> <sup>b</sup> (m <sup>2</sup> g <sup>-1</sup> )	S <sub>ext</sub> <sup>c</sup> (m <sup>2</sup> g <sup>-1</sup> )	D <sub>p</sub> <sup>d</sup> (nm)	V <sub>t</sub> <sup>e</sup> (cm <sup>3</sup> g <sup>-1</sup> )	V <sub>p</sub> <sup>f</sup> (cm <sup>3</sup> g <sup>-1</sup> )
HMS	0	-	550	815	216	2.94	1.80	0.50
NR/HMS <sup>a</sup>	0.5	0.05	-	589	323	2.35	1.40	0.16
MCS-0.5G-0.05M-350	0.5	0.05	350	737	399	2.42	1.70	0.23
MCS-0.5G-0.05M-450	0.5	0.05	450	766	450	2.44	1.73	0.24
MCS-0.5G-0.05M-550	0.5	0.05	550	831	485	2.47	1.83	0.25
MCS-0.5G-0.05M-700	0.5	0.05	700	675	387	2.40	1.44	0.15
MCS-0.5G-0.05M-800	0.5	0.05	800	338	184	1.80	0.93	0.07
MCS-0.5G-0.50M-700	0.5	0.50	700	670	342	2.37	1.42	0.21
MCS-0.5G-1.00M-700	0.5	1.00	700	664	322	2.37	1.41	0.19
MCS-0.5G-1.50M-700	0.5	1.50	700	524	312	2.24	1.18	0.11
MCS-0.5G-2.00M-700	0.5	2.00	700	500	316	2.12	1.14	0.10
MCS-1.0G-1.00M-700	1.0	1.00	700	631	311	2.24	1.35	0.17
MCS-1.5G-1.00M-700	1.5	1.00	700	602	287	2.22	1.30	0.17

<sup>a</sup> Extracted samples.<sup>b</sup> BET surface area.<sup>c</sup> External surface area determined from *t*-plot curves.<sup>d</sup> Pore diameter calculated using the BJH method.<sup>e</sup> Total pore volume.<sup>f</sup> Mesopore volume

#### 4.4 FTIR spectroscopy

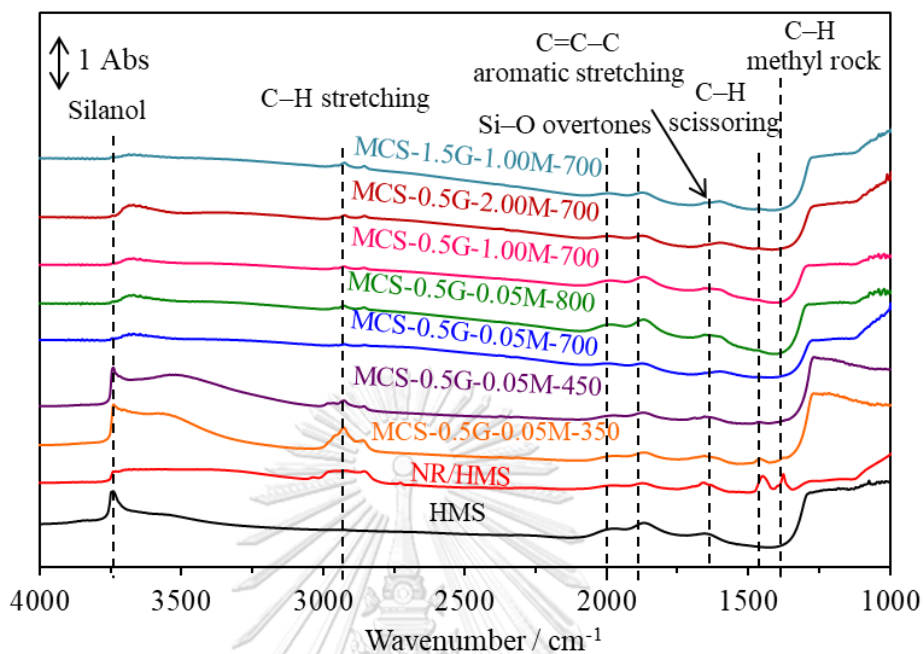


**Figure 4.8** FTIR spectra of pure silica HMS, NR/HMS precursor, and MCS nanocomposites prepared under different conditions.

The FTIR analysis was used to confirm the presence of rubber or carbon residue in the mesostructured nanocomposites. In addition, it is a facile technique to follow changes in the organo-functional groups upon increasing the carbonization temperature. As shown in Fig. 4.8, the pure silica HMS exhibited a band at  $1,634\text{ cm}^{-1}$  due to the vibration of the physically absorbed water, while those at  $1,875$  and  $2,100\text{ cm}^{-1}$  represented the Si—O overtone of the silica framework [84]. The intense band at  $3,750\text{ cm}^{-1}$  was assigned to the free silanol groups (Si—OH) [84]. The NR/HMS precursor showed additional bands related to the C—H stretching ( $2,800$ – $3,000\text{ cm}^{-1}$ ) and C—H deformation vibrations ( $1,370$  and  $1,430\text{ cm}^{-1}$ ), as the characteristics of the molecular rubber structure [9]. The presence of rubber in the NR/HMS decreased the intensity of the free silanol band ( $3,750\text{ cm}^{-1}$ ), since the hydrolysis and condensation of TEOS were hampered, and so some remnant ethoxy groups remained in the silicate framework [9, 28].



The carbonization at 350–550 °C restored the silanol groups, while the characteristic bands of NR were gradually decreased with increasing temperature. The result confirmed the conversion of the NR phase into carbon residue concomitantly with an enhanced condensation of the silicate structure during the carbonization process, as indicated by the TGA and XRD analyses (see also Figure. 4.1 and 4.4). However, the free silanol band almost disappeared above 700 °C due to the severe dehydroxylation of silanol groups. Trace C–H stretching and bending signals (2800–3000 cm<sup>-1</sup> and 1460 cm<sup>-1</sup>, respectively) were found at these high carbonization temperatures, suggesting that some rubber molecules were difficult to transform into the carbonaceous phase. A similar observation was found for the MCS series prepared with increasing H<sub>2</sub>SO<sub>4</sub> concentrations and NR contents. The silica phase covering the trapped rubber molecules might hinder the carbon formation. In addition, the band at 1,580–1,615 cm<sup>-1</sup>, corresponding to C=C–C aromatic stretching [85], was strongly correlated with the carbon residue content in the MCS nanocomposites prepared under the different conditions.

#### 4.5 Raman spectroscopy

Raman spectroscopy is a powerful technique to acquire information about the structural aspect of carbonaceous materials [86-90]. Herein, the Raman technique was used to investigate the transformation of entrapped rubber molecules to carbon in the MCS materials synthesized under different conditions. No Raman scattering band was observed for the pure silica HMS, while the NR/HMS precursor exhibited a broad band in range of 1,090–1,780 cm<sup>-1</sup> (Fig. 4.9) and at a high Raman shift region around 2,850 cm<sup>-1</sup> (Figure 4.10), which was attributed to the polymeric backbone of rubber incorporated into the HMS structure [86].

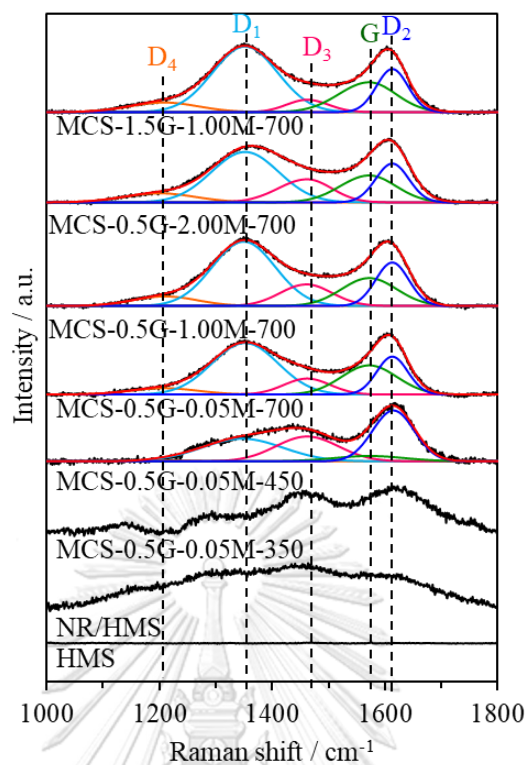


**Figure 4.9** Raman spectra of pure silica HMS, NR/HMS precursor, and MCS nanocomposites prepared under different conditions at low Raman shift region.

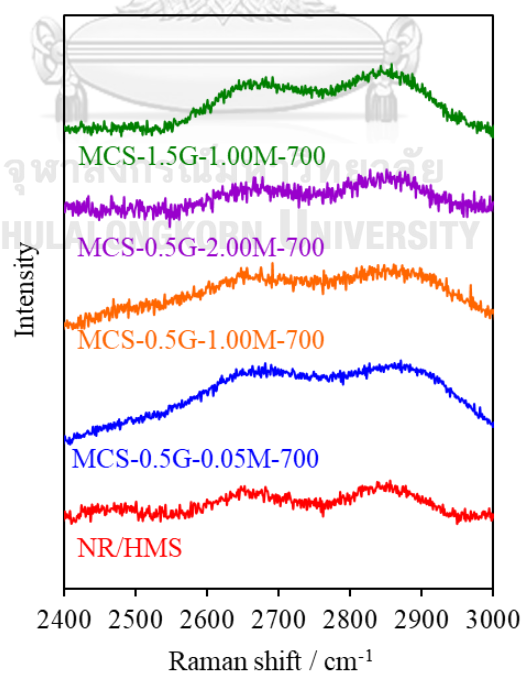


**Figure 4.10** Raman spectra of NR/HMS precursor, and MCS nanocomposites prepared under different conditions at high Raman shift region.

At a carbonization temperature of 350 °C, the residual rubber moieties still existed although the majority of NR was converted into carbonaceous species (MCS-0.5G-0.05M-350). A weak band at around 1,150  $\text{cm}^{-1}$  was attributed to the O=S=O symmetric stretching vibration of the sulfonic acid group grafted on the carbon surface. Increasing the temperature matured the carbon residue structure, as deduced from the increased band intensity. The resulting MCS nanocomposites exhibited two well-developed bands at around 1,370 (D band) and 1,590 (G band)  $\text{cm}^{-1}$ , which revealed the disorder or defect in the organization of carbon atoms and the  $\text{sp}^2$  in-plane vibration of the carbon atoms, respectively, [38]. The D and G bands were deconvoluted into five components, which were assigned to polyenes ( $\text{D}_4$ ; 1,208  $\text{cm}^{-1}$ ), graphene edges ( $\text{D}_1$ ; 1,352  $\text{cm}^{-1}$ ), amorphous carbon ( $\text{D}_3$ ; 1,462  $\text{cm}^{-1}$ ), graphitic carbon (G; 1,572  $\text{cm}^{-1}$ ), and graphene sheets ( $\text{D}_2$ ; 1,610  $\text{cm}^{-1}$ ), respectively, [30, 90]. Moreover, the intensity of the O=S=O band disappeared at a carbonization temperature of 700 °C, which supported the rearrangement of the amorphous carbon residue to a graphitic carbon structure [7].

**Table 4.4** Raman spectroscopy results of the pure silica HMS, NR/HMS precursor, and MCS nanocomposites.

Sample	Relative area (%)					$I_{\text{D}_1}/(I_{\text{D}_1}+I_{\text{G}}+I_{\text{D}_2})$
	$\text{D}_4$	$\text{D}_1$	$\text{D}_3$	G	$\text{D}_2$	
HMS	-	-	-	-	-	-
NR/HMS	-	-	-	-	-	-
MCS-0.5G-0.05M	5.86	46.27	10.05	21.88	15.93	0.55
MCS-0.5G-0.50M	6.30	43.58	12.04	21.58	16.51	0.53
MCS-0.5G-1.00M	7.08	43.66	12.43	20.90	15.92	0.54
MCS-0.5G-1.50M	7.16	43.93	13.66	20.50	14.75	0.55
MCS-0.5G-2.00M	7.25	40.75	16.32	18.68	16.99	0.53
MCS-1.0G-1.00M	7.87	44.96	9.26	22.79	15.12	0.54
MCS-1.5G-1.00M	8.18	48.23	7.46	24.96	11.17	0.57

The degree of graphitization of the carbon phase [ $I_{D1}/(I_G + I_{D1} + I_{D2})$ ] contained in the MCS nanocomposites was calculated from the integral intensity of the three bands at  $1,352\text{ cm}^{-1}$  ( $D_1$ ),  $1,610\text{ cm}^{-1}$  ( $D_2$ ), and  $1,572\text{ cm}^{-1}$  ( $G$ ). The  $I_{D1}/(I_G + I_{D1} + I_{D2})$  values for the MCS composites ranged from 0.53–0.57 (Table 4.4), indicating a similarity in their carbon structure. The relatively large fraction of  $D_1$  (40.75–48.23%) suggested that the carbon residue was present as highly dispersed nanosized graphene in the mesostructured nanocomposites. In the high Raman shift region, two bands, at  $2,650\text{ cm}^{-1}$  ( $D'_1$  band) and  $2,850\text{ cm}^{-1}$  ( $D'_3$  band), were observed (Figure 4.10), and were attributed to the overtone of D or  $D_1$  and a combination of D and G, respectively, [90]. These bands were related to the second order scattering of imperfect graphite and disordered carbons as graphene oxide-like carbon species [91].

Increasing the  $\text{H}_2\text{SO}_4$  concentration from 0.05 M to 2.00 M increased the fraction of amorphous carbon ( $D_3$ ), whereas the formation of crystalline carbon (G) was decreased from 21.9% (MCS-0.5G-0.05M-700) to 18.7% (MCS-0.5G-2.00M-700). Using a high  $\text{H}_2\text{SO}_4$  concentration might result in a high degree of sulfonic acid groups being grafted onto the carbon residue [7], which could retard the rearrangement of amorphous carbon to graphitic carbon. On the other hand, increasing the amount of NR used in the synthesis of NR/HMS precursor from 0.5 to 1.5 g was beneficial for the graphitization, since an increased fraction of graphitic carbon, but a lowered carbon amorphousity, was observed. The higher amount of NR used as a carbon source increased the carbon residue content, and so the structural ordering, resulting in a greater graphitized carbon phase in the resulting MCS nanocomposites.

#### 4.6 XPS analysis

The MCS nanocomposites were characterized by XPS in comparison with the pristine NR/HMS, and the BEs obtained were interpreted to clarify the effects of the  $\text{H}_2\text{SO}_4$  concentration and NR amount on the surface functionalities and structure of carbon dispersed in the resulting MCS materials. As shown in Figure 4.8A, the C1s XPS signals of the NR/HMS precursor represented the C=C bond ( $282.9\text{ eV}$ ) and the C–C/C–H bonds ( $284.8\text{ eV}$ ), which corresponded to the *cis* 1,4–polyisoprene

backbone of NR [28]. The signals at 285.8 eV and 287.2 eV were assigned to the C—O/C—O—C bonds and the C=O bond, respectively, [92] of the surface functional groups formed by the oxidative cleavage of NR chains during storage [93]. For the MCS nanocomposites synthesized under different conditions (Figure 6B–D), the main C1s XPS signal was shifted to lower BEs (283.6–284.5 eV).

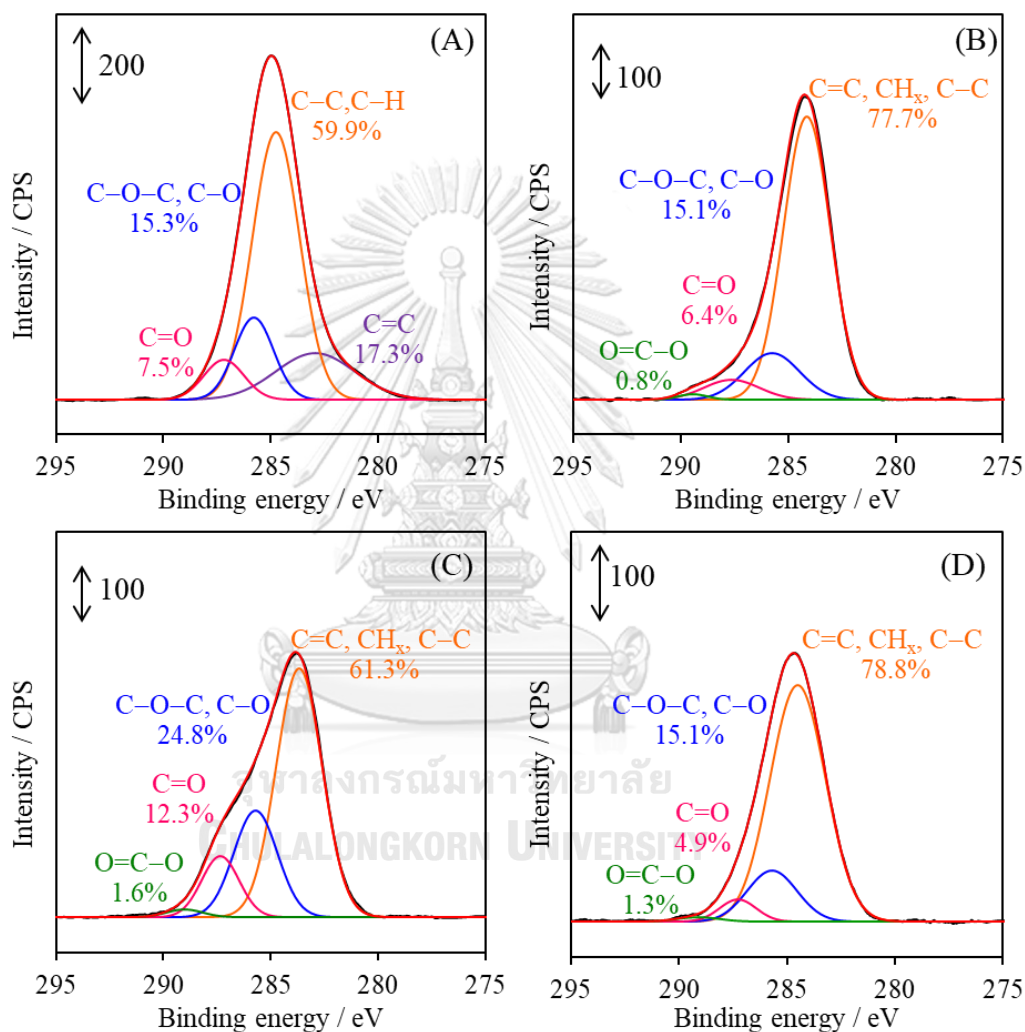


**Figure 4.11** C1s XPS spectra of (A) NR/HMS, (B) MCS-0.5G-1.00M-700, (C) MCS-0.5G-2.00M-700, and (D) MCS-1.5G-1.00M-700.

The spectra were further deconvoluted into four components, representing carbon groups (C=C, CH<sub>x</sub>, and C—C) at 283.6–284.5 eV, hydroxyl groups or ether linkages (C—O, C—O—C) at 285.3–285.7 eV, carbonyl groups (C=O) at 287.2–287.3 eV, and carboxyl or ester groups (COO) at 289.0–289.1 eV. In addition, the O1s XPS

spectra confirmed the presence of these oxygenated groups, as shown in Figure 4.12. The band corresponding to the carboxyl or ester groups was observed at 530.2–530.5 eV, while that found at 531.5–532.0 eV was attributed to the hydroxyl or ether groups [94, 95].

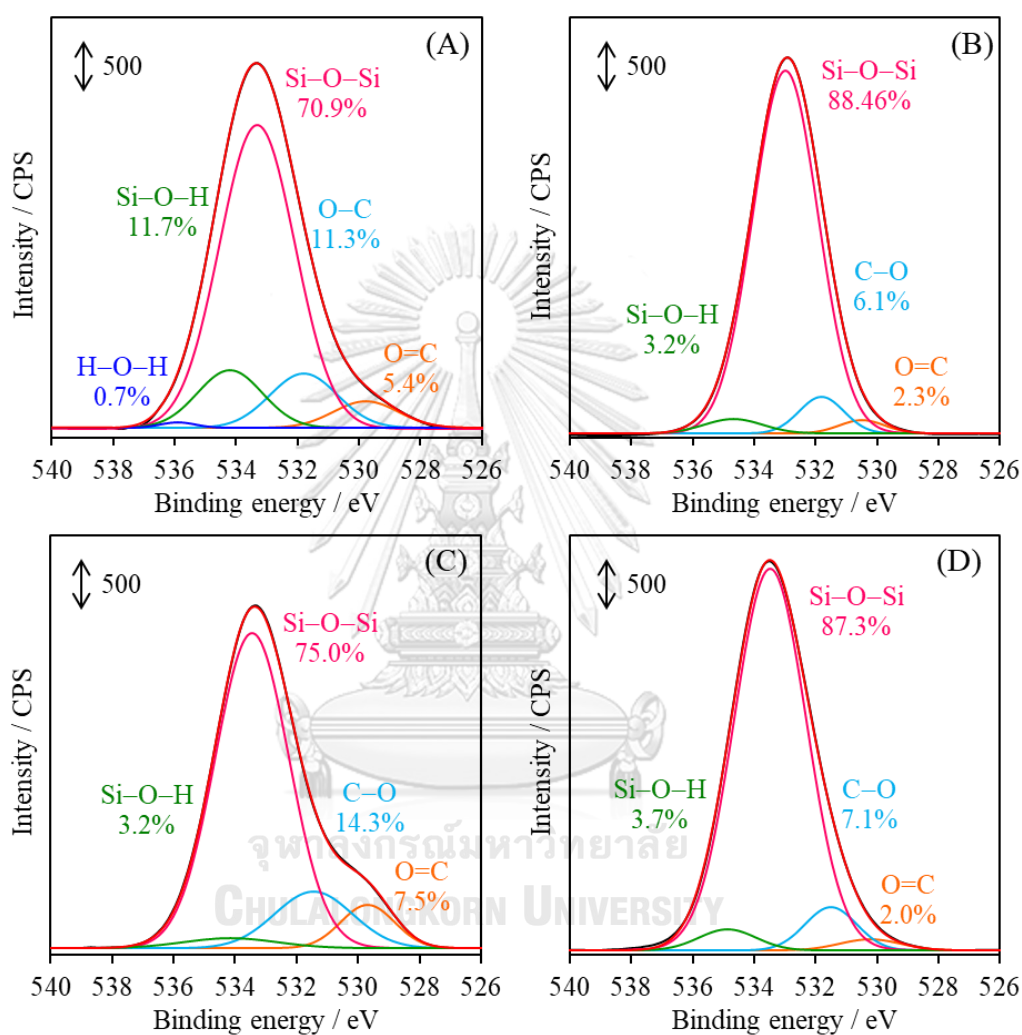


**Figure 4.12** O1s XPS spectra of (A) NR/HMS, (B) MCS-0.5G-1.00M-700, (C) MCS-0.5G-2.00M-700, and (D) MCS-1.5G-1.00M-700.

The chemical composition (atomic concentration) obtained from the XPS analysis is summarized in Table 4.5. A high concentration of oxygen-functional groups on the material surface confirmed that the carbon derived from the *in situ* formed NR/silica precursor possessed a graphene oxide-like structure. Increasing the  $\text{H}_2\text{SO}_4$  concentration from 1.00 to 2.00 M enhanced the content of oxygen-containing

groups on the carbon surface due to the oxidation of the carbonaceous residue by  $\text{H}_2\text{SO}_4$ . A similar observation was previously reported in the sulfonation of biochar using concentrated  $\text{H}_2\text{SO}_4$  solution, which not only introduced sulfonic acid groups but also generated carboxyl and hydroxyl groups on the resulting acidic carbon [96-98]. When compared to MCS-0.5G-1.00M-700, the content of carbon groups ( $\text{C}=\text{C}$ ,  $\text{CH}_x$ , and  $\text{C}-\text{C}$ ) was increased, while that of  $\text{C}=\text{O}$  and  $\text{C}-\text{O}$  was reduced, on MCS-1.5G-1.00M-700. Increasing the amount of NR in the nanocomposite precursor promoted the formation of a carbon residue and condensed carbon phase. Overall, these results were in good agreement with the effects of the  $\text{H}_2\text{SO}_4$  concentration and NR content on the structural aspect of carbon species, as evidenced by the Raman analysis (Section 4.5).

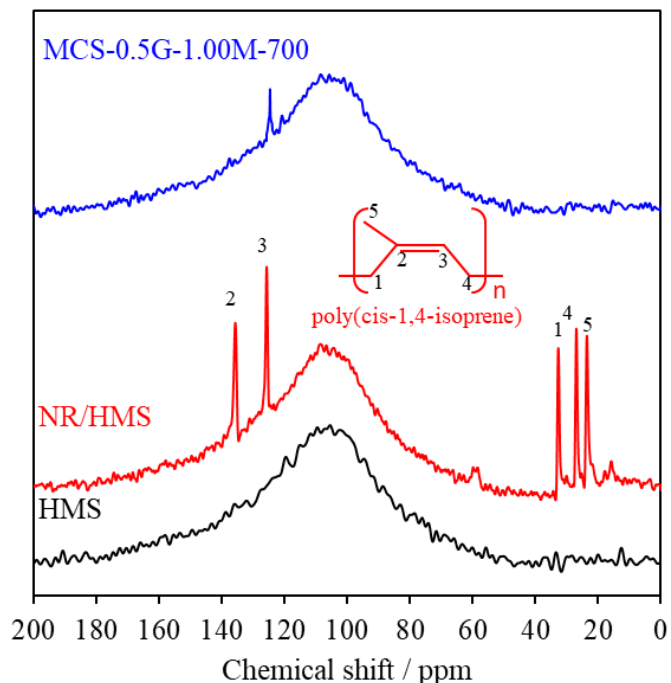


**Table 4.5** XPS results of the pure silica HMS, NR/HMS precursor, and MCS nanocomposites

Atomic orbital	Bond type	HMS		NR/HMS		MCS-0.5G-1.00M-700		MCS-0.5G-2.00M-700		MCS-1.5G-1.00M-700	
		BE (eV)	Conc. <sup>a</sup> (%)	BE (eV)	Conc. <sup>a</sup> (%)	BE (eV)	Conc. <sup>a</sup> (%)	BE (eV)	Conc. <sup>a</sup> (%)	BE (eV)	Conc. <sup>a</sup> (%)
C1s	C=C	-	-	282.9	3.25	-	-	-	-	-	-
	C-C/ C-H	285.5	3.23	284.8	11.25	283.6	6.51	283.7	7.80	284.5	6.97
	C-O/ C-O-C	286.7	0.91	285.8	2.88	285.3	1.26	285.7	3.15	285.7	1.33
	C=O	-	-	287.2	1.41	287.2	0.54	287.3	1.57	287.3	0.43
	O=C-O	-	-	-	-	289.0	0.07	289.0	0.20	289.1	0.11
Si2p	Si-O	104.5	15.13	104.4	12.26	104.1	14.04	104.0	14.22	104.0	13.62
	O=C	-	-	529.8	3.74	530.3	1.75	530.5	5.50	530.2	1.57
O1s	O-C	531.4	6.46	531.8	7.82	531.7	4.74	532.0	10.44	531.5	5.47
	Si-O-Si	536.4	51.35	533.3	48.85	533.0	68.63	534.4	54.80	533.5	67.65
	Si-O-H	537.5	22.93	534.2	8.08	534.7	2.47	535.7	2.34	535.9	2.84
	O-H <sup>b</sup>	-	-	535.9	0.46	-	-	-	-	-	-

<sup>a</sup> Atomic concentration. <sup>b</sup> As water.



4.7 Solid state  $^{29}\text{Si}$  MAS NMR and  $^{13}\text{C}$  CP/MAS NMR studies

**Figure 4.13** Solid-state  $^{13}\text{C}$  CP/MAS NMR spectra of HMS, NR/HMS, and MCS-0.5G-1.00M-700.

The  $^{13}\text{C}$  CP/MAS NMR spectrum (Figure 4.13) of the NR/HMS exhibited chemical shifts at 23, 27, 33, 127, and 136 ppm, which were attributed to  $-\text{CH}_3$ ,  $-\text{CH}_2-$ ,  $-\text{CH}_2-$ ,  $=\text{CH}-$ , and  $>\text{C}=\text{}$ , respectively. These results corresponded to the individual carbons of poly(*cis*-1,4-isoprene) in the NR structure [99-101]. The weak signal at  $\sim 64$  ppm was related to the O-C bonds, revealing the presence of remnant ethoxy groups in the NR/HMS due to the incomplete hydrolysis of TEOS [28, 36]. For MCS-0.5G-1.00M-700, the peak for aliphatic carbon disappeared concomitantly with the appearance of a new signal at 128 ppm, corresponding to aromatic carbon species [30]. The result indicates the decomposition and transformation of rubber to aromatic carbon during carbonization at  $700^\circ\text{C}$ , in agreement with the TGA and FTIR analyses. Previously, Zhong et al. observed a similar NMR spectrum for aromatic carbon materials prepared from sucrose, followed by carbonization at  $800^\circ\text{C}$  [102].

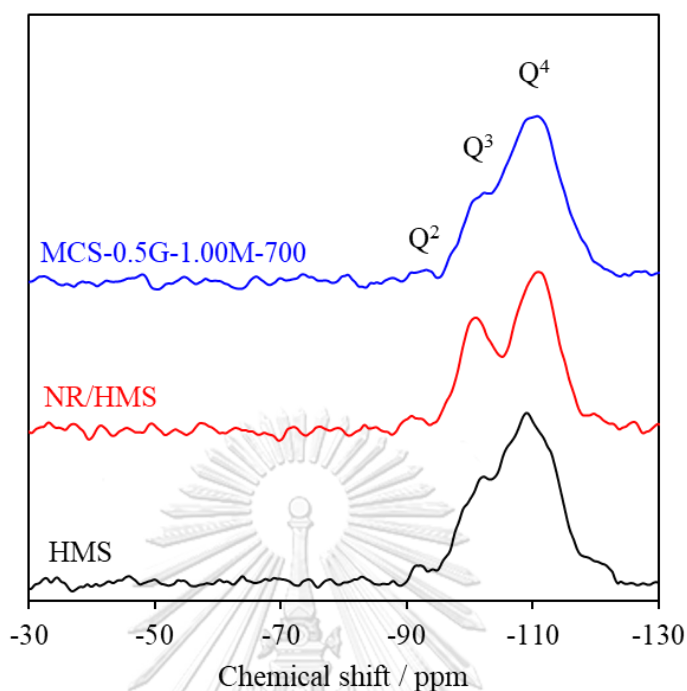


**Figure 4.14** Solid-state  $^{29}\text{Si}$ -MAS NMR spectra of HMS, NR/HMS, and MCS-0.5G-1.00M-700.

As shown in Figure 4.14, the  $^{29}\text{Si}$ -MAS NMR spectra showed the presence of  $Q^2$  (-92 ppm),  $Q^3$  (-101 ppm), and  $Q^4$  (-110 ppm) resonances, corresponding to the  $\text{Si}(\text{OSi})_2(\text{OH})_2$ ,  $\text{Si}(\text{OSi})_3(\text{OH})$ , and  $\text{Si}(\text{OSi})_4$  species, respectively. By comparing the intensities of  $Q^n$  groups of these materials in Table 4.6, The isolated silanol sites ( $Q^3$ ) of NR/HMS were higher than those of HMS because the self-assembly of surfactant micelles and the silica precursors was disturbed by the presence of rubber molecules in the synthesis mixture, resulting in lowered the degree of silicate condensation [28]. Comparison of the intensities of the  $Q^n$  groups of the composites revealed that MCS-0.5G-1.00M-700 exhibited a lower  $Q^2$  and  $Q^3$  but a higher four siloxane-bonded site ( $Q^4$ ) than the NR/HMS precursor. This result indicated that the carbonization process enhanced the condensation degree of silicate framework in the resulting nanocomposite.

**Table 4.6** Relative intensity of the  $Q^n$  group

Sample	$Q^2$ (%)	$Q^3$ (%)	$Q^4$ (%)
HMS	2.4	18.1	79.5
NR/HMS	3.0	32.7	64.3
MCS-0.5G-1.00M-700	2.3	14.7	83.0

#### 4.8 Field-emission scanning electron microscopy (FE-SEM)

The morphology of the pure silica HMS, NR/HMS, and MCS nanocomposites was investigated by FE-SEM, with representative images shown in Figure 4.15. The HMS exhibited small particles (23–68 nm) that were uniformly aggregated, generating interparticle voids with an average size of 22–57 nm (Figure 4.15A). This result was in good agreement with the  $N_2$  physisorption isotherm, consisting of a large hysteresis loop at  $P/P_0 \approx 0.75$  (Fig. 3). For NR/HMS (Figure 4.15B), the presence of the rubber phase induced the formation of particle agglomerates (102–167 nm) since some rubber molecules inevitably deposited on the external surface of NR/HMS. Nevertheless, the uniform morphology of the NR/HMS particles suggested that the rubber phase was homogeneously dispersed throughout the nanocomposite.

After carbonization, the resulting MCS materials possessed a reduced particle size and less aggregation, such as MCS-0.5G-1.00M-700 with an average size of 21–43 nm (Figure 4.15C), due to the decomposition and transformation of the rubber phase into carbon residue. When the  $H_2SO_4$  concentration was increased to 2.00 M, the particle size of MCS was enlarged to 30–47 nm (Figure 4.15D), which corresponded to an increased wall thickness of the silica wall and a high content of incorporated carbon, as evidenced from the XRD and TGA analyses, respectively.

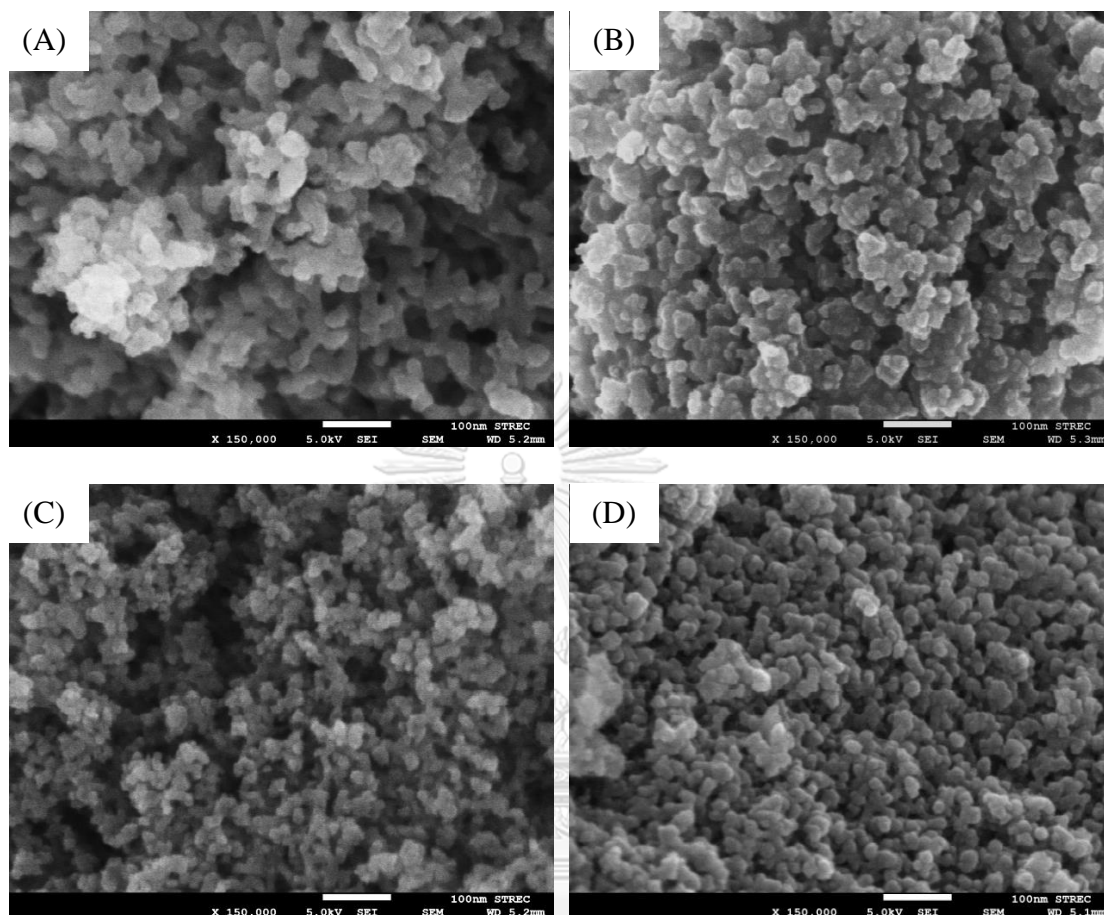


**Figure 4.15** FE-SEM images of (A) HMS, (B) NR/HMS, (C) MCS-0.5G-1.00M-700, and (D) MCS-0.5G-2.00M-700, all at a magnification of 150000 $\times$ .

#### 4.9 Transmission electron microscopy (TEM)

Representative TEM images of the pure silica HMS and nanocomposites are shown in Fig. 4.16. All the samples possessed conventional uniform wormhole-like mesopores, as observed for the HMS materials [17, 28]. This observation was in accord with the XRD and N<sub>2</sub> physisorption results, which confirmed that the mesostructure of the MCS nanocomposites was maintained after carbonization process.

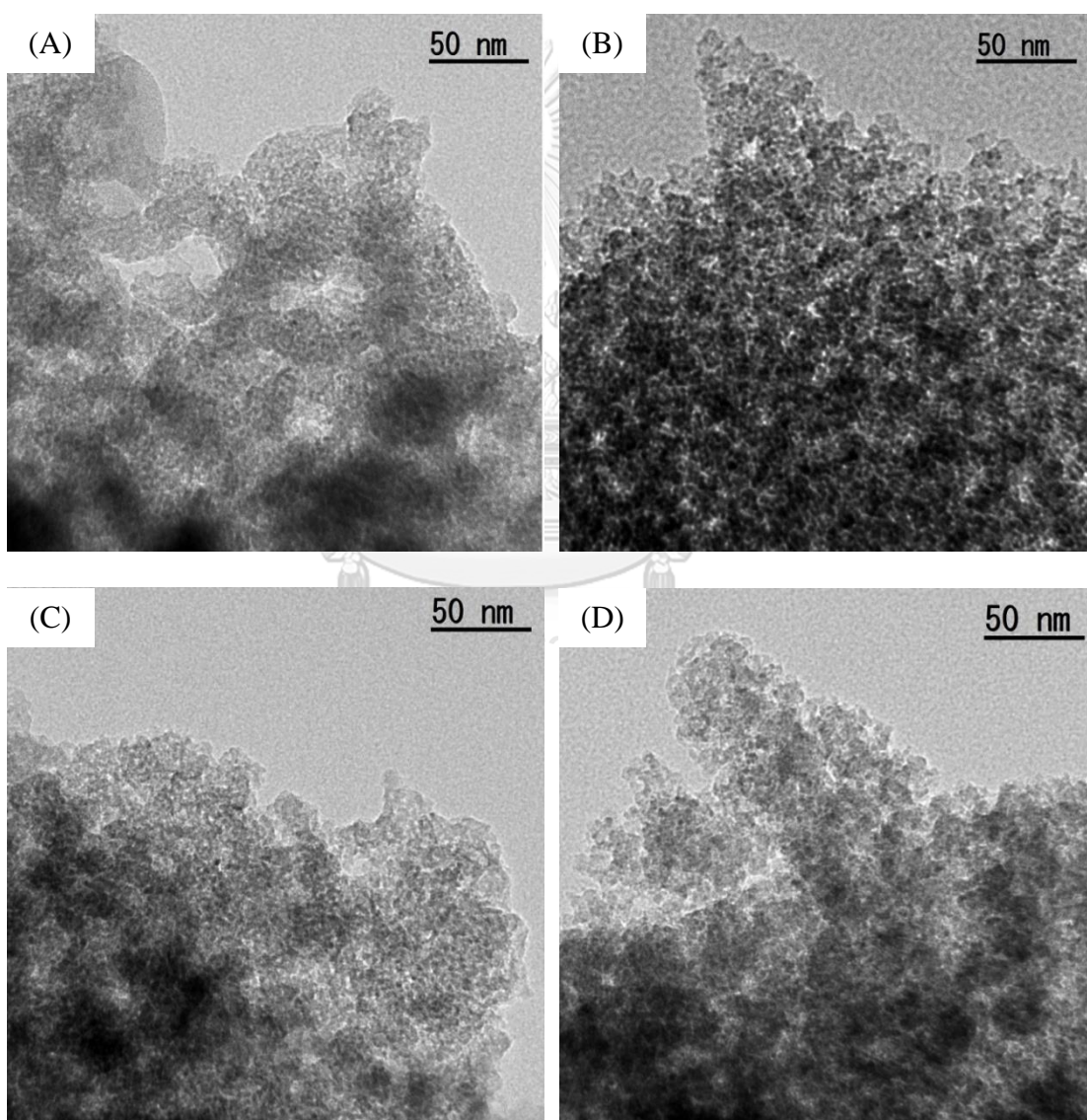


**Figure 4.16** TEM images of the (A) HMS, (B) NR/HMS, (C) MCS-0.5G-1.00M-700, and (D) MCS-0.5G-2.00M-700, all at a magnification of 100000 $\times$ .

#### 4.10 H<sub>2</sub>O adsorption measurement

The effects of carbon on the hydrophobic properties of MCS composites were investigated by water adsorption behavior at a low relative pressure. Figure 4.17 shows the H<sub>2</sub>O adsorption isotherms of the samples at  $P/P_0$  of 0–0.6. The NR/HMS exhibited a lower amount of adsorbed H<sub>2</sub>O than HMS due to the depletion of exposed surface silanol groups, as revealed by the FTIR analysis. The hydrophobic environment created by the rubber phase also reduced the interaction of H<sub>2</sub>O molecules onto the NR/HMS surface. Compared with the pure silica HMS, the MCS composites showed a lower adsorbed volume due to the hydrophobicity of carbon moieties dispersed in the MCS composites.

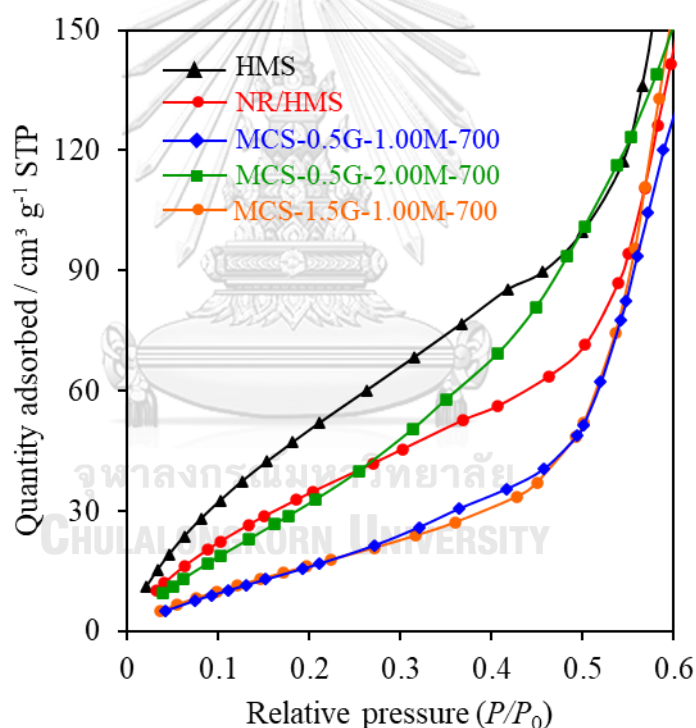


**Figure 4.17** Representative water adsorption isotherms of the (a) HMS, (b) NR/HMS, (c) MCS-0.5G-1.00M-700, (d) MCS-0.5G-2.00M-700, and (e) MCS-1.5G-1.00M-700 at the low relative pressures  $P/P_0$  in the range of 0–0.6.

Interestingly, MCS-0.5G-1.0M-700 and MCS-1.5G-1.0M-700 were more hydrophobic than their NR/HMS precursor. This was due to the depletion of silanol groups via dehydroxylation during the carbonization. Increasing the H<sub>2</sub>SO<sub>4</sub>

concentration resulted in an adverse effect on the hydrophobicity of the MCS composites, although the carbon residue content was promoted at a high  $\text{H}_2\text{SO}_4$  concentration. MCS-0.5G-2.0M-700 exhibited a higher amount of adsorbed  $\text{H}_2\text{O}$  than MCS-0.5G-1.0M-700, due to the higher content of oxygen-functional groups on the surface of MCS-0.5G-2.0M-700, as evidenced by the XPS results.

Analysis of the adsorption data at a low relative pressure (Table 4.7) indicated a decreased monolayer adsorption volume in the following order: HMS ( $82.9 \text{ cm}^3 \text{ g}^{-1}$ ) > MCS-0.5G-2.0M-700 ( $45.2 \text{ cm}^3 \text{ g}^{-1}$ ) > MCS-0.5G-0.05M-700 ( $41.6 \text{ cm}^3 \text{ g}^{-1}$ ) > NR/HMS ( $40.1 \text{ cm}^3 \text{ g}^{-1}$ ) > MCS-0.5G-1.0M-700 ( $22.0 \text{ cm}^3 \text{ g}^{-1}$ )  $\approx$  MCS-1.5G-1.0M-700 ( $22.0 \text{ cm}^3 \text{ g}^{-1}$ ). The result confirmed the tunable hydrophobic properties of the MCS composites, which provided them with potential applications in a broad area of adsorption, catalysis, and drug delivery.

**Table 4.7** Water adsorption volume of the pure silica HMS, NR/HMS precursor and MCS nanocomposites prepared under different conditions

Material	NR Content (g)	$\text{H}_2\text{SO}_4$ concentration (M)	Final temperature ( $^\circ\text{C}$ )	$V_m^k$ ( $\text{cm}^3 \text{ g}^{-1}$ )
HMS	0	-	550	82.9
NR/HMS <sup>a</sup>	0.5	0.05	-	40.1
MCS-0.5G-0.05M-700	0.5	0.05	700	41.6
MCS-0.5G-1.0M-700	0.5	1.00	700	22.0
MCS-0.5G-2.0M-700	0.5	2.00	700	45.2
MCS-1.5G-1.0M-700	1.5	1.00	700	22.0

n.d. = not determined.

<sup>a</sup> Extracted samples.

<sup>b</sup> Determined by water adsorption-desorption.



#### 4.11 SAXS analysis

SAXS technique was used to investigate the incorporation and distribution of rubber phase in the mesostructured silicate framework of NR/HMS. Figure 4.8 shows the SAXS patterns of organic-inorganic mesophases in the mixtures during the synthesis. In the case of NR/HMS, the peak at  $q = 1.46 \text{ nm}^{-1}$ , corresponding to the mesophase structure with a hexagonal unit cell of 0.68 nm, was found when the rubber gel was mixed with TEOS, DDA, and water. It was larger than the mesophase formed during the synthesis of pure silica HMS (unit cell = 0.58 nm) with the peak at  $q = 1.71 \text{ nm}^{-1}$ , because the rubber molecules incorporated into the organic-inorganic mesophase of NR/HMS and the hydrophobic environment created by the NR slowed the hydrolysis and condensation rate of the silicate species. The ethoxy groups adjacent to the rubber molecules remained non-hydrolyzed and acted as linkers between the rubber chains and the silicate oligomers, resulting in the mesostructured entrapped NR/silica composite framework. This was supported by the TEM and XRD analysis.

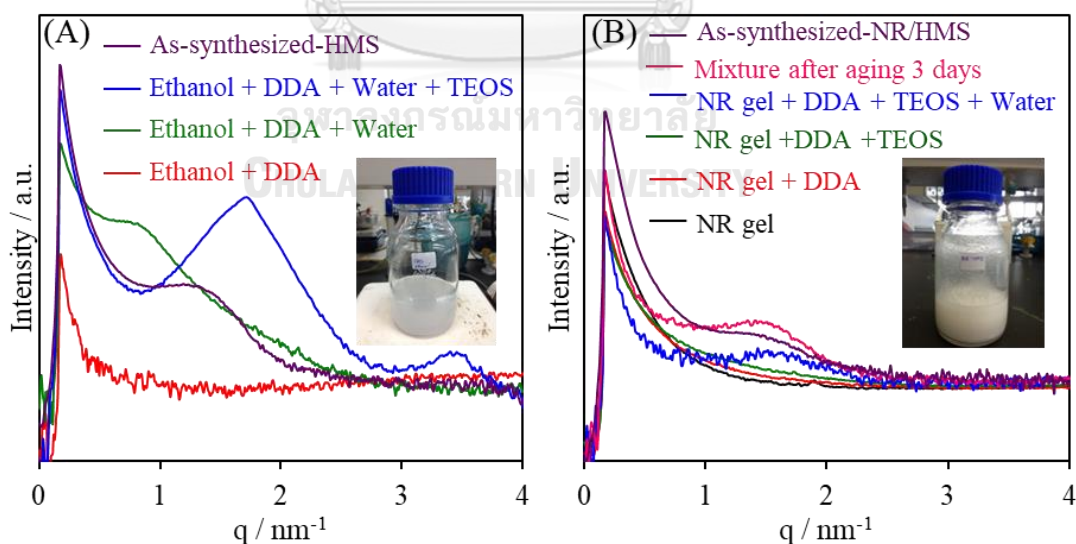


**Figure 4.18** SAXS patterns of the preparation of the as-synthesized (A) HMS and (B) NR/HMS with different compositions.



#### 4.12 Formation of mesoporous NR/HMS and MCS nanocomposites

According to the study in this chapter, the mechanistic model for the formation of NR/HMS composites synthesized via the *in situ* sol-gel process and conversion of the NR/HMS precursor into the MCS composites via carbonization, as illustrated in Figure 4.19. Firstly, TEOS and DDA were homogeneously dissolved in the NR solution using THF as the synthesis media. Upon adding H<sub>2</sub>O, TEOS was hydrolyzed to silicate species simultaneously with rearrangement of DDA molecules into hexagonal rod-like micelles, induced by H-bonding between the amine groups of DDA and the hydroxyl groups of the silicate species. The formation of an organic-inorganic mesophase in the mixtures during the NR/HMS synthesis was confirmed by the SAXS study. The resultant NR/HMS was then subjected to carbonization in an Ar atmosphere at 350 °C for 1 h, during which partial cyclization of NR was promoted via a H<sub>2</sub>SO<sub>4</sub>-catalyzed process. The temperature also promoted the condensation of the silicate framework, resulting in an improved ordering of the mesostructure. Further heating up to 700 °C converted the carbon residue into graphene-like oxide. The resulting MCS nanocomposite was characterized by a high dispersion of carbonaceous moieties, since their presence was determined by the location and dispersion of the rubber phase in the mesostructure of NR/HMS precursor. A previous study established that the interaction between the rubber and silica phase is rather weak, and could be extracted by toluene [28]. Moreover, the mesostructured framework was comprised of a genuine rubber/silica nanocomposite, which totally collapsed after the toluene extraction, indicating the highly dispersed NR molecules in the NR/HMS material. By controlling the acid concentration used in the treatment and subsequent carbonization temperature, the carbon content, surface functional groups, mesoporosity, and hydrophobicity of the resulting MCS nanocomposites could be tuned to meet the application requirement.

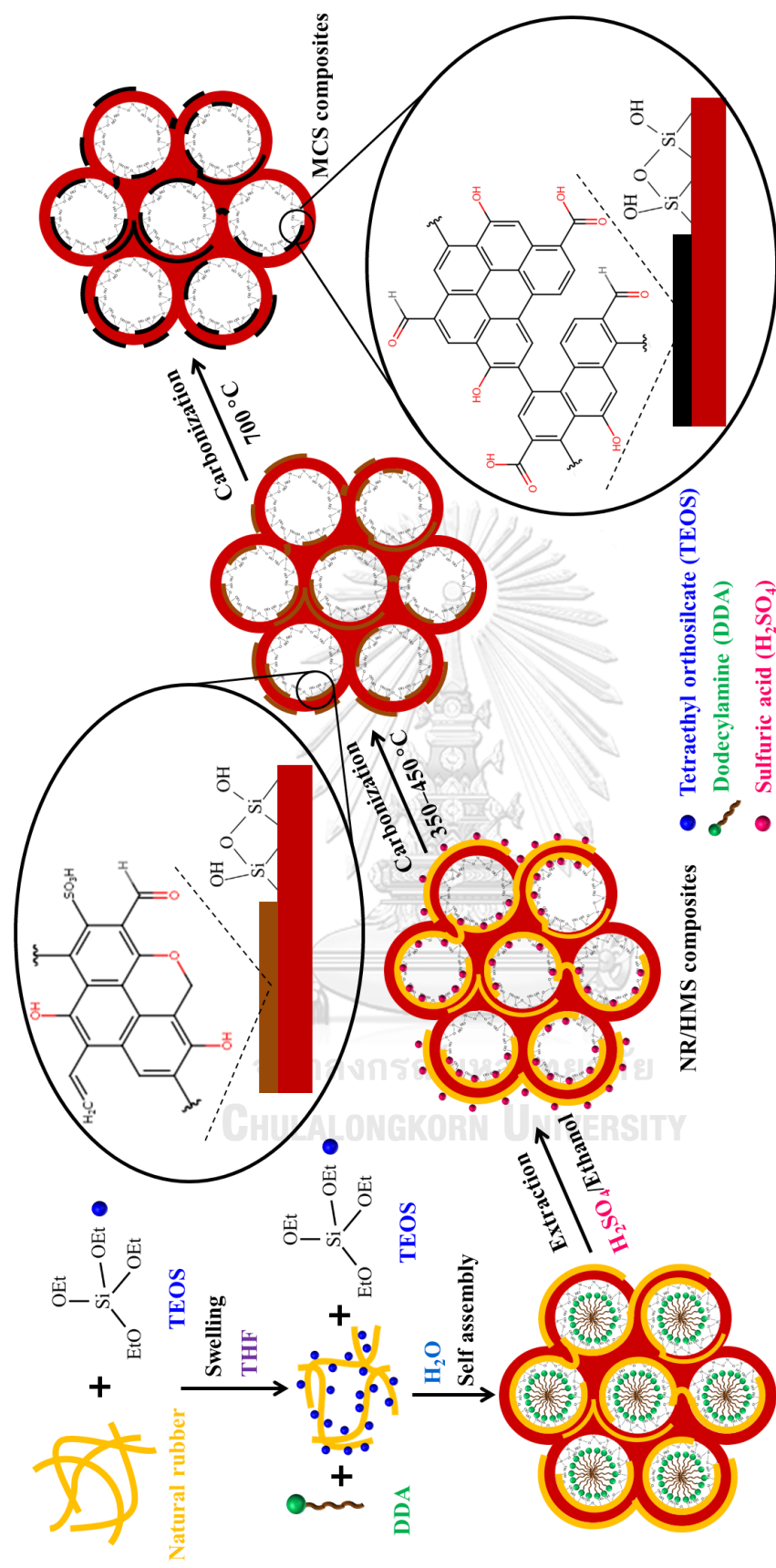


Figure 4.19 Mechanistic model for the formation of NR/HMS nanocomposites and their transformation to MCS materials.

## Chapter 5

### Functionalization and Characterization of MCS nanocomposites

In this Chapter, A series of acidic, basic, and bifunctional mesoporous carbon/silica materials were prepared. The synthesized MCS materials in this Chapter were prepared with the synthesis condition similarly to MCS-0.5G-1.00M-700 as described in Chapter III. The sulfonic acid-functionalized mesoporous carbon/silica (MCS-SO<sub>3</sub>H) was prepared by direct sulfonation with sulfuric acid (H<sub>2</sub>SO<sub>4</sub>) solution at difference concentration. Silica surface of MCS-SO<sub>3</sub>H were then grafted by 3-aminopropyltrimethoxysilane (APS) at difference concentration to produce the acid–base materials (MCS-SO<sub>3</sub>H-NH<sub>2</sub>). The MCS-SO<sub>3</sub>H and MCS-SO<sub>3</sub>H-NH<sub>2</sub> can take advantages from both surface functionalization with acid or/and base functional groups and hydrophobic carbon moieties to design the acidic composites and bifunctional acid-base composites with high mesoporosity and hydrophobicity. In addition, their structural, textural, and physicochemical properties were investigated in comparison with those of pure silica HMS, acidic HMS (HMS-SO<sub>3</sub>H) and acid–base hexagonal mesoporous silica (HMS-SO<sub>3</sub>H-NH<sub>2</sub>).

#### 5.1 Compositional and elemental analysis

The weight loss and differential thermal analysis (DTA) curves of MCS, MCS-18S, MCS-18S-0.2N and MCS-0.2N nanocomposites are shown in Figure 5.1. In all cases, the first-step weight loss between 30 and 120 °C was due to a loss of the physisorbed water and the last-step weight loss (~10 wt.%) in the range of 450–680 °C was related to the carbon residue. The MCS-18S revealed the decomposition of oxygen-containing groups functionalized on the carbon surface (2 wt.%) in the region of 230–350 °C. For MCS-18S-0.2N and MCS-0.2N, the weight loss at 220–450 °C was attributed to the decomposition of aminopropyl groups incorporated in the materials (8 wt%). More precisely, the change in DTA curve in this region was classified into 2 sub-steps [22]. The first step observed in the temperature range of 220–370 °C,

corresponded to the decomposition of amine moieties, whilst the second weight loss step (370–450 °C) was attributed to the decomposition of the hydrocarbon chain of aminopropyl groups. The carbon and silica content of pristine and functionalized MCS composites was summarized in Table 5.1

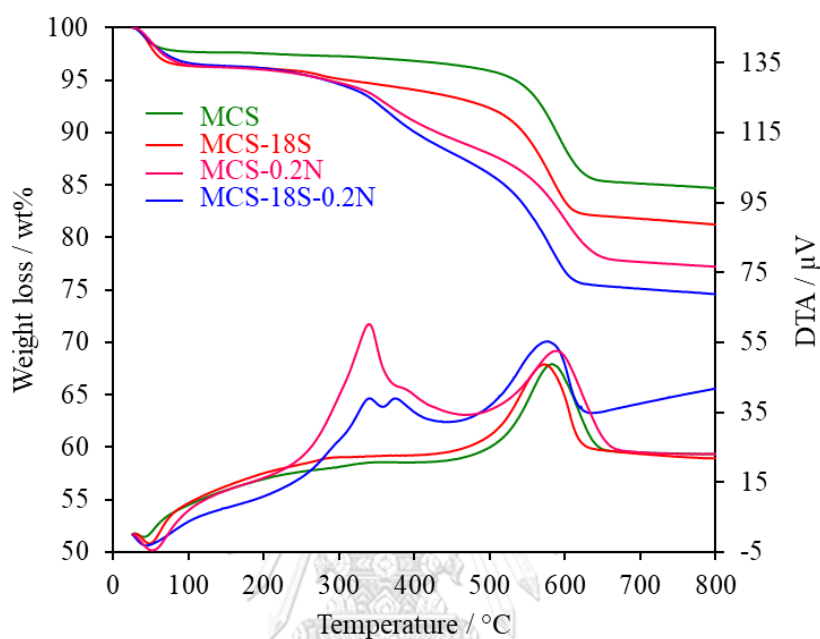


**Figure 5.1** Weight loss and DTA curves of (a) MCS, (b) MCS-18S, (c) MCS-0.2N and (d) MCS-18S-0.2N.

As shown in the Table 5.1, The carbon amount of MCS and MCS-18S materials was 10.4 and 11.4%, respectively. The functionalization with APS (MCS-0.2N and MCS-18S-0.2N) possessed silica content in the range of 81.2–84.7%, while a smaller amount of silica was observed for MCS and MCS-18S (74.6–77.2%) due to the incorporation of the organo-functional group in the HMS structure. In addition, the elemental analysis revealed that the nitrogen content of the bifunctional acid-base catalysts (1.36–1.49 mmol g<sup>-1</sup>) was superior to that of sulfur (0.30–0.34 mmol g<sup>-1</sup>). It was related to the fact that MCS contained only 11 wt.% carbon and silica matrix was the main component of mesostructured framework. For sulfonation of MCS, an increasing the H<sub>2</sub>SO<sub>4</sub> concentration from 5 to 15 mol% enhanced the sulfur content of MCS-SO<sub>3</sub>H from 0.29 to 0.40 mmol g<sup>-1</sup>. In the similar manner, the grafting of

aminopropyl groups on MCS-18S were increased from 1.36 to 1.49 mmol g<sup>-1</sup> when increasing APS concentration.

**Table 5.1** Chemical composition of HMS and MCS-based catalysts.

Sample	Carbon content <sup>a</sup> (wt.%)	Silica content <sup>a</sup> (wt.%)	Sulfur content <sup>b</sup> (mmol g <sup>-1</sup> )	Nitrogen content <sup>b</sup> (mmol g <sup>-1</sup> )
HMS	n.d.	n.d.	n.d.	n.d.
HMS-SO <sub>3</sub> H	n.d.	n.d.	1.51	n.d.
HMS-SO <sub>3</sub> H-NH <sub>2</sub>	n.d.	n.d.	1.42	1.46
MCS	10.4	84.7	0.07	n.d.
MCS-10S	n.d.	n.d.	0.29	n.d.
MCS-15S	n.d.	n.d.	0.32	n.d.
MCS-18S	11.4	81.2	0.40	n.d.
MCS-18S-0.1N	n.d.	n.d.	0.30	1.36
MCS-18S-0.2N	11.3	77.2	0.34	1.47
MCS-18S-0.3N	n.d.	n.d.	0.32	1.49
MCS-0.2N	12.7	74.6	0.06	1.65

n.d. = not determined.

<sup>a</sup> Determined by thermogravimetric analysis.

<sup>b</sup> Determined by CHNS analyzer.

## 5.2 XRD analysis

Figure 5.2 showed the XRD patterns of the functionalized HMS and MCS materials. The diffraction peaks of all materials, except for MCS-10S, were found at 2-Theta in the range of 1.0–3.0°, corresponding to characteristic (100) plane of the hexagonal mesoporous structure [22, 103]. The introduction of the organic species, either the carbon residue, propylsulfonic group or amino-propyl group into HMS decreased the order hexagonal mesostructure. The MCS-SO<sub>3</sub>H series sulfonated with different H<sub>2</sub>SO<sub>4</sub> concentration exhibited the characteristic peaks at lower 2-Theta positions than the parent MCS. The mesostructure ordering of MCS-SO<sub>3</sub>H nanocomposites were decrease when a decreased H<sub>2</sub>SO<sub>4</sub> concentration was used, which was in accord with an increased hydrolysis of silica by water in H<sub>2</sub>SO<sub>4</sub> solution [30]. An increased amount of APS (from 0.1 to 0.3 M) used in the post-grafting of MCS and MCS-18S detrimentally affected the structural order of the resulting MCS nanocomposites. It was due to a loss of mesostructured order at a high content of incorporated amino-propyl group in nanocomposite.

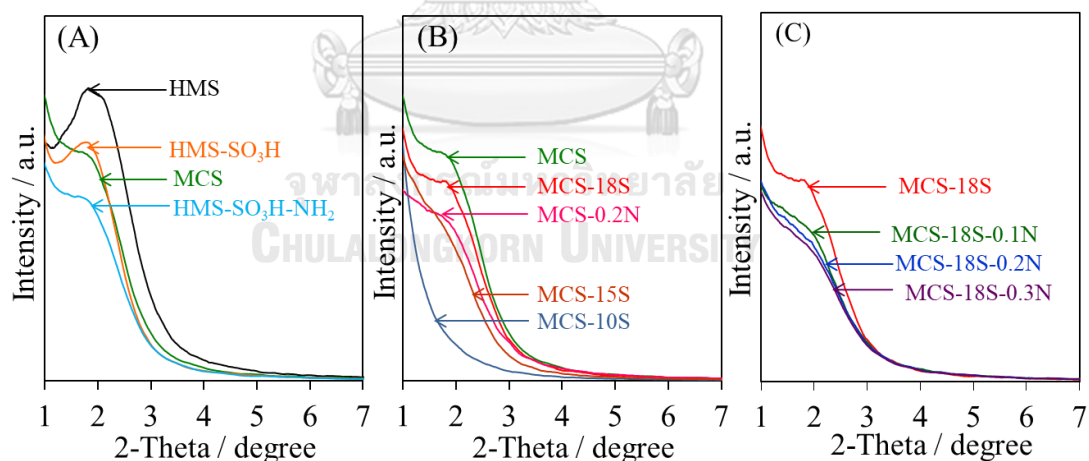


**Figure 5.2** XRD patterns of HMS and MCS with and without functionalization.

### 5.3 N<sub>2</sub> physisorption measurement

The functionalized HMS and MCS materials displayed type IV isotherms according to the IUPAC classification (Figure 5.3), which is characteristic of framework-confined mesoporous materials. As shown in Table 5.2, The introduction of organic species, either carbon residue, propyl sulfonic group, or aminopropyl group into HMS reduced the BET surface area ( $S_{\text{BET}}$ ), pore diameter ( $D_p$ ), and total pore volume ( $V_t$ ). The MCS-SO<sub>3</sub>H nanocomposites prepared with a low H<sub>2</sub>SO<sub>4</sub> concentration (MCS-10S) exhibited lower  $S_{\text{BET}}$  and  $V_t$ , whereas  $D_p$  was larger than the parent MCS (Table 5.2). These results show that the silica pore walls of MCS-SO<sub>3</sub>H were hydrolyzed by H<sub>2</sub>O, during the sulfonation process, resulting in mesopores interconnections, with a relatively poor mesostructured ordering [30]. An increase in H<sub>2</sub>SO<sub>4</sub> concentration enhanced  $S_{\text{BET}}$  and  $V_t$ , However,  $D_p$  was reduced due to the low amount of H<sub>2</sub>O available for silica hydrolysis. The  $S_{\text{BET}}$ ,  $V_t$ , and  $D_p$  of MCS-SO<sub>3</sub>H-NH<sub>2</sub>, decreased with increasing amount of APS (0.1–0.3 M) used in the post-grafting of MCS and MCS-18S, indicating that the aminopropyl group of APS incorporated into the pores of the MCS nanocomposites. The XRD and N<sub>2</sub> adsorption–desorption results suggested that the sulfonic acid and aminopropyl groups were attach on the surface of MCS composites.

**Table 5.2** Textural properties of HMS and MCS-based catalysts.

Sample	$S_{\text{BET}}^{\text{a}}$ ( $\text{m}^2 \text{g}^{-1}$ )	$D_{\text{p}}^{\text{b}}$ (nm)	$V_{\text{t}}^{\text{c}}$ ( $\text{cm}^3 \text{g}^{-1}$ )
HMS	905	2.64	1.93
HMS-SO <sub>3</sub> H	831	2.37	1.72
HMS-SO <sub>3</sub> H-NH <sub>2</sub>	480	2.00	1.26
MCS	664	2.37	1.41
MCS-10S	351	2.64	1.15
MCS-15S	512	2.50	1.24
MCS-18S	565	2.37	1.35
MCS-18S-0.1N	383	2.12	1.14
MCS-18S-0.2N	358	2.12	1.05
MCS-18S-0.3N	332	2.00	1.03
MCS-0.2N	484	2.12	1.21

n.d. = not determined.

<sup>a</sup> BET surface area.

<sup>b</sup> Pore diameter calculated using the BJH method.

<sup>c</sup> Total pore volume.



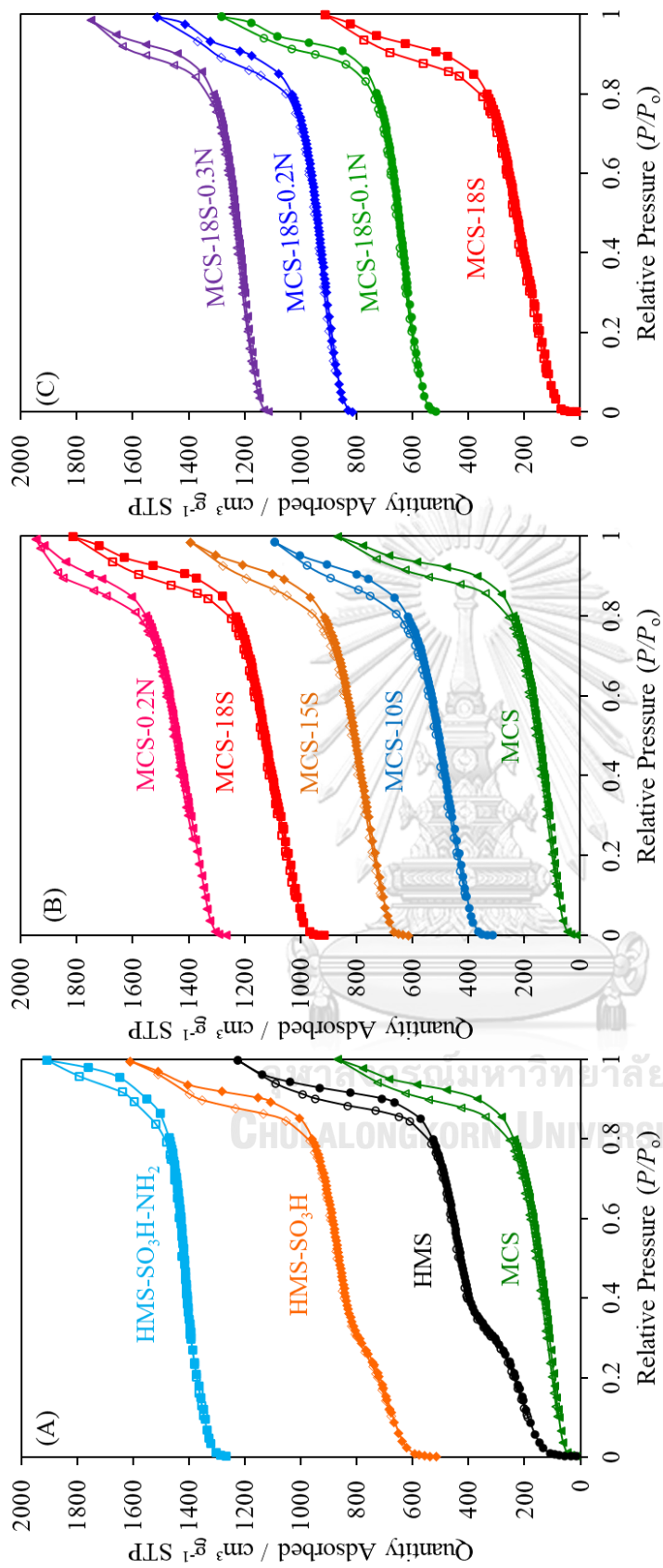
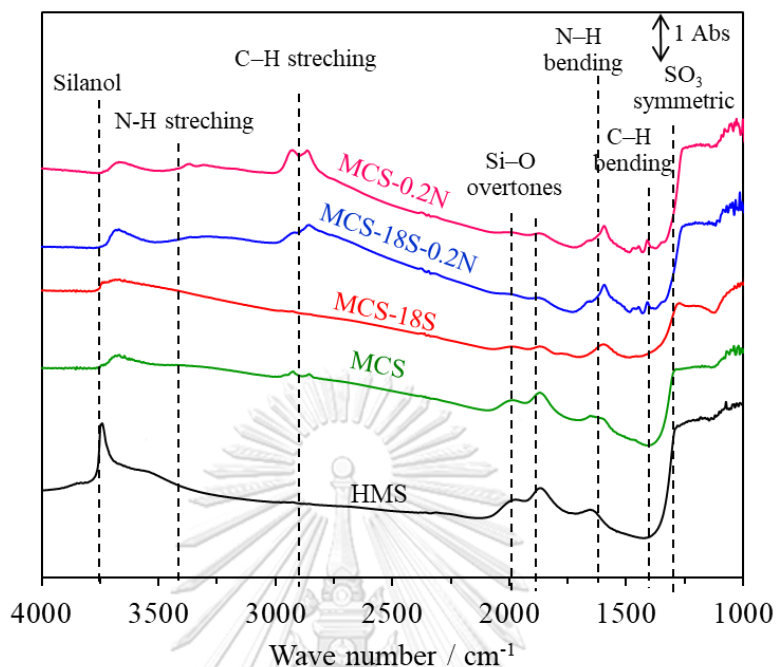


Figure 5.3  $N_2$  adsorption-desorption isotherms of HMS and MCS with and without functionalization.

## 5.4 FTIR spectroscopy



**Figure 5.4** FTIR spectra of the pure silica HMS, Parent MCS, MCS-18S, MCS-18S-0.2N and MCS-0.2N.

The FTIR analysis was used to confirm the presence of carbon residue or organo-functional groups in the mesostructured nanocomposites. As shown in Figure 5.4, The Si—O overtone of the silica framework of all mesoporous samples appeared between 1875 and 2100  $\text{cm}^{-1}$  [84]. The pure silica HMS exhibited an intense band at 3750  $\text{cm}^{-1}$  and a broad band at around 1640  $\text{cm}^{-1}$ , which can be assigned to free silanol groups (Si—OH) and vibration of physically absorbed water, respectively, [9]. The MCS showed additional bands related to the C—H stretching (2800–3000  $\text{cm}^{-1}$ ) and C=C—C aromatic stretching (1580–1615  $\text{cm}^{-1}$ ), as the characteristics of carbonaceous residue [103, 104]. After sulfonation (MCS-18S), the bands related to the sulfonic acid groups were observed at 1250  $\text{cm}^{-1}$  (S=O stretching) [30]. These results indicated that the carbonaceous phase in MCS was modified by  $\text{H}_2\text{SO}_4$ . The presence of amino-propyl group in MCS nanocomposites after functionalization with APS exhibited the bands between 3250 and 3500 (N—H stretching), 2850 and 2910

$\text{cm}^{-1}$  (C—H stretching of methylene groups), 1530 and 1640 (N—H bending) and around  $1410 \text{ cm}^{-1}$  (C—H bending) [22]. Indeed, all the MCS composites had a lower absorbance level of the free silanol band became obvious in the NR/HMS composite samples. These results could be interpreted as that the surface of HMS was covered with the carbon residue.

### 5.5 XPS analysis

The surface functional groups of the functionalized MCS nanocomposites were characterized by XPS in comparison with the pristine MCS. As shown in Figure 5.5A, the C1s XPS signals of all materials represented the binding energies in range of 282.0–289.9 eV. The spectra were further deconvoluted into four components, representing carbon groups (C=C,  $\text{CH}_x$  and C—C) at 284.9–285.0 eV, hydroxyl groups or ether linkages (C—O, C—O—C) at 285.9–286.0 eV, carbonyl groups (C=O) at 287.3 eV, and carboxyl or ester groups (C—O=O) at 289.1–289.4 eV [103]. For S1s XPS spectra (Figure 5.5B), The MCS-18 and MCS-18S-0.2N provided a similar S2p signal at 164.3 and 171.5 eV, corresponding to the S2p<sub>3/2</sub> and S2p<sub>1/2</sub> bands of sulfonic acid groups (—SO<sub>3</sub>H), respectively [20, 105, 106], indicating the successful sulfonation of MCS surface. In addition, the S2p signals at 164.0 and 164.9 eV were probably associated with the thiol groups (—SH) [107, 108], which could be generated via reduction of surface —SO<sub>3</sub>H groups [108]. The presence of amino groups on the surfaces of MCS nanocomposites were confirmed by N1s XPS spectra (Figure 4C). The band were deconvoluted into three component peaks centered at 398.8 eV, 400.2 eV, 401.7 eV and were assigned to —NH<sub>2</sub>, —CONH<sub>2</sub>, and —NH<sub>3</sub><sup>+</sup> functional groups, respectively [109], which indicate that the amine group of APS could react with the carboxylic acid group on the carbon surface, as well as protonate with hydrogen cation (H<sup>+</sup>) from acid sites.

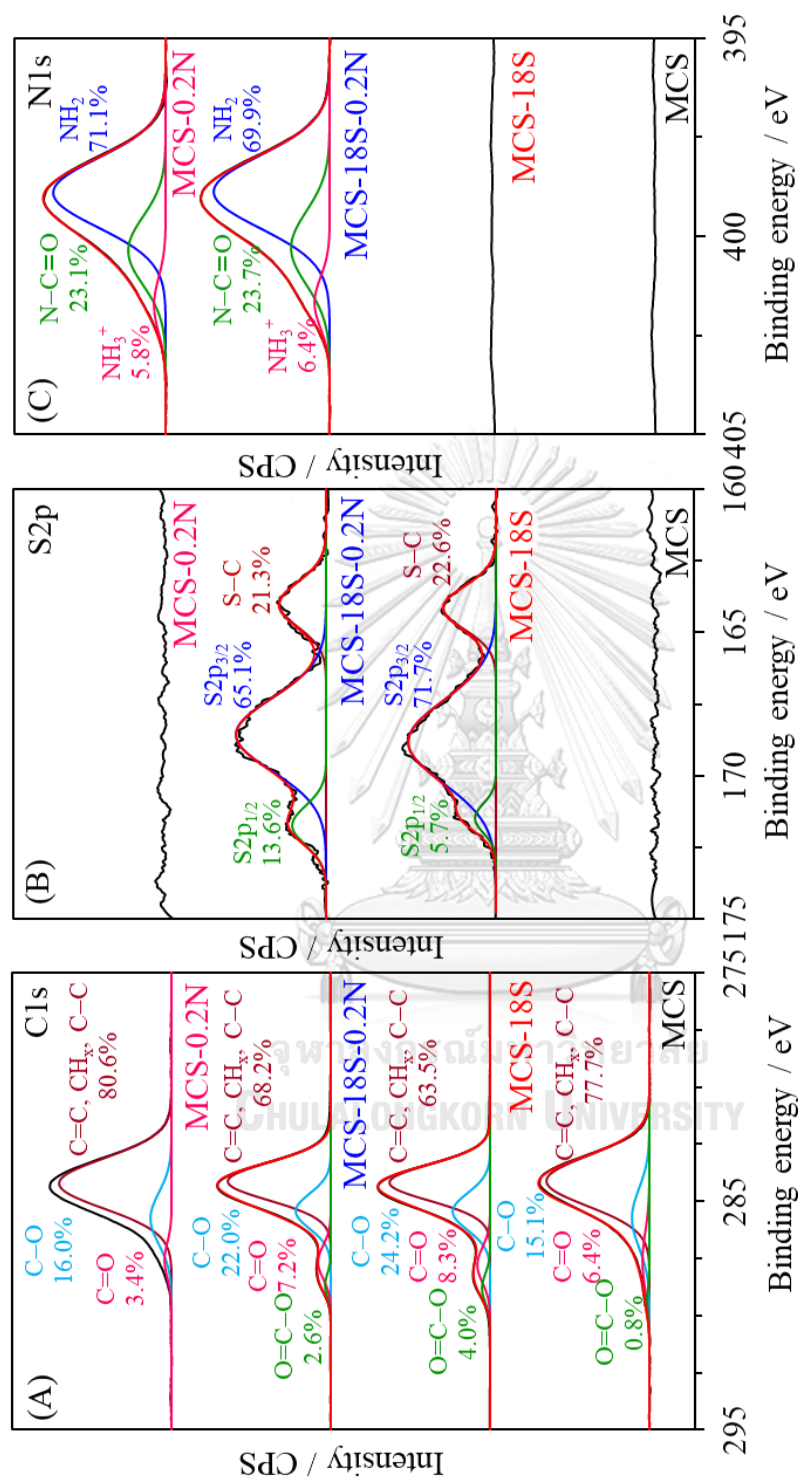


**Figure 5.5** (A) C1s, (B) N1s and (C) S2p XPS spectra of parent MCS, MCS-18S, MCS-18S-0.2N and MCS-0.2N.

## 5.6 Solid state $^{29}\text{Si}$ MAS NMR and $^{13}\text{C}$ CP/MAS NMR studies

The  $^{13}\text{C}$  NMR spectrum (Figure 5.6) of the MCS exhibited the chemical shift at 128 ppm, which attributed to aromatic carbon species [103]. After sulfonation (MCS-18S), the peak for aromatic carbon species decreased simultaneously with a new signal at 160 and 145 ppm, which can be assigned to COOH and phenolic OH respectively [110]. The result indicated that the oxygen-containing groups were enhanced by sulfonation with  $\text{H}_2\text{SO}_4$  in agreement with the XPS analysis. For MCS-18S-0.2N and MCS-0.2N, the chemical shift signals were of observed at 44, 25, and 9 ppm, which attributed to  $\text{N}-\text{CH}_2$ ,  $-\text{CH}_2-$ ,  $\text{Si}-\text{CH}_2-$ , respectively. These results corresponded to the propyl carbons of amino-propyl group in the MCS structure [111].

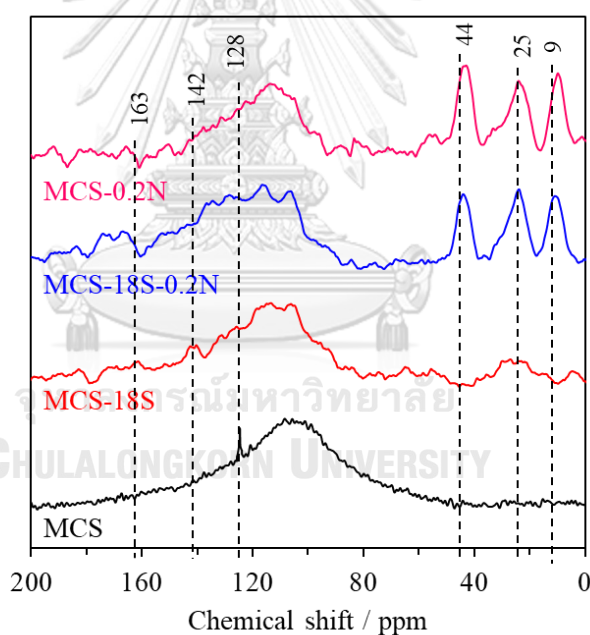


**Figure 5.6** Solid-state  $^{13}\text{C}$  CP/MAS NMR spectra of parent MCS, MCS-18S, MCS-18S-0.2N and MCS-0.2N.

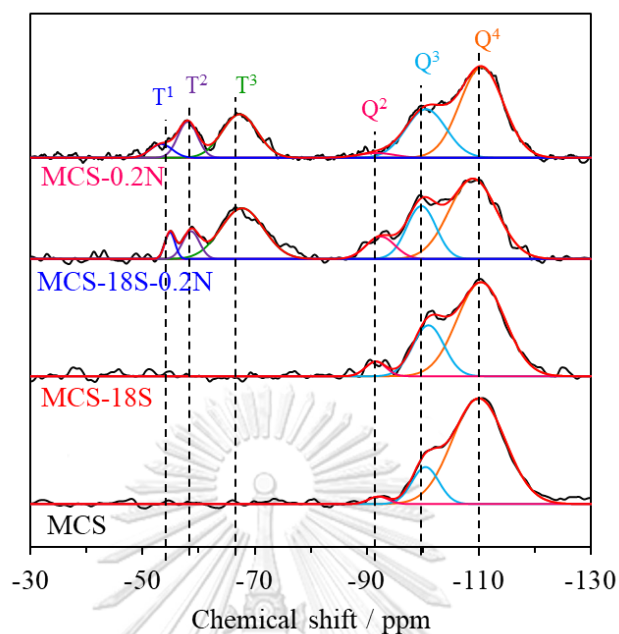


**Figure 5.7** Solid-state  $^{29}\text{Si}$  MAS NMR spectra of parent MCS, MCS-18S, MCS-18S-0.2N and MCS-0.2N.

**Table 5.3** Relative intensities of the  $T^m$  and  $Q^n$  groups

Sample	T <sup>1</sup> (%)	T <sup>2</sup> (%)	T <sup>3</sup> (%)	Q <sup>2</sup> (%)	Q <sup>3</sup> (%)	Q <sup>4</sup> (%)
MCS	-	-	-	2.2	14.8	83.0
MCS-18S	-	-	-	4.7	24.8	70.5
MCS-18S-0.2N	3.0	5.2	24.3	7.3	17.4	42.8
MCS-0.2N	3.5	8.2	17.7	2.0	22.7	45.8

As shown in Figure 5.7, the  $^{29}\text{Si}$  MAS NMR spectra of MCS with and without functionalization. The three resonance signals were observed at  $-92$ ,  $-101$ , and  $-110$  ppm, corresponding to  $Q^2$  ( $\text{Si}(\text{OSi})_2(\text{OH})_2$  or  $\text{Si}(\text{OSi})_2(\text{OEt})_2$ ),  $Q^3$  ( $\text{Si}(\text{OSi})_3(\text{OH})$  or  $\text{Si}(\text{OSi})_3(\text{OEt})$ ), and  $Q^4$  ( $\text{Si}(\text{OSi})_4$ ) species, respectively [20, 22]. The sulfonation of MCS (MCS-18S) exhibited higher fraction of  $Q^2$  and  $Q^3$  species than MCS composites (Table 5.3), indicating that the hydrolysis of silica phase was promoted in the

nanocomposite. After the functionalization with APS, three more signals were observed at  $-55$ ,  $-58$  and  $-68$  ppm, which attributed to  $T^1$  ( $\text{RSi}(\text{OSi})(\text{OH})_2$ ),  $T^2$  ( $\text{RSi}(\text{OSi})_2(\text{OH})$ ) and  $T^3$  ( $\text{RSi}(\text{OSi})_3$ ) sites, respectively, where R is the organofunctional group. Moreover, MCS-18S-0.2N possess the relative intensities of  $Q^2$  higher than MCS-18S due to the presence of remnant ethoxy groups of APS [22]. This result confirmed that the amino-propyl group were incorporated as a part of the MCS structure.

### 5.7 Raman spectroscopy

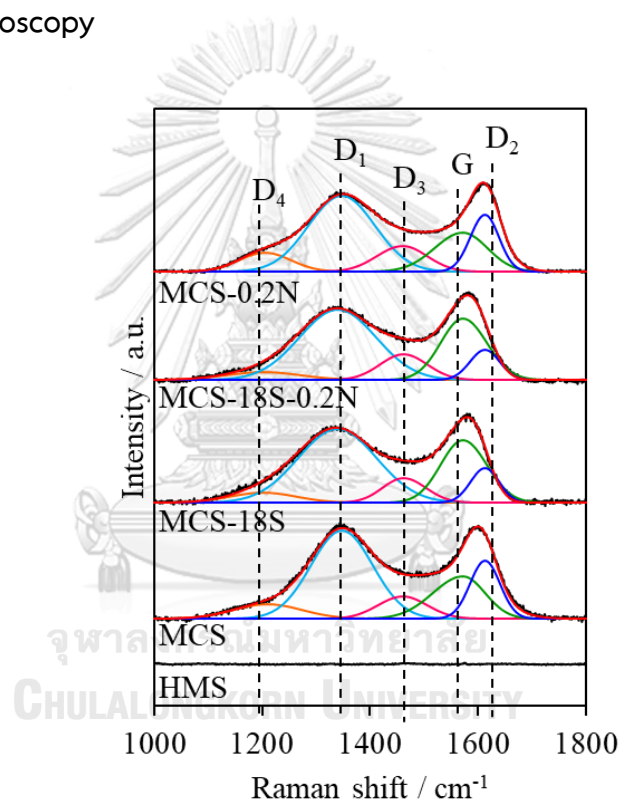


**Figure 5.8** Raman spectra of parent MCS, MCS-18S, MCS-18S-0.2N and MCS-0.2N.

The level of disorder of  $sp^2$  hybridized structure of the carbonaceous materials was investigated by using Raman spectroscopy [30, 103, 112]. The Raman spectra of all materials exhibited D band at  $1370 \text{ cm}^{-1}$  and G band at around  $1590 \text{ cm}^{-1}$  (Figure 5.8), which corresponded to the presence of structural defects in the hexagonal  $sp^2$  carbon lattice of graphene and the in-plane vibration of the  $sp^2$  carbon atoms, respectively [103]. The D and G bands can be deconvoluted into five components, which are assigned to polyenes ( $D_4$ ,  $1208 \text{ cm}^{-1}$ ), graphene edges ( $D_1$ ,

1352  $\text{cm}^{-1}$ ), amorphous carbon ( $D_3$ , 1472  $\text{cm}^{-1}$ ), graphitic carbon (G, 1572  $\text{cm}^{-1}$ ), and graphene sheets ( $D_2$ , 1612  $\text{cm}^{-1}$ ), respectively. The integral intensity of three bands at 1352  $\text{cm}^{-1}$  ( $D_1$ ), 1612 ( $D_2$ ) and 1572  $\text{cm}^{-1}$  (G) were performed to calculate degree of graphitization of carbon phase ( $I_{D1}/(I_G + I_{D1} + I_{D2})$ ) containing in the MCS nanocomposites as summarized in Table 5.4. The relative intensity ratio of  $I_{D1}/(I_G + I_{D1} + I_{D2})$  values of MCS-18S (0.62) and MCS-18S-0.2N (0.61) were higher than MCS (0.54) due to defect of generating oxygen-functional groups in carbon structure during sulfonation process [30]. However, after functionalization of MCS with APS, the  $I_{D1}/(I_G + I_{D1} + I_{D2})$  value of MCS-0.2N (0.57) was not significant differences with pristine MCS. These results indicate that the post-grafting functionalization of MCS with APS does not influence the carbon structure. These all above results suggest that sulfonic acid groups only attached to the surface of carbon after sulfonation, while the amino propyl group was attached to silica surface as show in Figure 5.9.

**Table 5.4** Raman spectroscopy results of the functionalized MCS Nanocomposites.

Sample	Relative area (%)					$I_{D1}/(I_{D1}+I_G+I_{D2})$
	$D_4$	$D_1$	$D_3$	G	$D_2$	
MCS	7.09	43.66	12.43	20.90	15.92	0.54
MCS-18S	5.86	52.73	9.53	23.11	8.77	0.62
MCS-18S-0.2N	5.76	50.30	11.91	23.52	8.51	0.61
MCS-0.2N	8.58	44.61	12.67	19.82	14.32	0.57



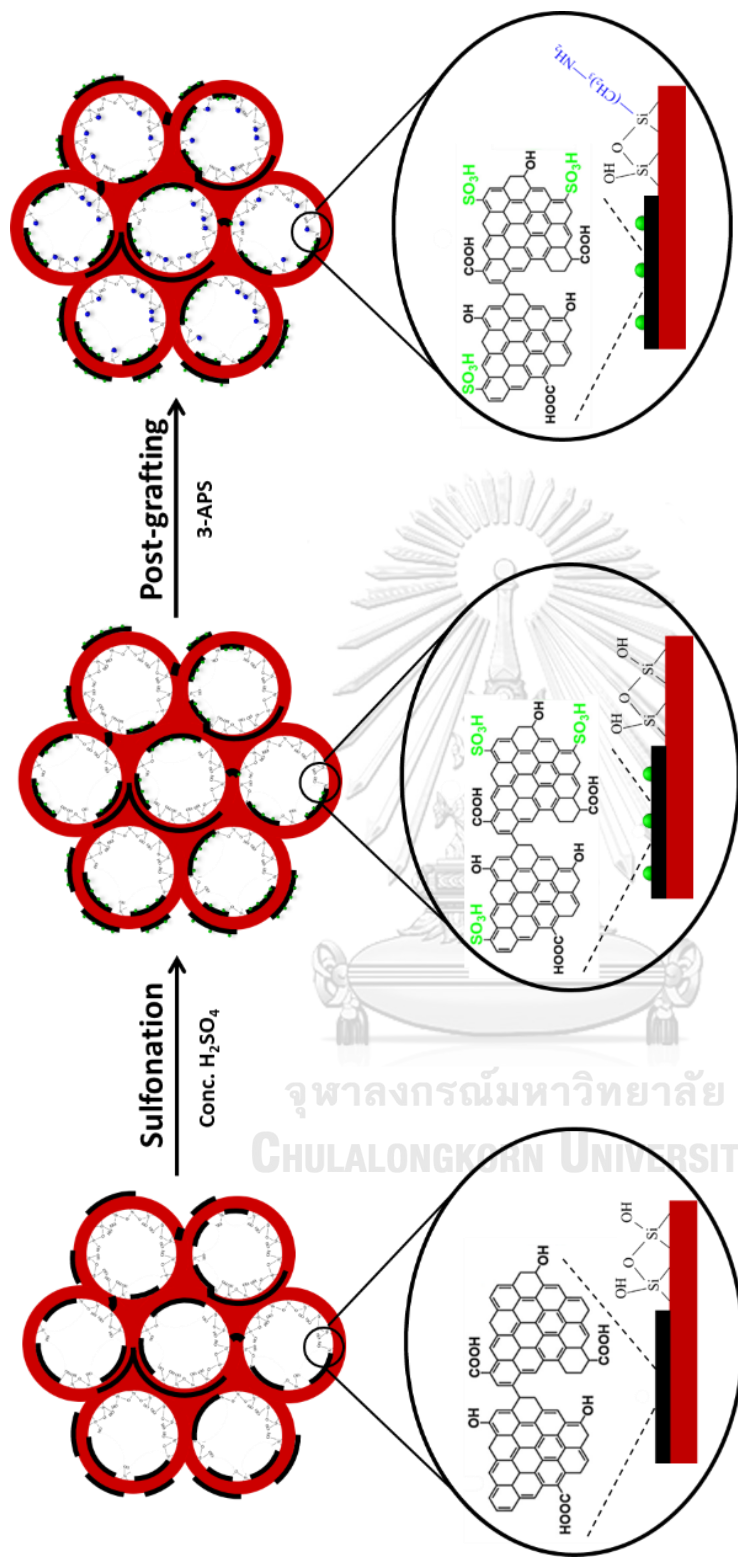


Figure 5.9 Schematic diagram showing the preparation process of acid and base functionalized MCS composites.

## 5.8 Acidity and basicity measurement

The acidity and basicity of representative MCS catalysts were investigated using back acid and base titration, while CHNS analysis was used to determine the amount of sulfur and nitrogen in the catalysts (Table 5.5). For HMS-SO<sub>3</sub>H, the number of acid sites was lower than the sulfur content, which suggested an incomplete oxidation of the thiol group to the sulfonic acid group. Further functionalization of HMS-SO<sub>3</sub>H to prepare the HMS-SO<sub>3</sub>H-NH<sub>2</sub> catalyst lowered the number of acid sites concomitantly with basicity generation. The acidity of MCS was originated from the acidic oxygen-functional groups on the carbon surface, in agreement with FTIR and XPS results. For the MCS-SO<sub>3</sub>H series, increasing the H<sub>2</sub>SO<sub>4</sub> concentration in the sulfonation process from 10 to 18 M (MCS-10S, MCS-15S, and MCS-18S) enhances the number of acid sites due to sulfonic acid group incorporation into the MCS, corresponding to the increasing sulfur content. Similarly, to the case of HMS-SO<sub>3</sub>H, the acidity of MCS-18S was decreased after functionalization with APS. The effect became magnified when increasing the APS concentrations (from MCS-18S-0.1N to MCS-18S-0.2N and MCS-18S-0.3N), and so the number of basic sites. This result indicates the acidic and basic groups were self-neutralized. However, the mass balance between the elemental composition and the acid-base content suggests other factors disturbing the back titration process. Possibly, some acid sites located on the carbon surface were not accessible after grafting the aminopropyl groups on the mesostructured silica framework. It was demonstrated that APS functionalization by post-grafting method resulted in a poor distribution of the organic groups due to a strong H-bonding character of amino moieties [113, 114].

**Table 5.5** Chemical composition, acidity and basicity of HMS and MCS-based catalysts.

Sample	Sulfur content <sup>a</sup> (mmol g <sup>-1</sup> )	Nitrogen content <sup>a</sup> (mmol g <sup>-1</sup> )	Acidity <sup>b</sup> (mmol H <sup>+</sup> g <sup>-1</sup> )	Basicity <sup>b</sup> (mmol OH <sup>-</sup> g <sup>-1</sup> )
HMS	n.d.	n.d.	n.d.	n.d.
HMS-SO <sub>3</sub> H	1.51	n.d.	1.34	n.d.
HMS-SO <sub>3</sub> H-NH <sub>2</sub>	1.42	1.46	0.12	1.11
MCS	0.07	n.d.	1.11	n.d.
MCS-10S	0.29	n.d.	1.27	n.d.
MCS-15S	0.32	n.d.	1.38	n.d.
MCS-18S	0.40	n.d.	1.43	n.d.
MCS-18S-0.1N	0.30	1.36	0.20	0.93
MCS-18S-0.2N	0.34	1.47	0.12	1.18
MCS-18S-0.3N	0.32	1.49	0.10	1.21
MCS-0.2N	0.06	1.65	n.d.	1.34

n.d. = not determined.

<sup>a</sup> Determined by CHNS analyzer.

<sup>b</sup> Determined by back acid-base titration with HCl aq. (0.01 M) and NaOH aq. (0.01 M).

## 5.9 H<sub>2</sub>O adsorption measurement

The effects of incorporating acid-base functional group and carbonaceous residue on the hydrophobicity of representative HMS and MCS catalysts were measured using H<sub>2</sub>O sorption measurement (Table 5.6). The HMS-SO<sub>3</sub>H (63.55 cm<sup>3</sup> g<sup>-1</sup>) and HMS-SO<sub>3</sub>H-NH<sub>2</sub> (57.93 cm<sup>3</sup> g<sup>-1</sup>) revealed a lower monolayer-adsorbed volume ( $V_m$ ) of H<sub>2</sub>O than HMS (82.89 cm<sup>3</sup> g<sup>-1</sup>) due to the presence of the propyl sulfonic acid and aminopropyl groups and the reduction of silanol groups in the HMS structure. The MCS catalyst series exhibited a lower H<sub>2</sub>O adsorbed volume than HMS due to the reduction of surface silanol groups and dispersion of hydrophobic carbon residue in the resulting nanocomposites, as seen from the FTIR (see also Figure 5.4) analysis. The H<sub>2</sub>O adsorbed volume of MCS-SO<sub>3</sub>H (MCS-10S, MCS-15S, and MCS-18S) increased as H<sub>2</sub>SO<sub>4</sub> concentration increases during the sulfonation process (Table 5.6). Increased level of hydrophilic oxygen-containing groups and sulfonic acid groups caused by sulfonation in the sulfonated MCS nanocomposites, as shown in the XPS result (see also Figure 5.5A and 5.5C), explain the increase in the H<sub>2</sub>O affinity observed in the catalyst. The MCS-SO<sub>3</sub>H-NH<sub>2</sub> exhibited a lower volume of the adsorbed H<sub>2</sub>O monolayer than MCS-SO<sub>3</sub>H owing to the grafting of organosilane onto the silica wall structure, thus, reduction of the silanol group in the MCS structure, as confirmed by the <sup>29</sup>Si MAS NMR data (see also Figure 5.7). The volume per unit mass of the adsorbed H<sub>2</sub>O monolayer on the MCS-18S-0.1N, MCS-18S-0.2N, and MCS-18S-0.3N catalysts were found to be 35.13, 32.75, and 31.98 cm<sup>3</sup> g<sup>-1</sup>, respectively. These results suggest that the MCS-based catalysts had a higher hydrophobic character than the HMS-based catalysts due to the incorporated hydrophobic-carbonaceous residue.

**Table 5.6** Water adsorption volume of HMS and MCS-based catalysts.

Sample	$V_m^a$ ( $\text{cm}^3 \text{g}^{-1}$ )
HMS	82.89
HMS-SO <sub>3</sub> H	63.55
HMS-SO <sub>3</sub> H-NH <sub>2</sub>	57.95
MCS	22.52
MCS-10S	39.76
MCS-15S	46.25
MCS-18S	49.56
MCS-18S-0.1N	35.13
MCS-18S-0.2N	32.75
MCS-18S-0.3N	31.98
MCS-0.2N	32.32

n.d. = not determined.

<sup>a</sup> Determined by water adsorption–desorption.

## Chapter 6

### Catalytic activity of synthesized composites in HMF synthesis

In this Chapter, the sulfonic acid-functionalized mesoporous carbon/silica (MCS-SO<sub>3</sub>H) used as the solid acid catalysts for dehydration of fructose. Silica surface of MCS-SO<sub>3</sub>H were then grafted by 3-aminopropyltrimethoxysilane to produce the acid–base catalyst (MCS-SO<sub>3</sub>H-NH<sub>2</sub>). Then these materials were tested in the conversion of glucose to HMF. The reaction was performed in a biphasic solvent system of THF and NaCl aqueous solution. To investigate the advantage of hydrophobicity of functionalized MCS on the catalytic conversion of fructose and glucose, they compared with those of pure silica HMS, acidic HMS (HMS-SO<sub>3</sub>H) and acid–base hexagonal mesoporous silica (HMS-SO<sub>3</sub>H-NH<sub>2</sub>). Moreover, the effect of acid and base ratio on the catalytic performance of bifunctional acid-base MCS catalysts in glucose dehydration was investigated. The reaction condition and amount of MCS-SO<sub>3</sub>H-NH<sub>2</sub> catalyst were also studied in order to achieve high HMF yield in the catalytic glucose dehydration. In addition, MCS-SO<sub>3</sub>H-NH<sub>2</sub> was investigated for the reusability in the dehydration of glucose.

#### 6.1 Dehydration of fructose into HMF

Dehydration of fructose into HMF was studied over HMS and MCS-based catalysts. The reaction was carried out in a biphasic solvent (aqueous NaCl solution/THF) using a Teflon-lined stainless-steel autoclave. The catalytic performance of catalysts in the dehydration of fructose were summarized Table 2. The dehydration of fructose into HMF was favored on Brønsted basic sites [71]. However, the Brønsted acid site catalyzes the hydrolysis of HMF into LVA and 2,5-dioxo-6-hydroxyhexanal, as reactive monomers for humins growth [115]. The parent MCS revealed higher HMF yield than pure silica HMS due to the promotion of HMF production by acidic oxygen-functional groups, which act as Brønsted acid sites on the carbon surface. Moreover, HMS provided the humins yield higher than MCS due

to the affinity for H<sub>2</sub>O of HMS, as revealed by the H<sub>2</sub>O physisorption. The fructose conversion and HMF formation increased with increasing the number of acid sites onto MCS by sulfonation (from MCS to MCS-10S, MCS-15S, and MCS-18S), whereas the humins yield decreased due to the higher HMF formation rate than humins formation rate in MCS base catalyst, indicating that the formation of humins was retarded the hydrophobicity of MCS. Comparison with HMS-SO<sub>3</sub>H confirmed the result. In addition, LVA formation was observed over HMS-SO<sub>3</sub>H because of the high surface water affinity in the HMS base catalyst. The formation of glucose was observed over the MCS-0.2N catalyst due to fructose isomerization promotion by aminopropyl groups, acting as Brønsted base sites. Moreover, MCS-0.2N catalyst provided high humins yield owing to the polymerization of HMF itself, or with fructose to humins, by the amine base group through aldol condensation of aldehydes and ketones [116]. Therefore, a low HMF yield was observed over MCS-0.2N.

**Table 6.1** Transformation of fructose to HMF over HMS and MCS-based catalysts.

Catalyst	Conversion of fructose (mol%)	Yield (mol%)				
		Glucose	HMF	LVA	FF	Humins
HMS	67.2	0.0	32.3	0.0	0.1	34.8
MCS	68.2	0.0	41.6	0.0	0.5	26.1
MCS-10S	72.2	0.0	45.5	0.0	0.4	26.3
MCS-15S	73.6	0.0	47.2	0.0	0.5	25.9
MCS-18S	81.0	0.0	56.0	0.0	0.6	24.4
HMS-SO <sub>3</sub> H	87.6	0.0	50.9	7.1	0.6	29.0
MCS-0.2N	67.0	8.5	11.8	0.0	0.4	46.3

Reaction conditions: 100 mg catalyst, 5 ml of 200 mM fructose in NaCl solution, 10 ml THF, 150 C, 2 h.

## 6.2 Conversion of glucose into HMF

### 6.2.1 Effect of Catalyst Functionality on Glucose Conversion into HMF

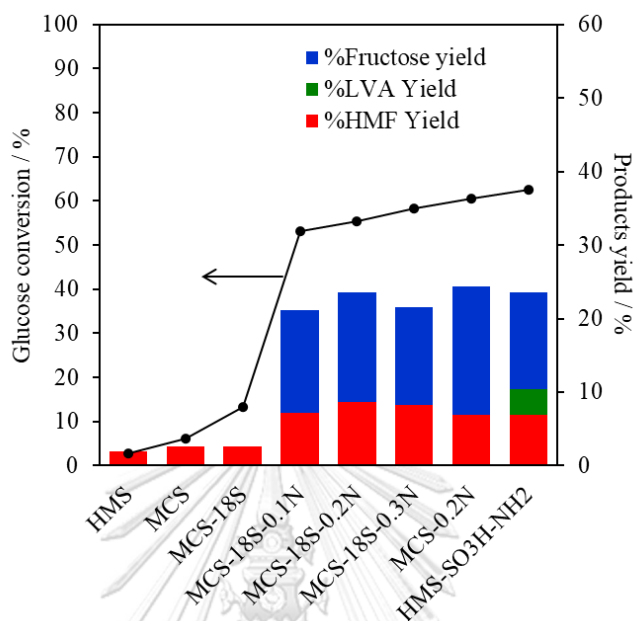


**Figure 6.1** Glucose conversion over functionalized HMS and MCS composites. Reaction conditions: 100 mg catalyst, 5 ml of 200 mM glucose in NaCl solution, 10 ml THF, 150 °C, 2 h.

The glucose conversion and product yield in the dehydration of glucose over various catalysts in the THF/H<sub>2</sub>O system are shown in Figure 6.1. MCS and MCS-18S catalyzed glucose conversion into HMF via direct dehydration over Brønsted acid sites. However, glucose conversion and HMF yield were low. The introduction of amine-functional groups onto MCS, giving the MCS-0.2N, led to higher glucose conversion and fructose yield than MCS and MCS-18S due to an promoted glucose isomerization into fructose by aminopropyl group, which act as Brønsted base sites [72, 117]. In addition, the presence of acidic oxygen-functional groups on carbon possibly catalyzes the fructose dehydration into HMF over MCS-0.2N. The combined sulfonic acid and aminopropyl groups of the MCS-18S-xN series enhanced the HMF formation because of the promoted isomerization and dehydration rate. An increase in the amine-content promoted glucose conversion and HMF yield of which MCS-18S-0.2N, an amine content of 1.47 mmol g<sup>-1</sup>, provided 8.7% HMF yield at 55%



glucose conversion. However, increased amine content ( $1.49 \text{ mmol g}^{-1}$ ) of MCS-18S-0.3N resulted in a drop in HMF yield owing to an increased aldol condensation of HMF itself, or with fructose and glucose, into humins [118]. Compared to MCS-18S-0.2N, HMS- $\text{SO}_3\text{H-NH}_2$  promoted the hydrolysis of HMF into LVA and humins. This result was ascribed by hydrophobicity/hydrophilicity derived from mesoporous supports. Therefore, it can be concluded that the presence of carbon in the composites retards the hydrolysis of HMF into undesired byproducts.

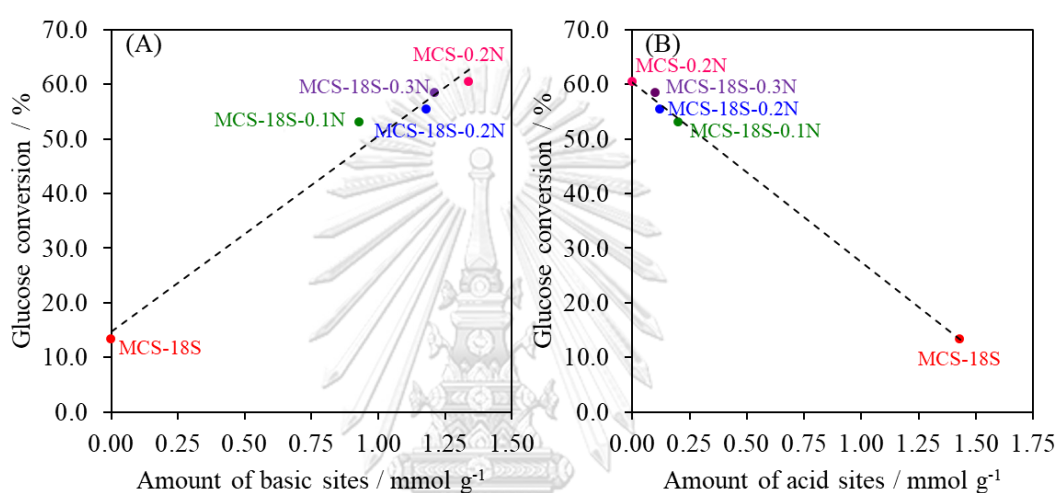


**Figure 6.2** Relationship of (A) number of basic sites and (B) number of acid sites over functionalized HMS and MCS composites.

Figure 6.2A shows a positive correlation between the number of Brønsted basic sites and glucose conversion, which indicated that the basic sites promote the conversion of glucose. This result was similar to the work reported by Liu et al. [119], who observed an enhanced isomerization of glucose to fructose by increasing the concentration of organic amines as homogeneous Brønsted base catalysts. However, glucose conversion decreased as the acid concentration increases (Fig. 6.2B). MCS-18S with the highest acidity ( $1.43 \text{ mmol g}^{-1}$ ) was the least effective catalyst due to thermodynamic constraints of glucose dehydration in the presence of Brønsted acid [120, 121].

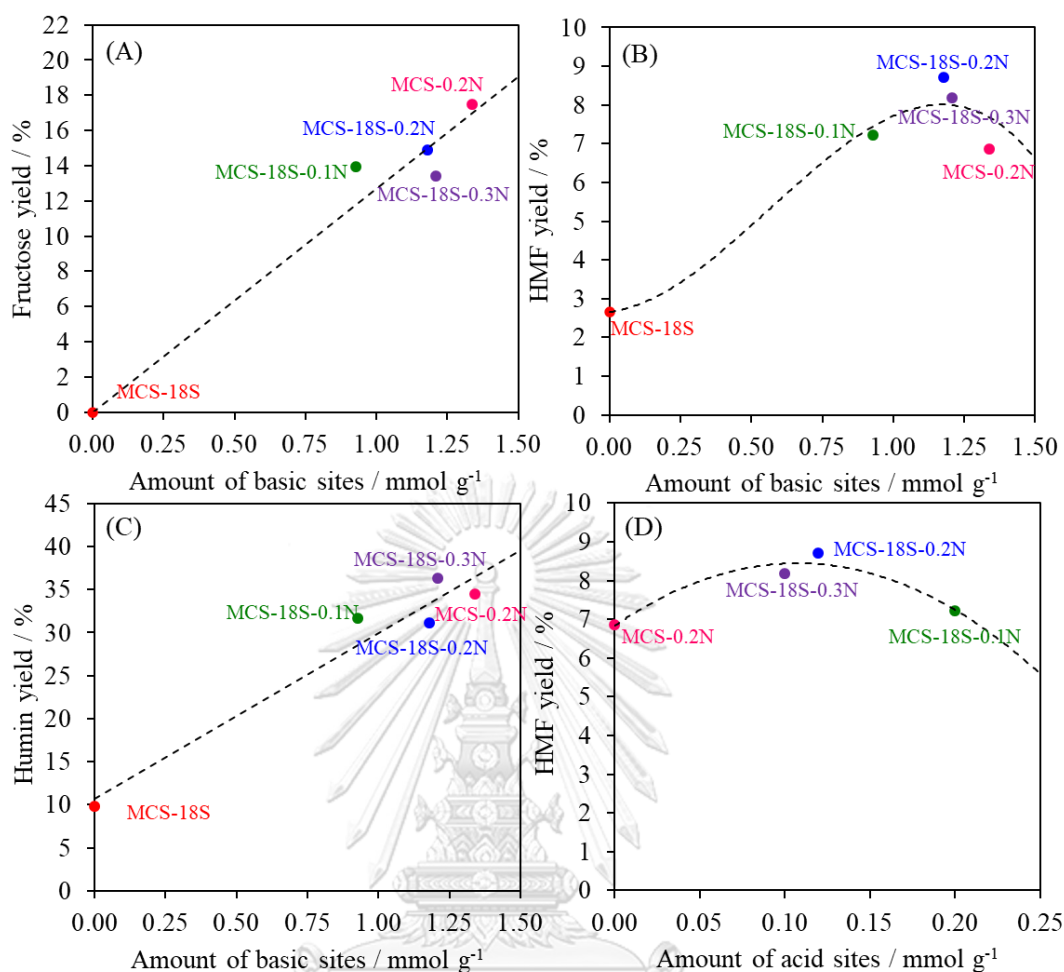


**Figure 6.3** Relationship of the fructose, HMF, and humins yield and number of basic sites and acid sites from glucose conversion over functionalized HMS and MCS composites.

The relationship between the fructose, HMF and humins yield and number of basic sites are illustrated in Figure 6.3A–C. With an increasing number of basic sites, the fructose, HMF and humins yield increased, but HMF yield declined in high basicity conditions due to condensation of HMF to humins [118]. These results indicated that the basic sites not only promoted isomerization of glucose to fructose, but also promoted the formation of humins. The relationship between the HMF yield and number of acid sites is illustrated in Figure 6D. The HMF formation over functionalized MCS catalysts increased with increasing number of acid sites, but it decreased in high acid conditions. The drop in the HMF yield over MCS-18S-0.1N with a high acid content implied that some acid sites were not involved in the

dehydration of fructose to HMF. The highest HMF yield of 8.7% was obtained over MCS-18S-0.2N with 55.3% glucose conversion. Suitable amounts of Brønsted basic/acid sites and hydrophobicity are the key to gain the highest yield HMF. Therefore, experiments were performed over the MCS-18S-0.2N catalyst in the following sections.

### 6.2.2 Effect of reaction temperature and time

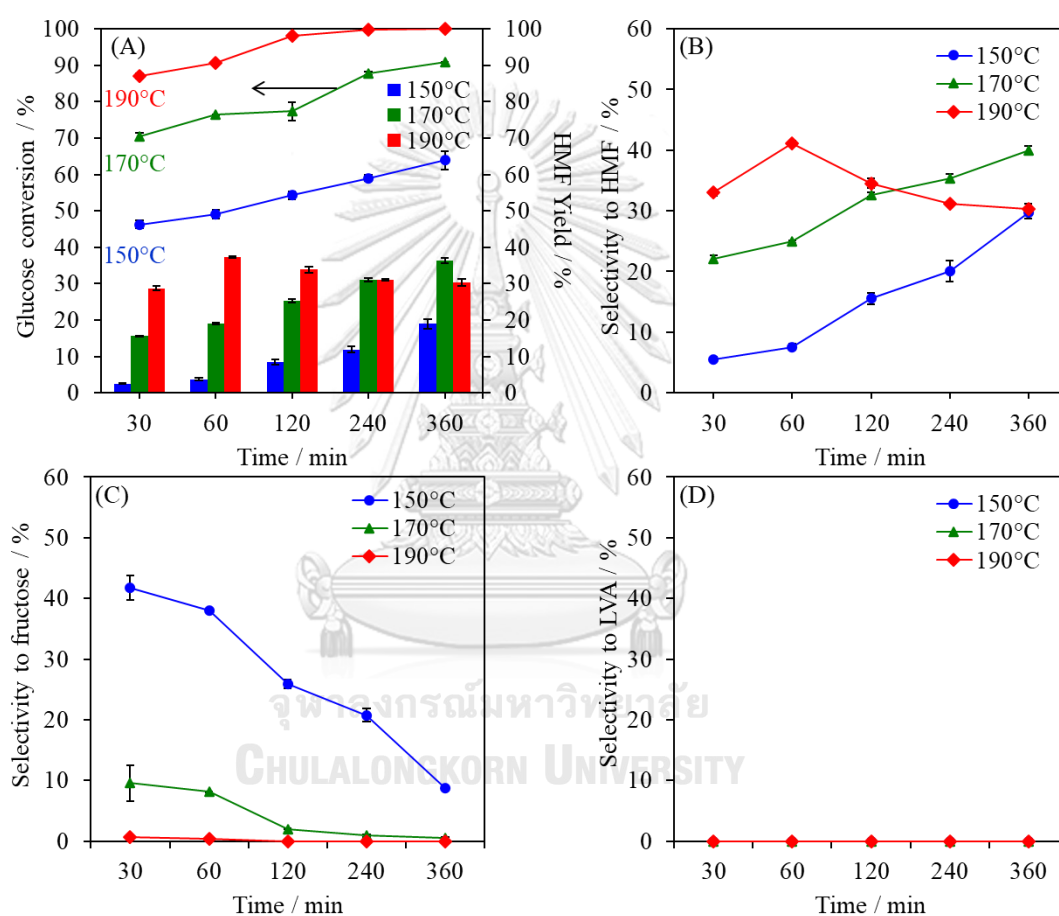


**Figure 6.4** Effect of temperature and reaction time on glucose conversion to HMF catalyzed by MCS-18S-0.2N. Reaction conditions: 5 mL 0.2-M glucose in NaCl solution, 10 mL THF, 100 mg MCS-18S-0.2N.

The glucose conversion, product yields, and product selectivity as functions of reaction time at temperatures of 150–190 °C are shown in Figure 6.4. The HMF yield is 19% at the conversion of glucose below 63% within 360 min at a lower

temperature (150 °C), whereas a high fructose selectivity was achieved. Further increasing the reaction temperature to 170 °C, the glucose conversion and HMF selectivity increase (Figure 6.4A and B), the selectivity to fructose decreased (Figure 6.4C) due to the endothermic nature of the glucose dehydration [76]. The reaction temperature of 190 °C provided the highest HMF yield (37.3%) at 91% glucose conversion within 60 min. However, the HMF yield and selectivity decreased when the reaction time exceeded 360 min. Fructose is an important intermediate for humin formation. Swift et al.[3] reported that the activation energy of fructose condensation to humins (127 kJ mol<sup>-1</sup>) is similar to that of fructose dehydration to HMF (114 kJ mol<sup>-1</sup>); thus, increasing the reaction temperature accelerated both routes. Moreover, the transformation of HMF to humins was increased at a longer reaction time [3]. Therefore, the reaction temperature of 190 °C and the reaction time of 60 min were adopted as the optimal reaction conditions. In addition, the levulinic acid formation, which was derived by hydration of HMF acid, was not observed over MCS-18S-0.2N catalyst (Figure 8D). These results suggested that the formation of levulinic acid, as a by-product from HMF hydrolysis, was retarded over the bifunctional acid-base MCS catalyst.

### 6.2.3 Effect of catalyst amount

The effects of catalyst loading on the glucose dehydration were studied by using different amount of the bifunctional acid-base MCS catalyst (MCS-18S-0.2N). The catalyst loading is an important parameter that needs to be optimized to increase the HMF yield. The effect of catalyst amount on glucose dehydration is shown in Figure 6.5. The glucose conversion and HMF yield increase with the increase of catalyst dosage due to higher active sites promoting dehydration of glucose into HMF in reaction systems. However, with increasing catalyst amount over 50 mg of MCS-18S-0.2N catalyst, HMF yield was dropped concomitantly with an increased humins because the increasing amount of catalyst increased basicity and acidity in reaction system, resulting in promoted condensation of HMF into humin [115, 118]. Therefore, the optimum catalyst dosage of MCS-18S-0.2N was 50 mg with highest 39.4% HMF yield.

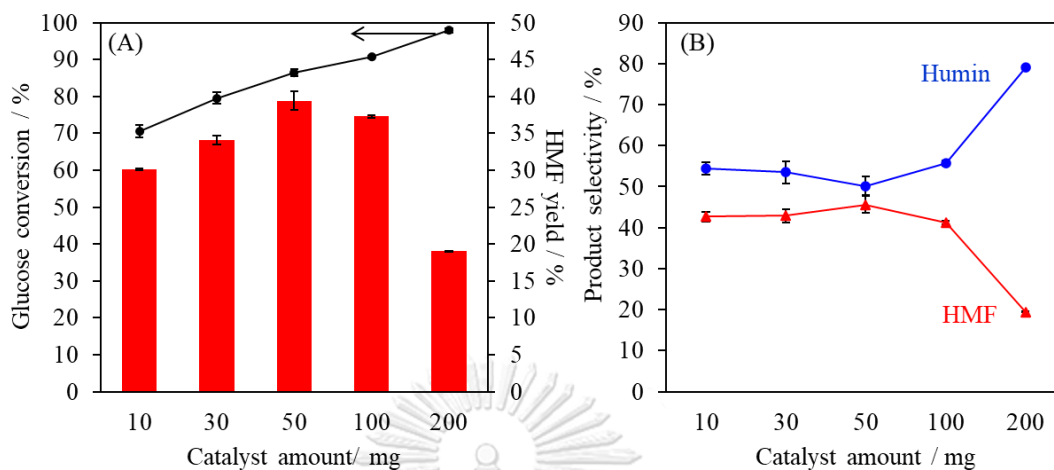


**Figure 6.5** Effect of catalyst amount on glucose conversion to HMF catalyzed by MCS-18S-0.2N. Reaction conditions: 5 mL 0.2-M glucose in NaCl solution, 10 mL THF, 190 °C, 1 h.

### 6.3 Reusability of MCS-SO<sub>3</sub>H-NH<sub>2</sub> composite

The reusability of MCS-18S-0.2N catalyst was preliminary evaluated in the HMF synthesis via glucose conversion under the suitable reaction conditions. The spent MCS-18S-0.2N was recovered from the reaction mixture by filtration, followed by thoroughly washing with deionized water and acetone, and drying at 100 °C overnight. As shown in Figure 6.6, the catalyst could be repeatedly used in the glucose dehydration at least 3 times during which the glucose conversion and HMF yield were gradually decreased to 63.6% and 29.2%, respectively. The 3<sup>rd</sup> reused catalyst was characterized for its elemental composition using TGA and CHNS analysis (Table 6.2). The content of carbon increased by 87 wt.%, while the amount of sulfur and nitrogen was slightly changed. Possibly, the deactivation of MCS-18S-0.2N was originated from a strong adsorption of organic substances on the catalyst surface, which limited the accessibility of glucose to the active sites during the reusability study.

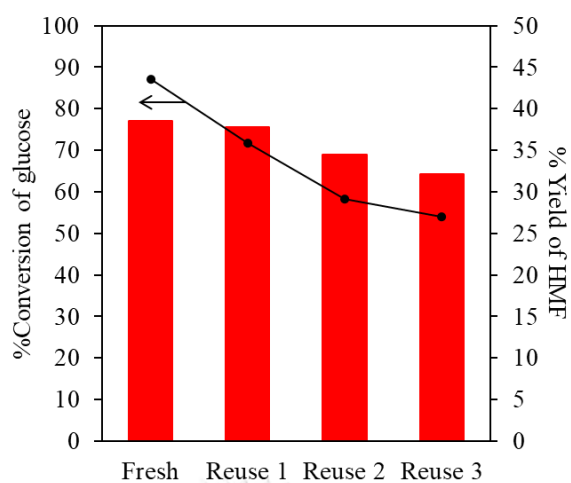


**Figure 6.6** Reusability of MCS-18S-0.2N in catalytic glucose conversion to HMF. Reaction conditions: 5 mL 0.2-M glucose in NaCl solution, 10 mL THF, 50 mg catalyst, 190 °C, 1 h.

**Table 6.2** Chemical composition of MCS-based catalysts fresh MCS-18S-0.2N and spent MCS-18S-0.2N after used at 3st cycle in glucose dehydration.

Sample	Carbon content <sup>a</sup> (wt.%)	Silica content <sup>a</sup> (wt.%)	Sulfur content <sup>b</sup> (mmol g <sup>-1</sup> )	Nitrogen content <sup>b</sup> (mmol g <sup>-1</sup> )
Frest-MCS-18S-0.2N	12.7	74.6	0.34	1.47
Spent-MCS-18S-0.2N	23.8	52.4	0.33	1.35

n.d. = not determined.

<sup>a</sup> Determined by thermogravimetric analysis.

<sup>b</sup> Determined by CHNS analyzer.

#### 6.4 Comparison of catalyst performance

Table 6.3 summarized the heterogeneous catalysts performance for synthesis of HMF by fructose or glucose dehydration. The MCS-18S (entry 4) revealed the highest HMF yield (56.0%) at a similar fructose conversion. The lower HMF yield on H-Mordenite (entry 1) can be attributed to its strong acidity, which facilitated the formation of humins and diffusion constraints of the reactants and products in the small zeolitic pores [122]. The silylation of H-Mordenite ( $\text{SiO}_2/\text{H-Mordenite}$ ) with TEOS enhanced the HMF selectivity because the silylating agent reduced the number of acid sites on the external surface of H-Mordenite particles, which is responsible for successive condensation of HMF to humins. Al-SBA-15 (entry 3) provides higher HMF yield and TON than H-Mordenite, which due to not only a weaker and lower acidity but also the confinement effect of mesostructured pores. These works pointed out that the catalysts with high acidity and low space constraints favor humin formation. The presence of sulfonic acid groups with high acid strength resulted in high catalytic performance of MCS-18S at relatively low temperature ( $150\text{ }^\circ\text{C}$ ), whereas the mesostructured framework-limited confinement for condensation of fructose and HMF to humins. In addition, the hydrophobicity of the carbon phase in the MCS catalyst retarded the humin formation [115] and HMF hydrolysis into LVA [123].

For the glucose conversion,  $\text{SiSnPO}_4$  [124] (entry 6) and H-Beta-Cal750 [125] (entry7) exhibited a higher HMF yield than  $\text{Nb}_2\text{O}_5$  [4] (entry 5) owing to the higher B/L ratio of  $\text{SiSnPO}_4$  (0.2) and H-Beta-Cal750 (0.94) compare to  $\text{Nb}_2\text{O}_5$  (0.1). A high Lewis acidity not only promoted the glucose isomerization, but also enhanced the formation of undesired products, such as humins. The HMF yield over MCS-18S-0.2N (39.4%) was lower than that obtained from Beta-Cal750 (43.0%) and  $\text{SiSnPO}_4$  (42.8%). However, MCS-18S-0.2N (6.4) exhibited higher TON than Beta-Cal750 (2.7) and  $\text{SiSnPO}_4$  (0.9) because the reaction over MCS-18S-0.2N was conducted at a higher glucose concentration. Moreover, the presence of hydrophobic carbon in the nanocomposite catalyst may restrain the adsorption of water molecules onto the catalyst surface, thus, retarding the HMF hydrolysis.

**Table 6.3** Overview of HMF yields from the conversion of fructose and glucose in the representative catalytic system.

Entry	Substrate	Solvent	Catalyst	Catalyst loading (%wt)	Temperature (C)	Time (h)	Conversion (mol%)	Yield (mol%)		TON <sup>a</sup>	Ref.
								HMF	LVA		
1	Fructose	H <sub>2</sub> O/MIBK	H-Mordenite	15	165	1	79	38.7	n.d.	9.3	[122]
2	Fructose	H <sub>2</sub> O/MIBK	SiO <sub>2</sub> /H-Mordenite	20	165	6.7	80	48.0	n.d.	11.7	[126]
3	Fructose	H <sub>2</sub> O/MIBK	Al-SBA-15	30	165	1	78	48.4	3.1	13.0	[122]
4	Fructose	H <sub>2</sub> O–NaCl/ THF	MCS-18S	56	150	2	81	56.0	0.0	3.8	This work
5	Glucose	H <sub>2</sub> O–NaCl/THF	Nb <sub>2</sub> O <sub>5</sub>	100	160	2	93	15.7	7.2	1.2	[4]
6	Glucose	H <sub>2</sub> O–DMSO/THF	SiSnPO <sub>4</sub>	100	180	1	75	42.8	n.d.	1.2	[124]
7	Glucose	H <sub>2</sub> O–DMSO/THF	H-Beta-Cal750	83	180	3	78	43.0	6.0	2.7	[125]
8	Glucose	H <sub>2</sub> O–NaCl/THF	MCS-18S-0.2N	28	190	1	86	39.4	0.0	6.4	This work

n.d. = not determined.

<sup>a</sup> Turnover number, determined as the mmol of HMF yield/(mmol of total active sites X weight of catalyst loading



## Chapter 7

### CONCLUSIONS AND RECOMMENDATIONS

#### 7.1 Conclusions

All of the results from Chapter IV to VI can be separately concluded in each part as shown belows;

**Chapter IV:** The MCS nanocomposites with a well-ordered mesostructure, high mesoporosity, and enhanced hydrophobicity were successfully prepared from the NR/HMS composite precursor via carbonization. The physicochemical properties of the resulting MCS nanocomposites could be controlled by varying the carbonization temperature, concentration of  $H_2SO_4$  solution used in the pretreatment step, and the initial NR content of the NR/HMS precursor. The MCS nanocomposites exhibited enhanced structural, textural, and hydrophobic properties after increasing the carbonization temperature up to 700 °C, while using a high concentration of  $H_2SO_4$  solution promoted rubber conversion into carbon residues, resulting in an increased carbon content. Increasing the amount of NR in the preparation of the NR/HMS precursor did not influence the carbon content but changed the structural and textural properties of the resulting MCS materials due to the limited incorporation of rubber molecules into the mesostructure of HMS. The MCS nanocomposites were characterized by a high dispersion of graphene oxide-like carbonaceous moieties with different types of surface oxygen-containing groups (C—O, C=O, C—O—O, and O—C=O). The tunable hydrophobic properties of MCS composites were not only determined by the content of carbonaceous materials, but also by the amount of surface silanol groups and oxygen-functional groups.

**Chapter V:** A series of acidic, basic, and bifunctional mesoporous carbon/silica materials with hexagonal mesostructure were successfully prepared by using NR/HMS as a catalyst precursor. The acid functions were introduced into the mesoporous silica by either post-grafting of organo-sulfonic acid groups or direct sulfonation on the carbon surface, whereas the 3-aminopropyl group grafting on the silica surface. The incorporation of carbon and/or the organofunctional group into the

HMS structure reduced the amount of free silanol groups and enhanced the hydrophobicity of the materials. For the sulfonated MCS (MCS-SO<sub>3</sub>H), increasing the H<sub>2</sub>SO<sub>4</sub> concentration in the sulfonation process enhances structural ordering, textural properties, and acidity of the obtained materials but reduce the hydrophobicity due to increased level of hydrophilic oxygen-containing groups (C—O, C=O, C—O—O, and O—C=O) and sulfonic acid groups. The introduction of amine-functional groups onto MCS-SO<sub>3</sub>H, giving the MCS-SO<sub>3</sub>H-NH<sub>2</sub>, led to lower structural ordering, textural properties, and acidity than MCS-SO<sub>3</sub>H. An increase in the amount of APS increased the basicity of the obtained materials and a decrease in the structural ordering and textural properties.

**Chapter VI:** The MCS catalyst without adding any acid or base functional groups, the presence of carbon in the mesoporous silica fairly promoted the fructose conversion into HMF. The MCS-SO<sub>3</sub>H catalysts with hydrophobicity and high acidity exhibited better catalytic activity than those of HMS-SO<sub>3</sub>H catalysts in the dehydration of fructose. The MCS-SO<sub>3</sub>H-NH<sub>2</sub> have prospect for the HMF synthesis from glucose. High Brønsted basicity promoted glucose isomerization and enhance the formation of humins. Moreover, the formation of levulinic acid, as a by-product from HMF hydrolysis, was retarded over the carbon/silica nanocomposite catalysts. Therefore, a suitable number of Brønsted acid/base sites and hydrophobicity are the key to gain the highest HMF yield. In addition, MCS-SO<sub>3</sub>H-NH<sub>2</sub> catalyst exhibited reusability in the glucose dehydration at least 3 cycles.

## 7.2 Recommendation and future works

The preparation of MCS-SO<sub>3</sub>H-NH<sub>2</sub> catalysts by post-grafting of organosilane should be comparatively studied to access the effect of distribution of functional groups on the catalyst surface. Although the MCS-SO<sub>3</sub>H-NH<sub>2</sub> catalysts provide the well catalytic performance in glucose conversion to HMF, the humins yield was still high when operating at high temperatures due to a high ratio of Brønsted basic/acid

sites, which resulting in an enhanced humins formation. To avoid undesired products and maximize the selectivity of HMF in the conversion of glucose, the preparation of zeolites with tunable Brønsted/Lewis acidity and porosity for the formation of HMF and humins should be investigated for further studies. Moreover, MCS-SO<sub>3</sub>H-NH<sub>2</sub> had strong adsorption of organic substances on the catalyst surface, resulting in deactivation of catalysts. Further study was ongoing to find the suitable conditions for regeneration of MCS-SO<sub>3</sub>H-NH<sub>2</sub>.



## REFERENCES

1. Werpy, T. and G. Petersen, *Top value added chemicals from biomass: volume I -- results of screening for potential candidates from sugars and synthesis Gas*. 2004, ; National Renewable Energy Lab., Golden, CO (US). p. Medium: ED.
2. Zhou, P. and Z. Zhang, *One-pot catalytic conversion of carbohydrates into furfural and 5-hydroxymethylfurfural*. *Catalysis Science & Technology*, 2016. **6**(11): p. 3694–3712.
3. Dallas Swift, T., H. Nguyen, A. Anderko, V. Nikolakis, and D.G. Vlachos, *Tandem Lewis/Brønsted homogeneous acid catalysis: conversion of glucose to 5-hydroxymethylfurfural in an aqueous chromium(iii) chloride and hydrochloric acid solution*. *Green Chemistry*, 2015. **17**(10): p. 4725–4735.
4. Li, X., K. Peng, Q. Xia, X. Liu, and Y. Wang, *Efficient conversion of cellulose into 5-hydroxymethylfurfural over niobia/carbon composites*. *Chemical Engineering Journal*, 2018. **332**: p. 528–536.
5. Mednick, M.L., *The acid-base-catalyzed conversion of aldohexose into 5-(Hydroxymethyl)-2-furfural*. *The Journal of Organic Chemistry*, 1962. **27**(2): p. 398–403.
6. Takagaki, A., M. Ohara, S. Nishimura, and K. Ebitani, *A one-pot reaction for biorefinery: combination of solid acid and base catalysts for direct production of 5-hydroxymethylfurfural from saccharides*. *Chemical communications (Cambridge, England)*, 2009(41): p. 6276–6278.
7. Valle-Vigón, P., M. Sevilla, and A.B. Fuertes, *Mesostructured silica-carbon composites synthesized by employing surfactants as carbon source*. *Microporous and Mesoporous Materials*, 2010. **134**(1–3): p. 165–174.
8. Yokoi, T., S. Seo, N. Chino, A. Shimojima, and T. Okubo, *Preparation of silica/carbon composites with uniform and well-ordered mesopores by esterification method*. *Microporous and Mesoporous Materials*, 2009. **124**(1–3): p. 123–130.
9. Nuntang, S., et al., *Novel mesoporous composites based on natural rubber and*

- hexagonal mesoporous silica: Synthesis and characterization*. Materials Chemistry and Physics, 2014. **143**(3): p. 1199–1208.
10. Slater, A.G. and A.I. Cooper, *Porous materials. Function-led design of new porous materials*. Science, 2015. **348**(6238): p. 8075.
  11. Benhamou, A., M. Baudu, Z. Derriche, and J.P. Basly, *Aqueous heavy metals removal on amine-functionalized Si-MCM-41 and Si-MCM-48*. Journal of Hazardous Materials, 2009. **171**(1-3): p. 1001–1008.
  12. Jiménez-Jiménez, J., M. Rubio-Alonso, D.E. Quesada, E. Rodríguez-Castellón, and A. Jiménez-López, *Synthesis and characterisation of acid mesoporous phosphate heterostructure (PPH) materials*. Journal of Materials Chemistry, 2005. **15**(34): p. 3466–3472.
  13. dos Santos, S.M.L., et al., *Synthesis and characterization of ordered mesoporous silica (SBA-15 and SBA-16) for adsorption of biomolecules*. Microporous and Mesoporous Materials, 2013. **180**: p. 284–292.
  14. Wei, J., et al., *Thermal and hydrothermal stability of amino-functionalized SBA-16 and promotion of hydrophobicity by silylation*. Microporous and Mesoporous Materials, 2009. **117**(3): p. 596–602.
  15. Beck, J.S., et al., *A new family of mesoporous molecular sieves prepared with liquid crystal templates*. Journal of the American Chemical Society, 1992. **114**(27): p. 10834–10843.
  16. Tanev, P.T. and T.J. Pinnavaia, *Mesoporous silica molecular sieves prepared by ionic and neutral surfactant templating: A comparison of physical properties*. Chemistry of Materials, 1996. **8**(8): p. 2068–2079.
  17. Nuntang, S., S. Yousatit, T. Yokoi, and C. Ngamcharussrivichai, *Tunable mesoporosity and hydrophobicity of natural rubber/hexagonal mesoporous silica nanocomposites*. Microporous and Mesoporous Materials, 2019. **275**: p. 235–243.
  18. Cassiers, K., P.V.D. Voort, and E.F. Vansant, *Synthesis of stable and directly usable hexagonal mesoporous silica by efficient amine extraction in acidified water*. Chemical Communications, 2000(24): p. 2489–2490.

19. De Filippis, P. and M. Scarsella, *Functionalized hexagonal mesoporous silica as an oxidizing agent for the oxidative desulfurization of organosulfur compounds*. Industrial & Engineering Chemistry Research, 2008. **47**(3): p. 973–975.
20. Nuntang, S., et al., *Organosulfonic acid-functionalized mesoporous composites based on natural rubber and hexagonal mesoporous silica*. Materials Chemistry and Physics, 2014. **147**(3): p. 583–593.
21. Nuntang, S., T. Yokoi, T. Tatsumi, and C. Ngamcharussrivichai, *Enhanced esterification of carboxylic acids with ethanol using propylsulfonic acid-functionalized natural rubber/hexagonal mesoporous silica nanocomposites*. Catalysis Communications, 2016. **80**: p. 5–9.
22. Yousatit, S., T. Jittapasata, N. Leelaphattharaphan, S. Nuntang, and C. Ngamcharussrivichai, *One-pot synthesis of wormhole-like mesostructured silica with a high amine loading for enhanced adsorption of clofibric acid*. Journal of Porous Materials, 2018. **25**(6): p. 1611–1623.
23. Brown, J., L. Mercier, and T.J. Pinnavaia, *Selective adsorption of Hg<sup>2+</sup> by thiol-functionalized nanoporous silica*. Chemical Communications, 1999(1): p. 69–70.
24. Mercier, L. and T.J. Pinnavaia, *Heavy metal ion adsorbents formed by the grafting of a thiol functionality to mesoporous silica molecular sieves: factors affecting Hg(II) uptake*. Environmental Science & Technology, 1998. **32**(18): p. 2749–2754.
25. Pauly, T.R., Y. Liu, T.J. Pinnavaia, S.J.L. Billinge, and T.P. Rieker, *Textural mesoporosity and the catalytic activity of mesoporous molecular sieves with wormhole framework structures*. Journal of the American Chemical Society, 1999. **121**(38): p. 8835–8842.
26. Alothman, Z., *A Review: Fundamental aspects of silicate mesoporous materials*. materials, 2012. **5**(12): p. 2874–2902.
27. Stein, A., B.J. Melde, and R.C. Schroden, *Hybrid inorganic–organic mesoporous silicates—nanoscopic reactors coming of age*. Advanced Materials, 2000. **12**(19): p. 1403–1419.
28. Nuntang, S., et al., *Mesostructured natural rubber/in situ formed silica*

- nanocomposites: A simple way to prepare mesoporous silica with hydrophobic properties*. *Microporous and Mesoporous Materials*, 2018. **259**: p. 79–88.
29. Krueyai, Y., P. Punyapalakul, and A. Wongrueng, *Removal of haloacetonitrile by adsorption on thiol-functionalized mesoporous composites based on natural rubber and hexagonal mesoporous silica*. *Environmental Engineering Research*, 2015. **20**(4): p. 342–346.
  30. Zhong, R., et al., *Silica-carbon nanocomposite acid catalyst with large mesopore interconnectivity by vapor-Phase assisted hydrothermal treatment*. *ACS Sustainable Chemistry & Engineering*, 2018. **6**(6): p. 7859–7870.
  31. Zhong, R., et al., *Acidic mesostructured silica-carbon nanocomposite catalysts for biofuels and chemicals synthesis from sugars in alcoholic solutions*. *Applied Catalysis B: Environmental*, 2017. **206**: p. 74–88.
  32. Zhong, R. and B.F. Sels, *Sulfonated mesoporous carbon and silica-carbon nanocomposites for biomass conversion*. *Applied Catalysis B: Environmental*, 2018. **236**: p. 518–545.
  33. Zhang, Y., F.L. Lam, X. Hu, and Z. Yan, *Formation of an ink-bottle-like pore structure in SBA-15 by MOCVD*. *Chemical communications (Cambridge, England)*, 2008(41): p. 5131–5133.
  34. Tian, X., et al., *Sulfonic acid-functionalized mesoporous carbon/silica as efficient catalyst for dehydration of fructose into 5-hydroxymethylfurfural*. *RSC Advances*, 2016. **6**(103): p. 101526–101534.
  35. Ryoo, R., S.H. Joo, and S. Jun, *Synthesis of highly ordered carbon molecular sieves via template-mediated structural transformation*. *The Journal of Physical Chemistry B*, 1999. **103**(37): p. 7743–7746.
  36. Liu, R., et al., *Triconstituent co-assembly to ordered mesostructured polymer-silica and carbon-silica nanocomposites and large-pore mesoporous carbons with high surface areas*. *Journal of the American Chemical Society*, 2006. **128**(35): p. 11652–11662.
  37. Zhai, Y., B. Tu, and D. Zhao, *Organosilane-assisted synthesis of ordered mesoporous poly(furfuryl alcohol) composites*. *Journal of Materials Chemistry*,

2009. **19**(1): p. 131–140.
38. Björk, E.M., et al., *Mesoporous silica and carbon based catalysts for esterification and biodiesel fabrication—The effect of matrix surface composition and porosity*. Applied Catalysis A: General, 2017. **533**: p. 49–58.
39. Acharjee, T.C. and Y.Y. Lee, *Production of levulinic acid from glucose by dual solid-acid catalysts*. Environmental Progress & Sustainable Energy, 2018. **37**(1): p. 471–480.
40. Zhao, Y., S. Wang, H. Lin, J. Chen, and H. Xu, *Influence of a Lewis acid and a Brønsted acid on the conversion of microcrystalline cellulose into 5-hydroxymethylfurfural in a single-phase reaction system of water and 1,2-dimethoxyethane*. RSC Advances, 2018. **8**(13): p. 7235–7242.
41. Russo, P.A., et al., *Solid acids with SO<sub>3</sub>H groups and tunable surface properties: versatile catalysts for biomass conversion*. Journal of Materials Chemistry A, 2014. **2**(30): p. 11813–11824.
42. Nakajima, K., M. Hara, and S. Hayashi, *Environmentally Benign Production of Chemicals and Energy Using a Carbon-Based Strong Solid Acid*. Journal of the American Ceramic Society, 2007. **90**(12): p. 3725–3734.
43. Tursi, A., *A review on biomass: importance, chemistry, classification, and conversion*. Biofuel Research Journal, 2019. **6**(2): p. 962–979.
44. Zafar, S. *An Introduction to Biomass Energy*. 2021 [cited 2021 03/02]; Available from: <https://www.bioenergyconsult.com/tag/types-of-biomass/>.
45. Climent, M.J., A. Corma, and S. Iborra, *Conversion of biomass platform molecules into fuel additives and liquid hydrocarbon fuels*. Green Chemistry, 2014. **16**(2).
46. Isikgor, F.H. and C.R. Becer, *Lignocellulosic biomass: a sustainable platform for the production of bio-based chemicals and polymers*. Polymer Chemistry, 2015. **6**(25): p. 4497–4559.
47. Zoghلامي, A. and G. Paes, *Lignocellulosic biomass: understanding recalcitrance and predicting hydrolysis*. Frontiers in Chemistry, 2019. **7**: p. 874.
48. Eyley, S. and W. Thielemans, *Surface modification of cellulose nanocrystals*.



- Nanoscale, 2014. **6**(14): p. 7764–7779.
49. McKendry, P., *Energy production from biomass (part 1): overview of biomass*. Bioresource Technology, 2002. **83**(1): p. 37–46.
  50. Carpenter, D., T.L. Westover, S. Czernik, and W. Jablonski, *Biomass feedstocks for renewable fuel production: a review of the impacts of feedstock and pretreatment on the yield and product distribution of fast pyrolysis bio-oils and vapors*. Green Chemistry, 2014. **16**(2): p. 384–406.
  51. Machmudah, S., Wahyudiono, H. Kanda, and M. Goto, *Chapter 3 - hydrolysis of biopolymers in near-critical and subcritical water, in water extraction of bioactive compounds*, H. Dominguez González and M.J. González Muñoz, Editors. 2017, Elsevier. p. 69–107.
  52. Ragauskas, A.J., et al., *Lignin valorization: improving lignin processing in the biorefinery*. Science, 2014. **344**(6185): p. 1246843.
  53. Okolie, J.A., S. Nanda, A.K. Dalai, and J.A. Kozinski, *Chemistry and Specialty Industrial Applications of Lignocellulosic Biomass*. Waste and Biomass Valorization, 2020. **12**(5): p. 2145–2169.
  54. Sajid, M., X. Zhao, and D. Liu, *Production of 2,5-furandicarboxylic acid (FDCA) from 5-hydroxymethylfurfural (HMF): recent progress focusing on the chemical-catalytic routes*. Green Chemistry, 2018. **20**(24): p. 5427–5453.
  55. Takkellapati, S., T. Li, and M.A. Gonzalez, *An overview of biorefinery derived platform chemicals from a cellulose and hemicellulose biorefinery*. Clean Technol Environ Policy, 2018. **20**(7): p. 1615–1630.
  56. El Khadem, H.S., *Carbohydrates*, In *encyclopedia of physical science and technology (Third Edition)*, R.A. Meyers, Editor. 2003, Academic Press: New York. p. 369–416.
  57. Niaz, K., F. Khan, and M.A. Shah, *Chapter 18 - Analysis of carbohydrates (monosaccharides, polysaccharides)*, in *Recent Advances in Natural Products Analysis*, A. Sanches Silva, et al., Editors. 2020, Elsevier. p. 621–633.
  58. Kobayashi, H., H. Kaiki, A. Shrotri, K. Techikawara, and A. Fukuoka, *Hydrolysis of woody biomass by a biomass-derived reusable heterogeneous catalyst*.

- Chemical Science, 2016. **7**(1): p. 692–696.
59. Johnson, J.M. and F.D. Conforti, *FRUCTOSE*, In *encyclopedia of food sciences and nutrition (Second Edition)*, B. Caballero, Editor. 2003, Academic Press: Oxford. p. 2748–2752.
  60. Carraher, J.M., C.N. Fleitman, and J.-P. Tessonier, *kinetic and mechanistic study of glucose isomerization using homogeneous organic Brønsted base catalysts in water*. ACS Catalysis, 2015. **5**(6): p. 3162–3173.
  61. Li, H., S. Yang, S. Saravanamurugan, and A. Riisager, *Glucose isomerization by enzymes and chemo-catalysts: status and current advances*. ACS Catalysis, 2017. **7**(4): p. 3010–3029.
  62. Shapla, U.M., M. Solayman, N. Alam, M.I. Khalil, and S.H. Gan, *5-Hydroxymethylfurfural (HMF) levels in honey and other food products: effects on bees and human health*. Chemistry Central Journal, 2018. **12**(1): p. 35.
  63. Saikia, K., et al., *Recent advances in biotransformation of 5-hydroxymethylfurfural: challenges and future aspects*. Journal of Chemical Technology & Biotechnology, 2021.
  64. Rosatella, A.A., S.P. Simeonov, R.F.M. Frade, and C.A.M. Afonso, *5-Hydroxymethylfurfural (HMF) as a building block platform: Biological properties, synthesis and synthetic applications*. Green Chemistry, 2011. **13**(4): p. 754-793.
  65. Li, M., et al., *High conversion of glucose to 5-hydroxymethylfurfural using hydrochloric acid as a catalyst and sodium chloride as a promoter in a water/ $\gamma$ -valerolactone system*. RSC Advances, 2017. **7**(24): p. 14330–14336.
  66. Chheda, J.N., Y. Román-Leshkov, and J.A. Dumesic, *Production of 5-hydroxymethylfurfural and furfural by dehydration of biomass-derived mono- and poly-saccharides*. Green Chemistry, 2007. **9**(4): p. 342–350.
  67. Jia, S., Z. Xu, and Z.C. Zhang, *Catalytic conversion of glucose in dimethylsulfoxide/water binary mix with chromium trichloride: Role of water on the product distribution*. Chemical Engineering Journal, 2014. **254**: p. 333–339.
  68. Yang, Y., C.-w. Hu, and M.M. Abu-Omar, *Conversion of carbohydrates and lignocellulosic biomass into 5-hydroxymethylfurfural using  $AlCl_3 \cdot 6H_2O$  catalyst*

- in a biphasic solvent system*. Green Chemistry, 2012. **14**(2): p. 509–513.
69. Nakamura, Y. and S. Morikawa, *The dehydration of D-fructose to 5-hydroxymethyl-2-furaldehyde*. Bulletin of the Chemical Society of Japan, 1980. **53**(12): p. 3705–3706.
70. Vasudevan, V. and S.H. Mushrif, *Insights into the solvation of glucose in water, dimethyl sulfoxide (DMSO), tetrahydrofuran (THF) and N,N-dimethylformamide (DMF) and its possible implications on the conversion of glucose to platform chemicals*. RSC Advances, 2015. **5**(27): p. 20756–20763.
71. Li, X., et al., *High yield production of HMF from carbohydrates over silica–alumina composite catalysts*. Catalysis Science & Technology, 2016. **6**(20): p. 7586–7596.
72. Yang, Q., W. Lan, and T. Runge, *Salt-Promoted glucose aqueous isomerization catalyzed by heterogeneous organic Base*. ACS Sustainable Chemistry & Engineering, 2016. **4**(9): p. 4850–4858.
73. Nishihara, H., et al., *Carbon-coated mesoporous silica with hydrophobicity and electrical conductivity*. Carbon, 2008. **46**(1): p. 48–53.
74. Liu, Y., et al., *Preparation and properties of sulfonated carbon–silica composites from sucrose dispersed on MCM-48*. Chemical Engineering Journal, 2009. **148**(1): p. 201–206.
75. Peng, W.-H., Y.-Y. Lee, C. Wu, and K.C.W. Wu, *Acid–base bi-functionalized, large-pored mesoporous silica nanoparticles for cooperative catalysis of one-pot cellulose-to-HMF conversion*. Journal of Materials Chemistry, 2012. **22**(43).
76. Zhou, C., et al., *Conversion of glucose into 5-hydroxymethylfurfural in different solvents and catalysts: Reaction kinetics and mechanism*. Egyptian Journal of Petroleum, 2017. **26**(2): p. 477–487.
77. Zachariah, A.K., V.G. Geethamma, A.K. Chandra, P.K. Mohammed, and S. Thomas, *Rheological behaviour of clay incorporated natural rubber and chlorobutyl rubber nanocomposites*. RSC Adv., 2014. **4**(101): p. 58047–58058.
78. Li, S.-D., H.-P. Yu, Z. Peng, C.-S. Zhu, and P.-S. Li, *Study on thermal degradation of sol and gel of natural rubber*. Journal of Applied Polymer Science, 2000.

- 75(11): p. 1339–1344.
79. Shafeeyan, M.S., W.M.A.W. Daud, A. Houshmand, and A. Shamiri, *A review on surface modification of activated carbon for carbon dioxide adsorption*. Journal of Analytical and Applied Pyrolysis, 2010. **89**(2): p. 143-151.
80. Li, L., et al., *Thermal stability of oxygen-containing functional groups on activated carbon surfaces in a thermal oxidative environment*. Journal of Chemical Engineering of Japan, 2014. **47**(1): p. 21–27.
81. D'Souza, A.S. and C.G. Pantano, *Hydroxylation and dehydroxylation behavior of silica glass fracture surfaces*. Journal of the American Ceramic Society, 2002. **85**(6): p. 1499–1504.
82. Zhao, X.S., G.Q. Lu, A.K. Whittaker, G.J. Millar, and H.Y. Zhu, *Comprehensive study of surface chemistry of MCM-41 using <sup>29</sup>Si CP/MAS NMR, FTIR, pyridine-TPD, and TGA*. The Journal of Physical Chemistry B, 1997. **101**(33): p. 6525–6531.
83. Wang, X., K.S. Lin, J.C. Chan, and S. Cheng, *Direct synthesis and catalytic applications of ordered large pore aminopropyl-functionalized SBA-15 mesoporous materials*. The Journal of Physical Chemistry B, 2005. **109**(5): p. 1763–1769.
84. Khan, A.S., et al., *Vibrational spectroscopy of selective dental restorative materials*. Applied Spectroscopy Reviews, 2016. **52**(6): p. 507–540.
85. Kohl, S., A. Drochner, and H. Vogel, *Quantification of oxygen surface groups on carbon materials via diffuse reflectance FT-IR spectroscopy and temperature programmed desorption*. Catalysis Today, 2010. **150**(1–2): p. 67–70.
86. Ponnamma, D., et al., *Free-volume correlation with mechanical and dielectric properties of natural rubber/multi walled carbon nanotubes composites*. Composites Part A: Applied Science and Manufacturing, 2015. **77**: p. 164–171.
87. Edwards, H.G.M., D.R. Brown, J.R. Dale, and S. Plant, *Raman spectroscopic studies of acid dissociation in sulfonated polystyrene resins*. Journal of Molecular Structure, 2001. **595**(1-3): p. 111–125.
88. Zhang, W., et al., *The Effect of pH on the Functionalization of Nylon Fabric with*

- Carbon Nanotubes*. Journal of Nanoscience and Nanotechnology, 2012. **12**(1): p. 84–90.
89. Cuesta, A., P. Dhamelincourt, J. Laureyns, A. Martínez-Alonso, and J.M.D. Tascón, *Raman microprobe studies on carbon materials*. Carbon, 1994. **32**(8): p. 1523–1532.
90. Zhang, Y., Q. Liu, J. Xiang, S. Zhang, and R.L. Frost, *Influence of the structural characteristic of pyrolysis products on thermal stability of styrene-butadiene rubber composites reinforced by different particle sized kaolinites*. Journal of Thermal Analysis and Calorimetry, 2014. **117**(3): p. 1201–1210.
91. Wu, J.B., M.L. Lin, X. Cong, H.N. Liu, and P.H. Tan, *Raman spectroscopy of graphene-based materials and its applications in related devices*. Chemical Society Reviews, 2018. **47**(5): p. 1822–1873.
92. Montero, J.M., M.A. Isaacs, A.F. Lee, J.M. Lynam, and K. Wilson, *The surface chemistry of nanocrystalline MgO catalysts for FAME production: An in situ XPS study of H<sub>2</sub>O, CH<sub>3</sub>OH and CH<sub>3</sub>OAc adsorption*. Surface Science, 2016. **646**: p. 170–178.
93. Wang, P., K.L. Tan, C.C. Ho, M.C. Khew, and E.T. Kang, *Surface modification of natural rubber latex films by graft copolymerization*. European Polymer Journal, 2000. **36**(7): p. 1323–1331.
94. Ganguly, A., S. Sharma, P. Papakonstantinou, and J. Hamilton, *Probing the thermal deoxygenation of graphene oxide using high-resolution in situ X-ray-based spectroscopies*. The Journal of Physical Chemistry C, 2011. **115**(34): p. 17009–17019.
95. Park, M., J. Ryu, Y. Kim, and J. Cho, *Corn protein-derived nitrogen-doped carbon materials with oxygen-rich functional groups: a highly efficient electrocatalyst for all-vanadium redox flow batteries*. Energy & Environmental Science, 2014. **7**(11): p. 3727–3735.
96. Cheung, W.H., S.S.Y. Lau, S.Y. Leung, A.W.M. Ip, and G. McKay, *Characteristics of chemical modified activated carbons from bamboo scaffolding*. Chinese Journal of Chemical Engineering, 2012. **20**(3): p. 515–523.

97. Pak, S.H., M.J. Jeon, and Y.W. Jeon, *Study of sulfuric acid treatment of activated carbon used to enhance mixed VOC removal*. International Biodeterioration & Biodegradation, 2016. **113**: p. 195–200.
98. Mena Aguilar, K.M., Y. Kose, Y. Amano, M. Machida, and F. Imazeki, *Influence of oxidation conditions of activated carbon on adsorption of Pb(II) from aqueous solution*. Journal of Environmental Chemistry, 2016. **26**(3): p. 109–114.
99. Kimura, H., et al., *Molecular dynamics and orientation of stretched rubber by solid-state <sup>13</sup>C NMR*. Polymer Journal, 2010. **42**(1): p. 25–30.
100. Kitamura, M., Y. Hata, H. Yasuoka, T. Kurotsu, and A. Asano, *Strain-induced <sup>13</sup>C chemical shift change of natural rubber*. Polymer Journal, 2012. **44**(8): p. 778–785.
101. Schmidt, T., et al., *Characterization of rubber particles and rubber chain elongation in Taraxacum koksaghyz*. BMC Biochem, 2010. **11**: p. 11.
102. Zhong, R., et al., *An eco-friendly soft template synthesis of mesostructured silica-carbon nanocomposites for acid catalysis*. ChemCatChem, 2015. **7**(18): p. 3047–3058.
103. Yousatit, S., et al., *Natural rubber as a renewable carbon source for mesoporous carbon/silica nanocomposites*. Scientific Reports, 2020. **10**(1): 12977.
104. Chua, Y.T., C.X.C. Lin, F. Kleitz, and S. Smart, *Synthesis of mesoporous carbon-silica nanocomposite water-treatment membranes using a triconstituent co-assembly method*. Journal of Materials Chemistry A, 2015. **3**(19): p. 10480–10491.
105. Shanthi, P.M., et al., *Sulfonic acid based complex framework materials (CFM): nanostructured polysulfide immobilization systems for rechargeable lithium-sulfur battery*. Journal of The Electrochemical Society, 2019. **166**(10): p. A1827–A1835.
106. Hood, Z.D., et al., *Tire-derived carbon for catalytic preparation of biofuels from feedstocks containing free fatty acids*. Carbon Resources Conversion, 2018. **1**(2): p. 165–173.

107. Liu, M., S. Jia, Y. Gong, C. Song, and X. Guo, *Effective hydrolysis of cellulose into glucose over sulfonated sugar-derived carbon in an Ionic Liquid*. *Industrial & Engineering Chemistry Research*, 2013. **52**(24): p. 8167–8173.
108. Wang, Y., et al., *Monodispersed hollow SO<sub>3</sub>H-functionalized carbon/silica as efficient solid acid catalyst for esterification of oleic acid*. *ACS Applied Materials & Interfaces*, 2015. **7**(48): p. 26767–26775.
109. Samadder, R., et al., *Magnetic nanocomposite based on polyacrylic acid and carboxylated cellulose nanocrystal for the removal of cationic dye*. *RSC Advances*, 2020. **10**(20): p. 11945–11956.
110. Johnson, R.L., et al., *Spectrally edited 2D <sup>13</sup>C–<sup>13</sup>C NMR spectra without diagonal ridge for characterizing <sup>13</sup>C-enriched low-temperature carbon materials*. *Journal of Magnetic Resonance*, 2013. **234**: p. 112–124.
111. Shiju, N.R., A.H. Alberts, S. Khalid, D.R. Brown, and G. Rothenberg, *Mesoporous silica with site-isolated amine and phosphotungstic acid groups: a solid catalyst with tunable antagonistic functions for one-Pot tandem reactions*. *Angewandte Chemie International Edition*, 2011. **50**(41): p. 9615–9619.
112. Wu, J.-B., M.-L. Lin, X. Cong, H.-N. Liu, and P.-H. Tan, *Raman spectroscopy of graphene-based materials and its applications in related devices*. *Chemical Society Reviews*, 2018. **47**(5): p. 1822–1873.
113. Loganathan, S. and A.K. Ghoshal, *Amine tethered pore-expanded MCM-41: A promising adsorbent for CO<sub>2</sub> capture*. *Chemical Engineering Journal*, 2017. **308**: p. 827–839.
114. Yokoi, T., H. Yoshitake, and T. Tatsumi, *Synthesis of amino-functionalized MCM-41 via direct co-condensation and post-synthesis grafting methods using mono-, di- and tri-amino-organoalkoxysilanes*. *Journal of Materials Chemistry*, 2004. **14**(6): p. 951–957
115. Patil, S.K.R., J. Heltzel, and C.R.F. Lund, *Comparison of structural features of humins formed catalytically from glucose, fructose, and 5-hydroxymethylfurfuraldehyde*. *Energy & Fuels*, 2012. **26**(8): p. 5281–5293.
116. James, O.O., et al., *Towards the conversion of carbohydrate biomass feedstocks*

- to biofuels via hydroxymethylfurfural*. Energy & Environmental Science, 2010. **3**(12).
117. Delidovich, I. and R. Palkovits, *Structure–performance correlations of Mg–Al hydrotalcite catalysts for the isomerization of glucose into fructose*. Journal of Catalysis, 2015. **327**: p. 1–9.
118. Huber, G.W., J.N. Chheda, C.J. Barrett, and J.A. Dumesic, *Production of liquid alkanes by aqueous-phase processing of biomass-derived carbohydrates*. Science, 2005. **308**(5727): p. 1446–1450.
119. Liu, C., et al., *Selective base-catalyzed isomerization of glucose to fructose*. ACS Catalysis, 2014. **4**(12): p. 4295–4298.
120. Garcés, D., E. Díaz, and S. Ordóñez, *Aqueous phase conversion of hexoses into 5-hydroxymethylfurfural and levulinic acid in the presence of hydrochloric Acid: mechanism and kinetics*. Industrial & Engineering Chemistry Research, 2017. **56**(18): p. 5221–5230.
121. Tan-Soetedjo, J.N.M., et al., *Experimental and kinetic modeling studies on the conversion of sucrose to levulinic acid and 5-hydroxymethylfurfural using sulfuric acid in water*. Industrial & Engineering Chemistry Research, 2017. **56**(45): p. 13228–13239.
122. Lucas, N., G. Kokate, A. Nagpure, and S. Chilukuri, *Dehydration of fructose to 5-hydroxymethyl furfural over ordered ALSBA-15 catalysts*. Microporous and Mesoporous Materials, 2013. **181**: p. 38–46.
123. Zhang, X., et al., *Highly efficient preparation of HMF from cellulose using temperature-responsive heteropolyacid catalysts in cascade reaction*. Applied Catalysis B: Environmental, 2016. **196**: p. 50–56.
124. Zhang, T., et al., *Efficient production of 5-hydroxymethylfurfural from glucose over silica-tin oxide composite catalysts*. Microporous and Mesoporous Materials, 2021. **311**: 110717.
125. Otomo, R., T. Yokoi, J.N. Kondo, and T. Tatsumi, *Dealuminated Beta zeolite as effective bifunctional catalyst for direct transformation of glucose to 5-hydroxymethylfurfural*. Applied Catalysis A: General, 2014. **470**: p. 318–326.



126. Ordonsky, V.V., J. van der Schaaf, J.C. Schouten, and T.A. Nijhuis, *The effect of solvent addition on fructose dehydration to 5-hydroxymethylfurfural in biphasic system over zeolites*. *Journal of Catalysis*, 2012. **287**: p. 68–75.



## APPENDIX A

## Quantitative chemical calculation for preparation MCS composites

## A1. Preparation of sulfuric acid solution for acid pretreatment

**Table A.1** Molecular weight and density of concentrated sulfuric acid solution

Physical property	Value
Concentration (%wt/wt)	95-98
Molecular weight (g/mol)	98.08
Density (g/mL)	1.84

Examples of calculation for preparation of 150 mL of 2 M  $H_2SO_4$  in ethanol

Concentration of concentrated  $H_2SO_4$  solution in molar

$$= \frac{96.5 \text{ g } H_2SO_4}{100 \text{ g solution}} \times \frac{1 \text{ mol } H_2SO_4}{98.08 \text{ g } H_2SO_4} \times \frac{1.84 \text{ g solution}}{1 \text{ mL solution}} \times \frac{1000 \text{ mL solution}}{1 \text{ L solution}} = 18.1 \text{ mol/L}$$

Volume of concentrated  $H_2SO_4$  solution for prepared 150 mL of 2 M  $H_2SO_4$  in ethanol

$$= \frac{2 \text{ mol } H_2SO_4}{1 \text{ L solution}} \times \frac{1 \text{ L solution}}{18.1 \text{ mol } H_2SO_4} \times 150 \text{ mL} = 16.6 \text{ mL}$$

Weight of concentrated  $H_2SO_4$  solution for prepared 150 mL of 2 M  $H_2SO_4$  in ethanol

$$= 16.6 \text{ mL} \times \frac{1.84 \text{ g solution}}{1 \text{ mL solution}} \times \frac{100 \text{ g solution}}{96.5 \text{ g } H_2SO_4} = 31.7 \text{ g}$$

Firstly, 31.7 g of concentrated  $H_2SO_4$  was dissolved in 100 mL of ethanol, and then then add ethanol up to 150 mL.

## APPENDIX B

## HPLC Chromatogram and Standard Curve of Reactants and Products

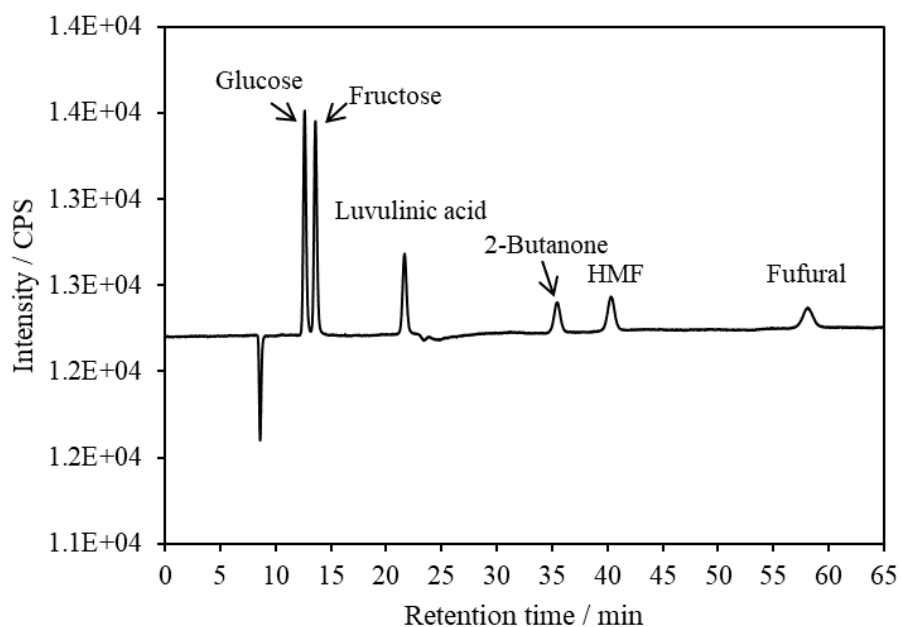


**Figure B.1** Chromatogram of Glucose, Fructose, Luvulinic acid, HMF, and fufural in aqueous phase by using 2-butanone as internal standard.

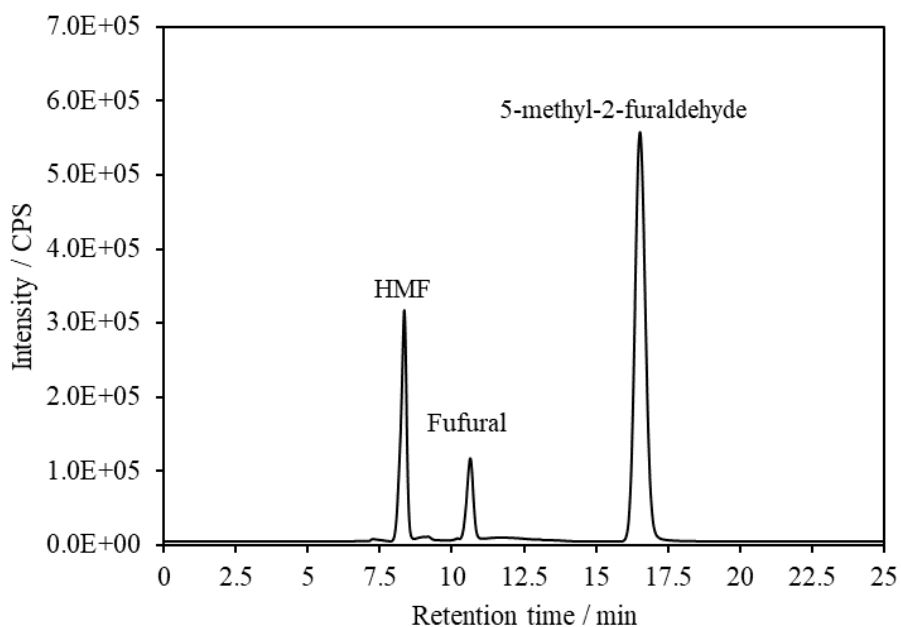


**Figure B.2** Chromatogram of HMF and fufural in organic phase by using 5-methyl-2-furaldehyde as internal standard.

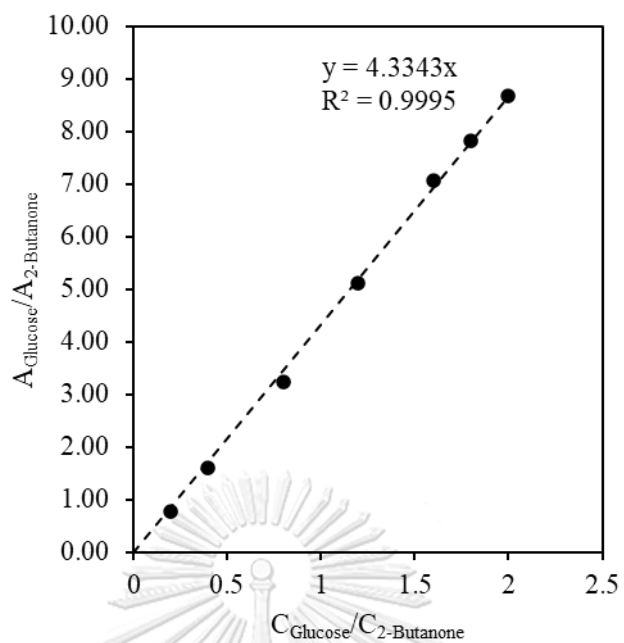


Figure B.3 The standard curves of glucose by using 2-butanone as internal standard.

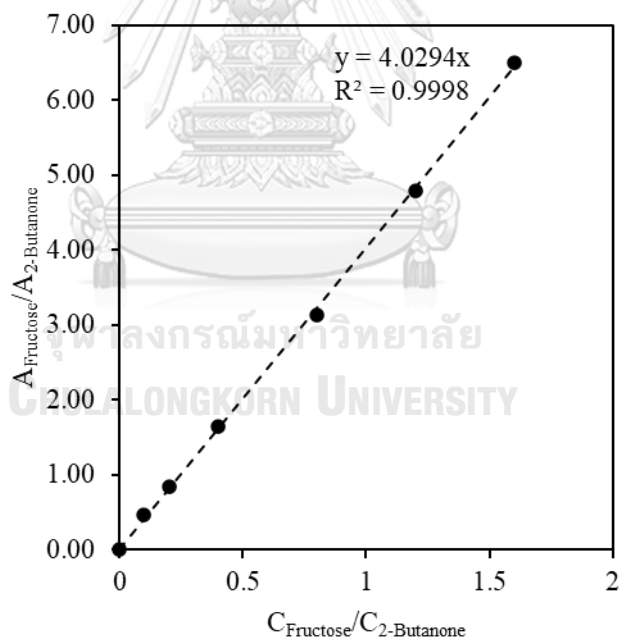


Figure B.4 The standard curves of fructose by using 2-butanone as internal standard.

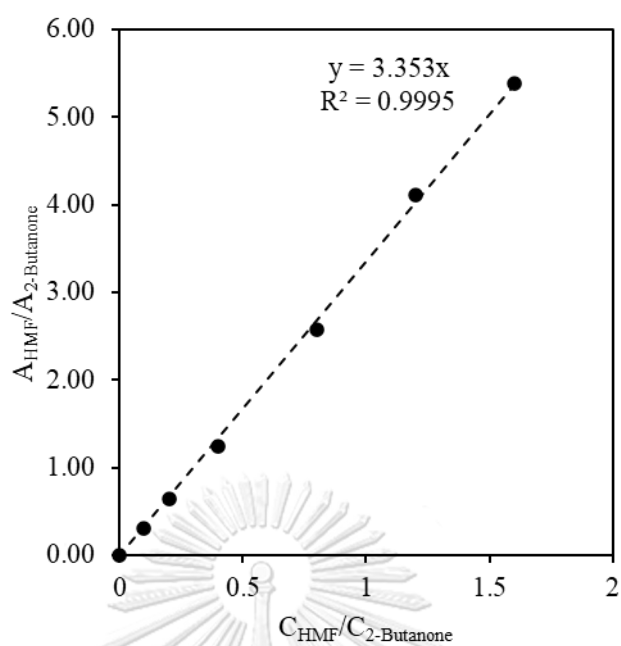


Figure B.5 The standard curves of HMF by using 2-butanone as internal standard.

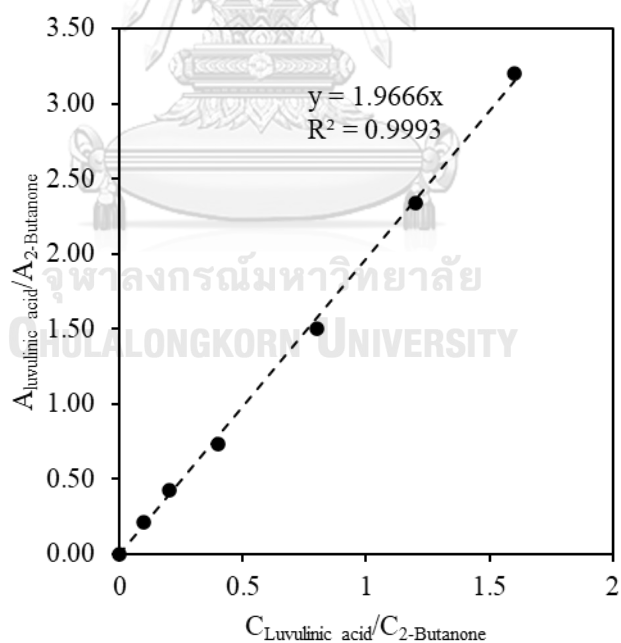


Figure B.6 The standard curves of luvulinic acid by using 2-butanone as internal standard.

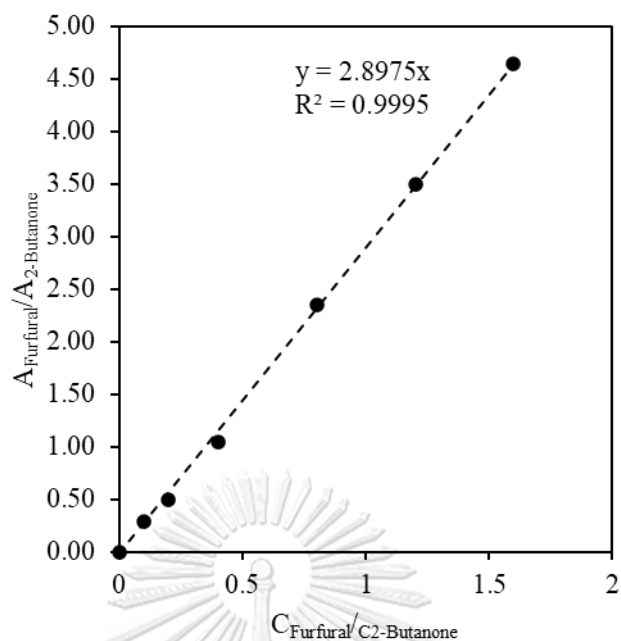


Figure B.7 The standard curves of furfural by using 2-butanone as internal standard.

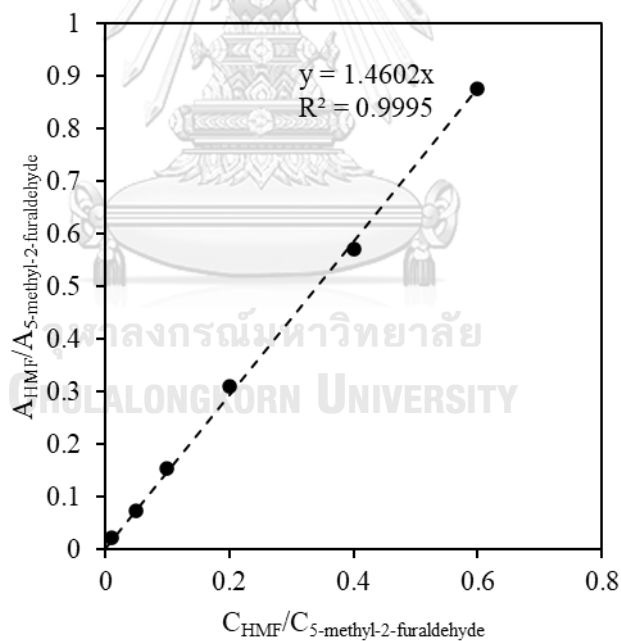
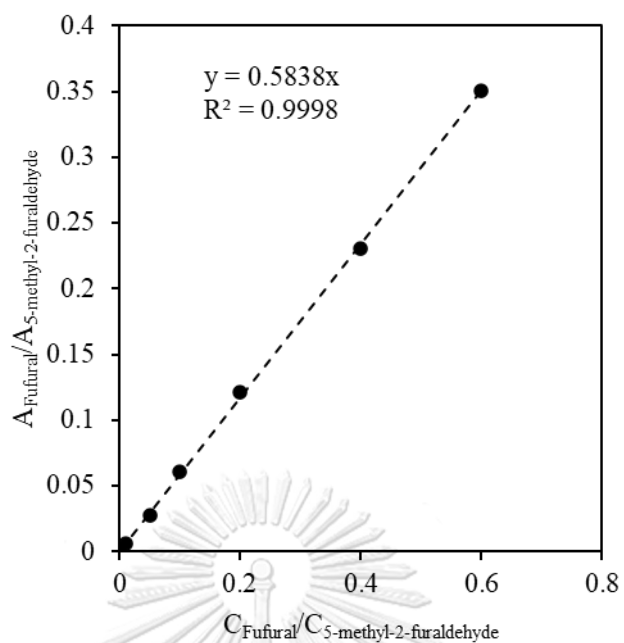


Figure B.8 The standard curves of HMF by using 5-methyl-2-furaldehyde as internal standard.



**Figure B.9** The standard curves of furfural by using 5-methyl-2-furaldehyde as internal standard.

## APPENDIX C

## Calculation of conversion

HPLC analyzer was used to analyze the sugar substrates and products in dehydration of glucose or fructose. The reactant and products were identified using internal standard method. The product yield and sugar conversion were calculated based on the results obtained from HPLC. 2-Butanone (for aqueous phase) and 5-methyl-2-furaldehyde (for organic phase) were used as internal standard.

The conversion, the product yields, and the product selectivity were calculated as follows:

$$\% \text{Conversion} = \left( \frac{\text{mole of reactant converted}}{\text{mole of reactant fed}} \right) \times 100\%$$

$$\% \text{Yield} = \left( \frac{\text{mole of product generated}}{\text{mole of reactant fed}} \right) \times 100\%$$

$$\% \text{Selectivity} = \left( \frac{\text{mole of product generated}}{\text{mole of reactant converted}} \right) \times 100\%$$

## Examples of calculation for aqueous phase

**Table C.2** Peak area of sugar substrates and products in aqueous phase

Catalyst	Peak area			
	Glucose	Fructose	LVA	2-Butanone
MCS-18S-0.2N	24395	7387	0	6728

Reaction conditions: 100 mg catalyst, 5 ml of 200 mM glucose in NaCl solution, 10 ml THF, 150 °C, 2 h.

Let Mole of glucose fed = 1 mmol

2-Butanone concentration in analyzed solution = 10 mM

Correction factor of glucose = 4.3343

Correction factor of fructose = 4.294



### Glucose conversion

Concentration of glucose in analyzed solution in molar

$$= \frac{\text{Peak area of glucose}}{\text{Peak area of 2 - Butanone}} \times \frac{2 - \text{Butanone concentration}}{4.3343}$$

$$= \frac{24395}{6728} \times \frac{10 \text{ mM}}{4.3343} = 8.37 \text{ mM}$$

Actual concentration of glucose in aqueous phase in molar

$$= 8.37 \text{ mM} \times \frac{3.00 \text{ mL}}{2.85 \text{ mL}} \times 10 = 88.11 \text{ mM}$$

Mole of remaining glucose

$$= \frac{88.11 \text{ mmol glucose}}{1 \text{ L solution}} \times \frac{1 \text{ L solution}}{1000 \text{ mL solution}} \times 5 \text{ mL solution}$$

$$= 0.44 \text{ mol}$$

$$\% \text{conversion of glucose} = \frac{1.00 - 0.44}{1.00} \times 100\% = 56.0\%$$

Fructose yield and selectivity

Concentration of fructose in analyzed solution in molar

$$= \frac{\text{Peak area of fructose}}{\text{Peak area of 2 - Butanone}} \times \frac{2 - \text{Butanone concentration}}{4.3343}$$

$$= \frac{7387}{6728} \times \frac{10 \text{ mM}}{4.3343} = 2.53 \text{ mM}$$

Actual concentration of fructose in aqueous phase in molar

$$= 2.53 \text{ mM} \times \frac{3.00 \text{ mL}}{2.85 \text{ mL}} \times 10 = 26.63 \text{ mM}$$

Mole of fructose generated

$$= \frac{26.63 \text{ mmol fructose}}{1 \text{ L solution}} \times \frac{1 \text{ L solution}}{1000 \text{ mL solution}} \times 5 \text{ mL solution}$$

$$= 0.13 \text{ mmol}$$

$$\% \text{Yield of fructose} = \frac{0.13}{1.00} \times 100\% = 13.3\%$$

$$\% \text{Selectivity to fructose} = \frac{0.13}{1.00 - 0.44} \times 100\% = 23.2\%$$

## Examples of calculation for organic phase

**Table C.3** Peak area of products in organic phase

Catalyst	Peak area			
	HMF	LVA	FF	5-MF
MCS-18S-0.2N	763953	0	24375	6826749

Reaction conditions: 100 mg catalyst, 5 ml of 200 mM glucose in NaCl solution, 10 ml THF, 150 °C, 2 h.

Let Mole of glucose fed = 1 mmol  
 5-methyl-2-furaldehyde (5-MF) concentration in analyzed solution  
 = 100 mM  
 Correction factor of HMF = 1.4602  
 Correction factor of furfural (FF) = 0.5838

### HMF yield and selectivity

Concentration of HMF in analyzed solution in molar

$$\begin{aligned}
 &= \frac{\text{Peak area of HMF}}{\text{Peak area of 5 - MF}} \times \frac{\text{5 - MF concentration}}{4.3343} \\
 &= \frac{763953}{6826749} \times \frac{100 \text{ mM}}{1.4602} = 7.66 \text{ mM}
 \end{aligned}$$

Actual concentration of HMF in organic phase in molar

$$= 7.66 \text{ mM} \times \frac{3.00 \text{ mL}}{2.70 \text{ mL}} = 8.52 \text{ mM}$$

Mole of HMF generated

$$\begin{aligned}
 &= \frac{8.52 \text{ mmol fructose}}{1 \text{ L solution}} \times \frac{1 \text{ L solution}}{1000 \text{ mL solution}} \times 10 \text{ mL solution} \\
 &= 0.085 \text{ mmol}
 \end{aligned}$$

$$\% \text{Yield of HMF} = \frac{0.085}{1.00} \times 100\% = 8.5\%$$

$$\% \text{Selectivity to HMF} = \frac{0.085}{1.00 - 0.44} \times 100\% = 15.2\%$$

## VITA

<b>NAME</b>	Satit Yousatit
<b>DATE OF BIRTH</b>	05 April 1991
<b>PLACE OF BIRTH</b>	Songkhla, Thailand
<b>INSTITUTIONS ATTENDED</b>	M.Sc. (Chemical Technology), Department of Chemical Technology, Faculty of Science, Chulalongkorn University. B.Sc. (Petrochemicals and Polymeric Materials, 2nd class honors), Department of Materials Science and Engineering, Faculty of Engineering and Industrial Technology, Silpakorn University.
<b>HOME ADDRESS</b>	129 Village No.5, Na Mom, Songkhla 90310
<b>PUBLICATION</b>	Yousatit, S.; Osuga, R.; Kondo, J.N.; Yokoi, T.; Ngamcharussrivichai, C. “Selective synthesis of 5-hydroxymethylfurfural over natural rubber-derived carbon/silica nanocomposites with acid–base bifunctionality” <i>Fuel</i> 311 (2022) 122577.  Khumho, R.; Yousatit, S.; Ngamcharussrivichai, C. “Glucose Conversion into 5-Hydroxymethyl-furfural over Niobium Oxides Supported on Natural Rubber-Derived Carbon/Silica Nanocomposite” <i>Catalysts</i> 11 (2021) 887.  Yousatit, S.; Pitayachinchot, H.; Wijitrat, A; Chaowamalee, S.; Nuntang, S.; Soontaranon, S.; Rugmai S.; Yokoi, T.; Ngamcharussrivichai, C. “Natural rubber as a renewable carbon source for mesoporous carbon/silica nanocomposites” <i>Scientific Reports</i> 10 (2020) 12977.

Nuntang, S.; Yousatit, S.; Yokoi, T.; Ngamcharussrivichai, C. "Tunable mesoporosity and hydrophobicity of natural rubber/hexagonal mesoporous silica nanocomposites" *Microporous Mesoporous Mater.* 275 (2019) 235–243.

Nuntang, S.; Yousatit, S.; Chaowamalee, S.; Yokoi, T.; Tatsumi, T.; Ngamcharussrivichai, C. "Mesostructured natural rubber/in situ formed silica nanocomposites: A simple way to prepare mesoporous silica with hydrophobic properties" *Microporous Mesoporous Mater.* 259 (2018) 79–88.

Yousatit, S.; Jittapasata, T.; Leelaphattharaphan, N.; Nuntang, S.; Ngamcharussrivichai, C. "One-pot synthesis of wormhole-like mesostructured silica with a high amine loading for enhanced adsorption of clofibric acid" *J. Porous Mater.* 25 (2018) 1611–1623.

**AWARD RECEIVED**

Best Poster Presentation Award TIChE 2020 (Track: Catalysis / Reaction Tech) on the topic of "Sulfonic acid functionalized mesoporous carbon/silica nanocomposites as efficient catalyst for fructose conversion into 5-hydroxymethylfurfural"